

**“Click” Cucurbit[7]uril Hosts on Self-Assembled Monolayers:
Quantitative Supramolecular Complexation with Ferrocene Guests**

by
Shuohua (Kennedy) Chen

B.Sc., Simon Fraser University, 2019

Thesis Submitted in Partial Fulfillment of the
Requirements for the Degree of
Master of Science

in the
Department of Chemistry
Faculty of Science

© Shuohua (Kennedy) Chen 2022
SIMON FRASER UNIVERSITY
Spring 2022

Copyright in this work is held by the author. Please ensure that any reproduction or re-use is done in accordance with the relevant national copyright legislation.

Declaration of Committee

Name: Shuohua (Kennedy) Chen

Degree: Master of Science

Title: “Click” Cucurbit[7]uril Hosts on Self-Assembled Monolayers: Quantitative Supramolecular Complexation with Ferrocene Guests

Committee:

Chair: Krzysztof Starosta
Professor, Chemistry

Hua-Zhong Yu
Supervisor
Professor, Chemistry

Jeffrey Warren
Committee Member
Associate Professor, Chemistry

Steven Holdcroft
Committee Member
Professor, Chemistry

Loren Kaake
Examiner
Associated Professor, Chemistry

Abstract

Cucurbit[7]uril (CB[7]), a symmetrical pumpkin-shaped molecule with an internal volume that can encapsulate guest molecules of complementary shape and size at a 1:1 ratio, has attracted tremendous attention in diverse fields. Particularly, the outstanding in-solution binding affinity ($K_f > 10^9 \text{ M}^{-1}$) of the host-guest inclusion complexation between cucurbit[7]uril molecule host and ferrocene derivatives molecule guests (Fc@CB[7]) enables their potential applications as conjugation/immobilization motifs for constructing biosensors and other molecular devices. However, their interfacial host-guest complexation behaviour has been rarely studied, partially due to the limitation of current CB[7] surface immobilization strategies (suffering from either poor stability or time-consuming and inconvenient procedure). In this thesis, it was shown that the well-known copper(I)-catalyzed azide-alkyne cycloaddition “click” reaction (CuAAC) can be used to chemically attach alkyne-functionalized CB[7] onto an azide-terminated self-assembled monolayer (SAM) on gold. The reaction time has been reduced from several hours to 30 min compared to conventional methods (e.g., the olefin metathesis reaction or the thiol-ene “click” reaction). Thus prepared CB[7]-tethered SAMs enabled the determination of complexation properties of CB[7] towards various Fc derivatives (e.g., neutral, positively charged and negatively charged substituents) on the surface via conventional cyclic voltammetry measurements. Particularly, the derived complexation thermodynamics ($K_f = (1.6 \pm 0.3) \times 10^7 \text{ M}^{-1}$) for ferrocenemethanol (FcMeOH), and kinetics data ($k_a = (2.6 \pm 0.4) \times 10^3 \text{ M}^{-1}\text{s}^{-1}$, $k_d = (5.1 \pm 0.3) \times 10^{-5} \text{ s}^{-1}$) confirms its strong interfacial host-guest binding with the surface-immobilized CB[7]. Moreover, the as-strong binding affinity of surface-bound CB[7] toward an anionic ferrocene derivative confirms the feasibility of employing Fc@CB[7] as the conjugation motif for immobilizing biological macromolecules (that are often negatively charged) to biochip surfaces.

Keywords: copper(I)-catalyzed azide-alkyne cycloaddition, cucurbit[7]uril, ferrocene, supramolecular guest-host complexation, cyclic voltammetry

*This thesis is dedicated to that sunny afternoon at the
international departure gate on July 28, 2012.*

10220 km from Foshan, China to Vancouver, Canada.

Dad, Mom, and my closest Family

ξThank you. My love for you all can never be quantified.ξ

Acknowledgements

I would like to first express my sincerest gratitude to my encouraging and patient senior supervisor, Prof. Hua-Zhong Yu, who had supported me throughout my MSc study. And he had taught me that research is not about focusing on one topic at a time, and there are always a lot of amazing areas to be explored and discovered. And thank you for providing me opportunities to attend academic conferences and participate in an internship to help build my future career.

To my dearest family, especially my gradually ageing parents, we have not been together for holidays or festivals for nearly 10 years. I am very grateful that you have faith in me and lead me to believe that I am not alone, and I will not be alone in this journey. I love you very much.

To my boyfriend, Haoyang. Thank you for taking care of me and letting me be myself. Thank you for always being there for me and being patient with my frustration. You have helped me become a better person and I feel so protected around you.

I would like to thank my committee members, Prof. Jeffrey Warren and Prof. Steven Holdcroft for their insightful inputs to my research work, and encouragement. Great appreciation for our collaborator Dr. Ruibing Wang and his student, Dr. Jia Chen from the University of Macau for providing with the synthetic cucurbit[7]uril host molecule. Without you, this work wouldn't be possible.

A special and sincere thanks to Dr. Lin Qi, Prof. Ning Gan, and Dr. Kun Liu for being my great mentors since I started my graduate study. To my friends, Jenny Tabuñag, Bob Chin, Yi Yuan, Dan Chang, Fiona Huang, and An Zhu. Thank you for cheering me up and bringing me a lot of joy. The rest of the member of Yu group, Karen Jiang, Dr. Lishen Zhang, Dr. Clayton Schultz, Brigitta Sun, Alvin Zhou, Mahboubeh Naderi Boldaji, Cliff Ng, Henry Qi, Joshua Ham, Tom Bui, and Kitty Leung.

To my two little furry guinea pigs, Piggy and Baldy, you have been witnessing my ups and downs, and your wheeking and purring are some of the warmest wordings I hear every day and that can take away my stress.

I would also like to thank funding and 4D Labs, especially Michael Wang, who helped me to conduct the XPS experiment.

Table of Contents

Declaration of Committee.....	ii
Abstract.....	iii
Dedication.....	iv
Acknowledgements.....	v
Table of Contents.....	vi
List of Tables.....	viii
List of Figures.....	ix
List of Acronyms.....	xiv
Chapter 1. Introduction.....	1
1.1. Supramolecular Host-Guest Complexes.....	1
1.1.1. Cucurbit[n]uril (CB[n]) family: Cucurbit[7]uril.....	3
1.1.2. Comparison and Contrast: CB[7] vs. β -CD.....	5
1.1.3. In-solution Fc@CB[7] host-guest complexation.....	6
1.1.4. Interfacial Fc@CB[7] host-guest complexation.....	10
1.2. Self-Assembled Monolayers (SAMs).....	12
1.2.1. Alkanethiolate SAMs on gold.....	13
1.2.2. Formation of thiolated DNA SAMs on gold and the challenges.....	16
1.3. Click Reaction on Surface.....	19
1.4. Motivation and Outline of This Thesis.....	22
Chapter 2. Instrumental Techniques.....	24
2.1. Cyclic Voltammetry (CV) and Electrochemical Cells.....	24
2.2. Fourier-Transform Infrared Spectroscopy (FTIR).....	30
2.3. Water Contact Angle Measurement.....	34
2.4. X-Ray Photoelectron Spectroscopy (XPS).....	35
Chapter 3. Experimental Details.....	39
3.1. Reagents and Materials.....	40
3.2. Surface Modification and Host Guest Complexation (Fc@CB[7]).....	41
3.3. Surface characterizations.....	42
Chapter 4. Results and Discussion.....	44
4.1. “Click” \equiv -O-CB[7] Hosts on N3C11S-Au SAM Surface.....	45
4.2. Optimization of the Binary SAMs and Surface “Clicking” Efficiency.....	49
4.3. Thermodynamics and Kinetics of Host-Guest Complexation on Surface.....	54
4.4. Surface-Immobilized CB[7] Hosts for Quantifying the Complexation with Other Fc Derivatives.....	62
4.5. Obstacles and Potential for Future Applications.....	64

Chapter 5. Summary and Future Direction	66
5.1. Conclusions.....	66
5.2. Future Work.....	66
References.....	70
Appendix A. Additional Supplementary Data	82
A1. Determination of the effective surface area (A) of the gold working electrode.	82
A2. Preparation and Characterization of HO-CB[7] and ≡-O-CB[7].....	83
A3. Preparation and Characterization of FcN ⁺ Br ⁻	85
Appendix B Additional Publication List.....	87

List of Tables

Table 1.1	Pros and cons of commonly used solid substrates for supporting SAMs.	15
Table 4.1	Formation constants (K_f) of selective Fc derivatives toward CB[7]-O-taz-C11S-Au.	62

List of Figures

- Figure 1.1 The synthesis routes by reacting glycoluril and formaldehyde to prepare CB[n] homologues. n represents the number of glycoluril units. 3
- Figure 1.2 (A) Top and side view of the crystallographic structure of CB[6]. Color codes: gray, carbon; blue, nitrogen; red, oxygen. (B) Diameters of the synthetic cucurbituril homologues. 4
- Figure 1.3 (A) Structures of CB[7] and β -CD. (B) Surface electrostatic potential for CB[7] and β -CD. The colored bar on the far right describes the electronegativity from negative (red) to positive (blue). 6
- Figure 1.4 (A) X-ray crystal structure showing the Fc adopts two orientations inside the CB[7] host cavity. These relative position angles are 79° and 22° , respectively. (B) X-ray crystal structure showing the orientation of a dicationic Fc derivatives (bis(trimethylammoniomethyl)ferrocene), which resides within the CB[7] chamber at a relative position angles of 43.7° 8
- Figure 1.5 Cyclic voltammetric responses of (A) monocationic Fc derivatives and (B) mono-substituted neutral Fc derivative before and after adding an equivalent amount of CB[7]. Scan rate was kept at 0.1 V/s. 9
- Figure 1.6 Formation constants (K_f) of CB[7] towards some Fc derivatives with different structural features upon Fc@CB[7] host-guest inclusion complexes in solution. 10
- Figure 1.7 Host-guest binding of CB[7] toward surface-immobilized Fc at a molecular interfaces. The binary SAMs are made from 11-Ferrocenyl-1-undecanethiol and 1-octanethiol. 12
- Figure 1.8 (A) Illustration of an ideal single-component SAM of alkanethiolates formed on gold (111) surface. (B) Orientation of single long-chain alkanethiol adsorbed on gold (111) with defined tilt angle (α), rotation angle (β), and projection angle (χ). Typically, $\alpha = 30^\circ$, $\beta = 55^\circ$, and $\chi = 14^\circ$. The purple atom is sulfur and the blue atom is the carbon from the end methyl group of the alkanethiol. 13
- Figure 1.9 Schematic diagrams of (A) co-adsorption, in which the gold substrate is incubated in a binary solution of the two thiols and (B) Post-assembly exchange, in which the gold substrate is treated in a thiol followed by a subsequent treatment with another precursor. 16
- Figure 1.10 Schematic diagram of preparing thiolated DNA monolayers on gold. (A) Thiolated single-stranded DNA (HS-ssDNA) adsorbed on gold surface via the thiol-gold and backbone-gold interactions. (B) Adsorption of mercaptohexanol (MCH) displacing non-specifically adsorbed DNA and preventing the interaction between the DNA backbone and gold surface. (C) Hybridization of complementary strands on the prepared DNA/MCH SAMs. 18

Figure 1.11	Fluorescence images taken at open circuit potential of independently prepared fluorescent-labelled (A) (a) ssDNA/MCH modified gold surfaces, (b) another example of a ssDNA/MCH layer, and (B) (a) MCH/ssDNA layer. The intensity of fluorescence is rendered as a range of colors, shown in the color-intensity bar. 19
Figure 1.12	Comparison between thermally activated and copper(I)-catalyzed Huisgen 1,3- azide-alkyne cycloaddition. 20
Figure 1.13	Schematic illustrations of performing CuAAC reactions on solid substrates: (A) gold, (B) singled-walled carbon nanotube, and (C) glass. 21
Figure 1.14	Schematic diagram showing chemical attachment of alkyne-functionalized CB[7] (\equiv -O-CB[7]) onto a binary azide-terminated SAM on gold surface via CuAAC reaction followed by subsequent supramolecular complexation with ferrocenemethanol (FcMeOH). 23
Figure 2.1	(A) Cyclic voltammetry potential waveform. (B) Representative CV response of reversible redox-active species. The inset next to (B) shows the diffusion process of redox species toward the electrode surface. 24
Figure 2.2	Representative CV response of a reversible electrode-adsorbed redox-active species. 27
Figure 2.3	Schematic representation of a three-electrode electrochemical cell for CV measurements of solution diffused redox molecules. During measurements, the three electrodes (working, reference, and counter electrodes) are submerged in the same electrolyte solution. The additional two holes on the cap is for degassing the solution with a N ₂ or Ar line. 28
Figure 2.4	Schematic view of the single-chamber electrochemical cell made of Plexiglas V-grade acrylic resin. A: plate for mounting a working electrode (i.e., a gold slide with a dimension of 0.7 × 1.8 cm ²). B: main body of the cell with a top-opening for adding electrolyte solutions, and a side slot (indicated by the red dashed rectangle) for attaching the working electrode. The opening with an O-ring seal located in the middle of the slot defines the area of working electrode exposed to the electrolyte in the cell. C: holder to lock the working electrode-mounting plate inside the slot. D: cap with three holes for inserting an reference electrode, a counter electrode, and an inert gas line. E: photo of the assembled cell that is ready for performing measurements. 29
Figure 2.5	Schematic optical diagram of an interferometer in FTIR. The two mirrors are positioned perpendicular to one another. 31
Figure 2.6	Schematic diagram showing angle of incident with the sample by employing two tilt mirrors. 32

Figure 2.7	FTIR spectra of (a) octadecanethiol SAM on gold (C18S-Au), (b) undecanethiol SAM on gold (C11S-Au), (c) ferrocenyundecanethiol/undecaethiol SAMs on gold (FcC11S-/C11S-Au) prepared by the postassembly exchange method, (d) FcC11S-/C11S-Au prepared by coadsorption method, and (e) FcC11S-Au..... 33
Figure 2.8	Schematic of a water drop on a solid surface showing contact angle (θ) that is determined by a balance of of the interfacial tensions of solid-gas (γ_{SG}) and solid-liquid (γ_{SL}), and the horizontal projection of the liquid-gas (γ_{LG}) on the solid surface ($\gamma_{LG}\cos\theta$). 34
Figure 2.9	Schematic diagram of contact angle measurement setup with the sessile drop method drawn based on the AST VCA system goniometer. 35
Figure 2.10	Basic components of an XPS instrument using a hemispherical field analyzer. 36
Figure 2.11	Schematic diagram of the mechanism of electron emission in XPS. 37
Figure 2.12	XPS characterization of gold slides modified in binary deposition solutions that contain different mole fraction of HOC11SH and C10SH. (A) O 1s region and (B) C 1s region. 38
Figure 4.1	Reflection-adsorption FTIR spectra of N3C11S-Au before (black) and after the chemical attachment of $\equiv\text{-O-CB}[7]$ via CuAAC (red), and after the incubation of CB[7]-O-taz-C11S-Au in 50 μM FcMeOH for 1 h (blue). 45
Figure 4.2	Water contact angle measurements on the N3C11S-Au before (left) and after the tethering of $\equiv\text{-O-CB}[7]$ via CuAAC (middle), and upon the subsequent incubation in 50 μM FcMeOH for 1 h. The volume of the water droplet for each measurement was kept at 1.5 μl . The standard deviations were based on 3 randomly selected spots on three independently prepared gold samples..... 46
Figure 4.3	(A) Cyclic voltammetry of N3C11S-Au before (black) and after the tethering of $\equiv\text{-O-CB}[7]$ via CuAAC (red), and after incubating the CB[7]-O-taz-C11S-Au in 50 μM FcMeOH for 1 h (blue). The scan rate was kept at 0.1 V/s and the electrolyte was 10 mM Tris-HClO ₄ (pH 7.4). (B) Corresponding voltammograms of the same system obtained at different v . And (C) A plot for the corresponding reduction peak current (I_p) as a function of v . The dashed line is the best fit linear line to the experimental data ($R^2 = 0.99$). 48
Figure 4.4	XPS spectra of (A) N 1s and (B) C 1s of gold sides modified in different 95% EtOH deposition solutions contains different mole fractions of N3C11SH/C10SH ($\chi_{\text{sol}}^{\text{N}_3}$). (C) Relationship between the normalized intensity of N ₃ ($I_{\text{N } 1\text{s}}/I_{\text{C } 1\text{s}}$) on the surface. (D) Relationship between molar fraction of N ₃ on the surface and the solution position. The solid line is to guide the eye only. 50

- Figure 4.5 Water contact angle measurements on the modified gold plotted as a function of the N3C11SH/C10SH ($\chi_{\text{sol}}^{\text{N3}}$) in 95% EtOH deposition solutions. The insets show the images of 1.5 μl of deionized water droplet on the corresponding modified gold surface..... 51
- Figure 4.6 (A) Representative CV responses of N3C11S-/C10S-Au prepared from different 95% EtOH with various $\chi_{\text{sol}}^{\text{N3}}$ upon clicking $\equiv\text{-O-CB[7]}$ and incubation in 50 μM FcMeOH for 1 h. The scan rate was kept at 0.1 V/s. (B) Corresponding Γ_{Fc} determined based on the integrated charge of the oxidation peaks from (A) as a function of $\chi_{\text{sol}}^{\text{N3}}$. The error bars represent the standard deviations based on three independently prepared samples. 52
- Figure 4.7 (A) Representative CV responses upon treating the N3C11S-/C10S-Au ($\chi_{\text{sol}}^{\text{N3}} = 75\%$) with $\equiv\text{-O-CB[7]}$ via CuAAC for different reaction periods and followed by treatment in 50 μM FcMeOH for 1 h. The scan rate was kept at 0.1 V/s, and the electrolyte was 10.0 mM Tris-HClO₄ (pH 7.4). (B) Corresponding Γ_{Fc} determined based on the integrated charge of the oxidation peaks from (A) as a function of reaction time. The error bars represent the standard deviations based on the three independently prepared samples..... 53
- Figure 4.8 Representative CV of incubation of N3C11S-/C10S-Au ($\chi_{\text{sol}}^{\text{N3}} = 75\%$) in increasing concentrations of FcMeOH for 1 h each. The scan rate was kept at 0.1 V/s. 54
- Figure 4.9 Thermodynamics study. (A) Representative CV responses upon treating the CB[7]-O-taz-C11S-Au in increasing FcMeOH concentrations. The scan rate was kept at 0.1 V/s. (B) Corresponding equilibrated surface density of FcMeOH@CB[7] (Γ_{Fc}) based on the integrated charge of the oxidation peaks from (A) as a function of [FcMeOH]. The solid line is to guide the eyes only. (C) Interfacial formation constant (K_f) determined at different [FcMeOH]. The solid and dashed lines show the average and standard deviation of the determined K_f values based on three independent replicates. 56
- Figure 4.10 Association kinetic study. (A) Representative CV responses measured upon treating the CB[7]-O-taz-C11S-Au in 100 nM of FcMeOH prepared in 10 mM Tris-HClO₄ (pH 7.4) for different time period. The scan rate was kept at 0.1 V/s. (B) Corresponding surface density of FcMeOH@CB[7] (Γ_{Fc}) based on the integrated charge of the oxidation peaks from (A) as a function incubation time in 100 nM FcMeOH. (C) The relationship between $\ln [1 - \Gamma_{\text{Fc}(t)} / \Gamma_{\text{Fc}(\text{max})}]$ and the incubation time (t). The dashed line is the best linear fit ($R^2 = 0.99$). The error bars represent standard deviations based on three independently prepared samples. 58

- Figure 4.11 Dissociation kinetic study. (A) Representative CV responses after incubating a saturated FcMeOH@CB[7]-O-taz-C11S-Au in 10 mM Tris-HClO₄ (pH 7.4) that was free of FcMeOH for extended time. The scan rate was kept at 0.1 V/s. (B) Corresponding surface density of FcMeOH@CB[7] (Γ_{Fc}) based on the integrated charge of the oxidation peaks from (A) as a function incubation time in FcMeOH-free buffer. (C) The relationship between $\ln(\Gamma_{Fc(t)}/\Gamma_{Fc(max)})$ and the incubation time (t). The dashed line is the best linear fit ($R^2 = 0.99$). The error bars represent standard deviations based on three-independently prepared samples. 60
- Figure 4.12 Representative cyclic voltammograms of individual CB[7]-O-taz-C11S-Au treating in increasing concentrations (0 - 450 nM) of (A) FcNH₂, (B) FcN⁺Br⁻, (C) FcCOO⁻, and (D) FcAcCOO⁻. The scan rate was kept at 0.1 V/s. 63
- Figure 5.1 (A) Schematic illustrating the mechanism of the electrochemical DNA sensor with ratiometric analyses. The distance between the ferrocene tag (Fc) and the gold electrode remains unchanged before and after the binding of the target sequence (T) to the DNA probe (P), whereas the electrons transfer from methylene blue (MB) to the electrode surface get disrupted due to the elongated distance after T binding. (B) Comparison on the background signals (before target binding) measured from 2 sets of 50 individual electrode samples prepared based on the (left) single-labelled method and the (right) dual-labelled method (ratiometric analyses). The black histograms represent the background responses of 50 individual measurements over eight electrodes. Average values are represented by the red bars, and the red error bars in the red bars represented the SD for 50 individual measurements. 67
- Figure 5.2 Schematic view of employing Fc@CB[7] as the conjugation motif for constructing ratiometric electrochemical biosensors. a redox cation (e.g., [Ru(NH₃)₆]³⁺) will be adapted as the second signal probe. Note: details need to be presented for people to understand the entire design. 69

List of Acronyms

AA	L-ascorbic acid
C10SH	1-decanethiol
CB[7]	Cucurbit[7]uril
CD	Cyclodextrin
CE	Counter electrode
Cp	Cyclopentadienyl
CuAAC	Copper(I)-catalyzed azide-alkyne cycloaddition
CV	Cyclic voltammetry
EtBr	Bromoethane
EtOH	Ethanol
Fc	Ferrocene
FcAcCOOH	Ferroceneacetic acid
FcCOOH	Ferrocenecarboxylic acid
FcMeOH	Ferrocenemethanol
FcN	(Dimethylaminomethyl)ferrocene
FcN ⁺ Br ⁻	N-(ferrocenylmethyl)-N, N-dimethyl-N-ethylammonium
FcNH ₂	Aminoferrocene
FTIR	Fourier-transform infrared spectroscopy
MCH	Mercaptohexanol
MCT	Mercury cadmium telluride (detector)
N3C11SH	11-azido-1-undecanethiol
NMR	Nuclear magnetic resonance
pI	Isoelectric point
RE	Reference electrode
SAM	Self-assembled monolayer
SD	Standard deviation
THPTA	Tris(3-hydroxypropyltriazolylmethyl)amine
Tris	Tris(hydroxymethyl)aminomethane
WE	Working electrode
XPS	X-ray photoelectron spectroscopy

Chapter 1.

Introduction

1.1. Supramolecular Host-Guest Complexes

Supramolecular host-guest inclusion complexes consist of a host molecule with a cavity of an appropriate size that can accommodate one or more guest molecules and can be expressed as below:



During such an inclusion complexation process, only non-covalent interactions are involved to hold these assemblies together, including hydrophobic interactions, ionic bonds, hydrogen bonds, and van der Waals forces.¹ From the thermodynamic view, the spontaneous formation of a host-guest complex is driven by the decrease of the Gibbs free energy (ΔG):

$$\Delta G = \Delta H - T\Delta S \quad (1.2)$$

The reduction in ΔG is mainly the result of the decreased enthalpy (ΔH) arises from the improved stability upon complexation, whereas the overall change in entropy (ΔS) is a more complicated process. It involves a decrease of entropy from the complex formation and an increase of entropy from the desolvation processes of both guests and hosts.² Nevertheless, systematic studies with various spectroscopic techniques have confirmed that both the chemical nature of the host and guest compounds, and their geometric “match” contribute to the ΔG and the recognition ability.³

The most well known and naturally occurring supramolecular assembly is the biotin-avidin/streptavidin system with formation constants in the range of $10^{13} - 10^{15} \text{ M}^{-1}$.^{2,4} Both avidin and streptavidin as the host molecules have the ability to bind up to 4 biotin guest molecules.⁵ Early differential scanning calorimetry has shown that under a full saturation condition of the biotin, the thermal stabilities of avidin and streptavidin

dramatically increase to 117 °C from 112 °C and 83 °C from 75 °C, respectively.⁴ Because of this great thermal stability, they have been utilized as conjugation motifs and affinity matrices for a variety of applications, including but not limited to immunohistochemistry, enzyme-linked immunoassay, DNA hybridization, affinity purification, and drug delivery.^{6,7} However, it is the physical and chemical properties of avidin and streptavidin that act as their own barrier towards the application development. Different from avidin, streptavidin is of lower solubility due to the absence of carbohydrates and its near-neutral isoelectric point (pI).⁸ On the other hand, the presence of the carbohydrates in avidin and its high pI (pI ~10.5) lead to the nonspecific electrostatic binding.^{9,10}

In this regard, efforts have been devoted to preparing synthetic host-guest systems with affinities that are comparable to the biotin-avidin/streptavidin system. To date, 4 main classes of supramolecular compounds have been reported, i.e., cyclodextrins, crown ethers, calix[n]arenes, and cucurbit[n]uril, but for meeting specific application needs, more unconventional hosts are synthesized. Particularly, Rebek et al. created a macrocyclic capsule by dimerizing two vase-like compounds through their H-bonding at edges. The resulted capsule of nanometer dimensions can accommodate two different molecules.¹¹ Li et al. have synthesized a hexacationic host, which bears two TPZ³⁺ (trispyridiniumtriazine) bridged and separated by three ethylene-triazole-ethylene linkers in a face-to-face manner, for capturing anthracene guest to prevent it from undergoing Diels-Alder reaction.¹² Jiang et al. developed a pair of amide naphthotubes that selectively binds to 2-phenyl pyrimidine guests with a moderate formation constant ($7.0 \times 10^5 \text{ M}^{-1}$), which can be employed in cell targeting and tissue imaging.¹³ However, these synthetic hosts only display moderate binding affinities toward guest molecules ($10^3 - 10^6 \text{ M}^{-1}$); therefore, they are not commonly found in literature search, making the cucurbit[n]uril still the dominant in the field of supramolecular chemistry.

1.1.1. Cucurbit[n]uril (CB[n]) family: Cucurbit[7]uril

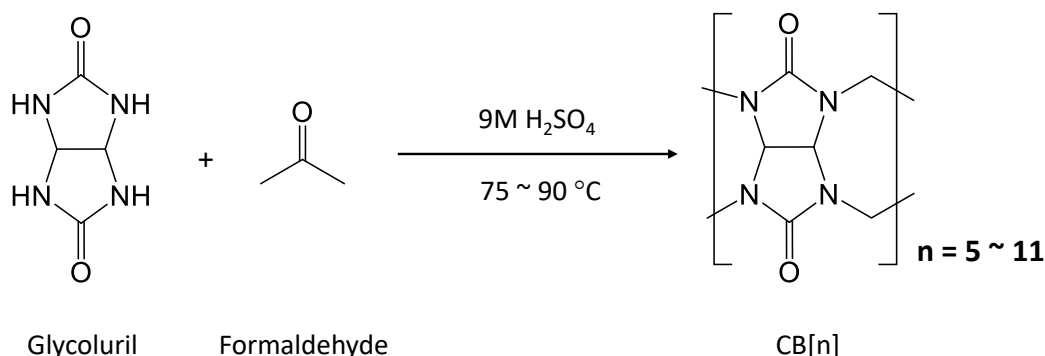


Figure 1.1 The synthesis routes by reacting glycoluril and formaldehyde to prepare CB[n] homologues. n represents the number of glycoluril units.

Among all the synthetic host molecules, the cucurbituril family continued to expand and gain recognition since the first ever-known hexameric macrocyclic compound, cucurbit[6]uril (CB[6]), was introduced in 1905.¹⁴ The CB[6] molecule was collected from the acid-catalyzed condensation reaction between glycoluril and formaldehyde at elevated temperature ($> 110\text{ }^\circ\text{C}$). By means of various spectroscopic characterizations (i.e., ^1H NMR, FTIR, and X-ray crystallization), it was confirmed to be a symmetric pumpkin-shape molecule consisting of six glycoluril units connected with methylene bridges. However, its poor solubility and the lack of chemical methods in introducing functional groups slowed down its development until its homologues were successfully synthesized, isolated, and characterized in 2003.¹⁵ As pointed out by Kim et al, a low reaction temperature is the key for obtaining other homologues as shown in Figure 1.1. The acquired product mixture was isolated by series of dissolution and fractional recrystallization to give 10 – 15% CB[5], 50 – 60% CB[6], 20 – 25% CB[7], 10 – 15% CB[8], and a trace amount of higher homologues (CB[n], $n = 9 - 11$) as identified by NMR and ESI-MS.¹⁵ Their structural geometry and associated parameters are summarized in Figure 1.2. Though the reaction mechanism is not clearly known, it is generally accepted that the final pumpkin-shape structure is cyclized from the generated linear oligomeric products formed between the glycoluril and formaldehyde in the initial acid condensation.¹⁶

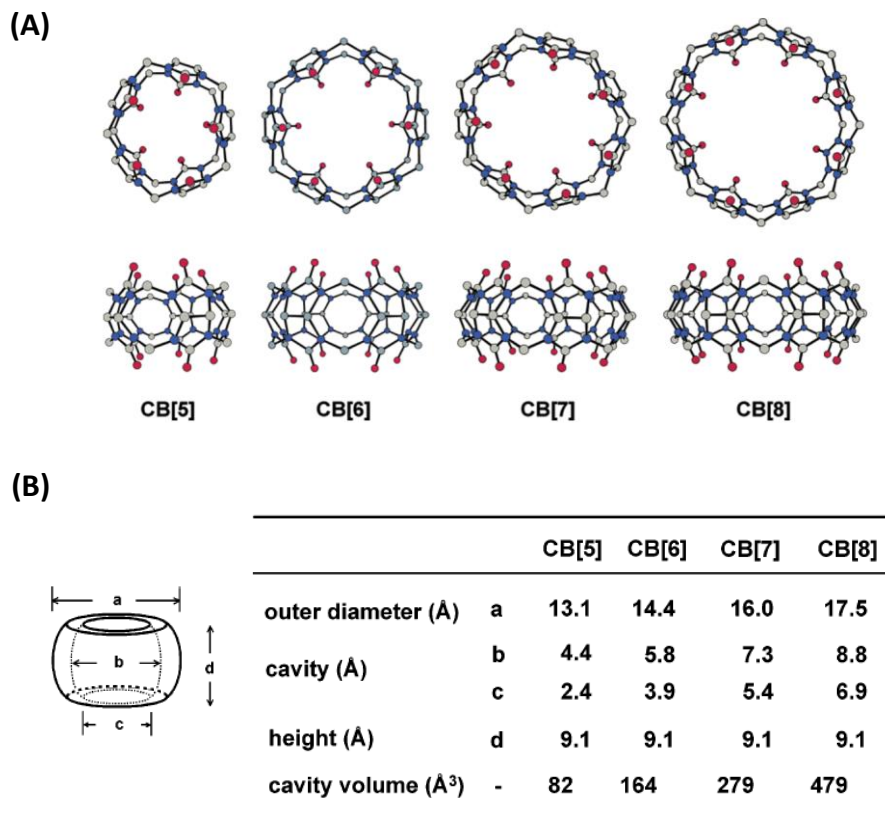


Figure 1.2 (A) Top and side view of the crystallographic structure of CB[6]. Color codes: gray, carbon; blue, nitrogen; red, oxygen. (B) Diameters of the synthetic cucurbituril homologues.

Note: Adapted with permission from Ref 15. Copyright (2003) *American Chemical Society*.

Their highly symmetric structure with a hydrophilic portals (carbonyl portals) and a hydrophobic cavity provide them with unique recognition properties which are not found in other macrocyclic hosts.¹⁷ Though CB[6] is the first member of the cucurbituril family and all other homologues share same characteristic features (e.g., hydrophobic cavity and hydrophilic carbonyl portals), CB[7] has drawn much attention in host-guest chemistry due to the outstanding physical and chemical properties. It possesses some features that separate it from the rest of the family members. Unlike CB[6] and CB[8], which has a solubility in common solvents lower than 10^{-5} M, CB[7] (as well as CB[5]) has a moderate solubility in water (20 – 30 mM).^{2,15} As postulated by Ripmeester et al., such a difference may be caused by the “odd-even effect”, with which CB[5] and CB[7] are less prone to self-association by forming fewer inter-cucurbituril CH---O between the protons on the outer rings of one CB[7] and the carbonyl oxygens on the other; thus, more H-bonding

with water molecules and more soluble.¹⁸ Moreover, the measured ring strain energy of CB[7] is the second lowest compared to other homologues because of the least deviation from the regular sp^3 methylene bridge bond angle upon ring formation (cyclization).^{15,19} The relatively low “ring strain” energy ensures the stability of CB[7] and may explain the low yield of other CB[n] hosts.¹⁵ It also should be noted that the volume of the internal cavity increases as more glycoluril units are incorporated in CB[n] analogues (Figure 1.2B), which determines their ability to bind specific types of guest molecules.¹⁵ This is significant for CB[7] as it can form very stable complexes at a 1:1 ratio with neutral and cationic ferrocene (Fc) derivatives, which are redox-active and allow for accurate quantitative electrochemical-related applications to be developed.^{2,20–22} On the other hand, the internal volume of CB[6] is too small to accommodate Fc derivatives; whereas, CB[8] has a larger cavity to accommodate two guest molecules to form 1:1:1 or 1:2 complexes.^{2,15}

1.1.2. Comparison and Contrast: CB[7] vs. β -CD

β -cyclodextrin (β -CD) is a naturally occurring macrocyclic molecules that resulted from the enzymatic reaction between cyclodextrinase and starch.^{23,24} And in terms of cavity size, CB[7] and β -CD are not too different from each other (279 \AA^3 vs. 262 \AA^3).^{15,20,25} Though they are similar in size, their binding affinities are very different. The binding constants of β -CD towards guest molecules are in the range of 10^3 - 10^4 M^{-1} regardless of the charge on the guests, whereas CB[7] can form exceedingly stable complexes toward neutral and cationic ferrocene derivatives in the range of 10^9 - 10^{15} M^{-1} .^{2,20–22} The significant difference in the binding affinity between them certainly correlates with their chemical composition and the associated electrostatic potential profile. β -CD is composed of glucopyranose subunits with one cavity opening lined by secondary hydroxyl groups that is larger than the other one lined with primary hydroxyl groups (Figure 1.3A). As shown in Figure 1.3B, none of these two asymmetrical hydroxyl openings exhibit strong electronegative properties.²⁰ This is in sharp contrast to the CB[7] (Figure 1.3B) where both of the symmetrical carbonyl portals are highly electronegative.^{2,20} Therefore, besides

the conventional hydrophobic interactions found in both macrocyclic hosts, additional non-covalent interactions (i.e., ion-dipole interaction and H-bonding) can be established between the positive charges on the guest and the electronegative carbonyl portals of the CB[7], leading to a much more favored complexation.²⁶ This actually contributes to the remarkable molecular recognition properties of CB[n], which the β -CD is lacking.

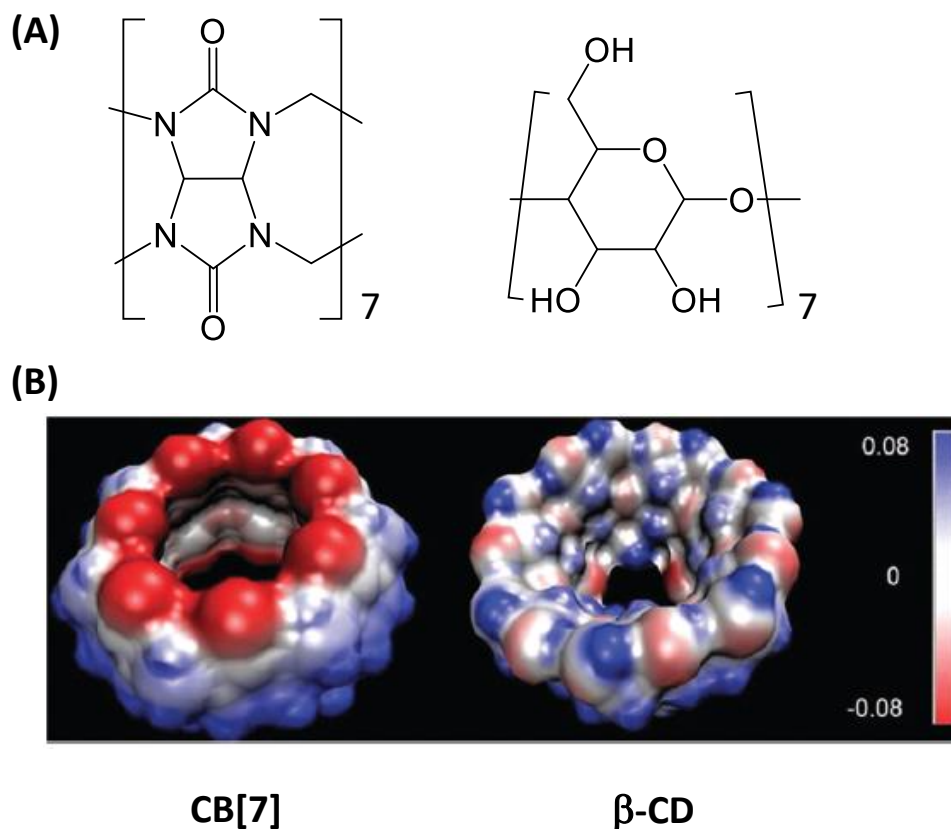


Figure 1.3 (A) Structures of CB[7] and β -CD. (B) Surface electrostatic potential for CB[7] and β -CD. The colored bar on the far right describes the electronegativity from negative (red) to positive (blue).

Note: (B) reprinted with permission from Ref 2. Copyright (2015), *Royal Society of Chemistry*.

1.1.3. In-solution Fc@CB[7] host-guest complexation

Several guest molecules that can form inclusion complexes with CB[7] hosts at 1:1 ratio, such as ferrocene (Fc),^{15,20,27–29} cobalotocene,³⁰ bicyclooctane derivatives,^{31,32}

diamantine,^{33,34} and adamantane.^{32,35} Fc guest is particularly significant due to its favorable electrochemical properties (e.g., reversible oxidation-reduction behavior and high stability),³⁶ low cost, and easy synthesis. Fundamental studies on probing the formation of CB[7] inclusion complexes with Fc derivatives of distinct structural features have been performed by means of cyclic voltammetry (CV) in conjunction with advanced spectroscopic techniques (X-ray crystallography, ¹HNMR, and ¹³CNMR, MS-TOF).²⁰⁻²²

Similar to other guests, the binding affinity between Fc and CB[7] is ascribed to their size-shape complementarity (i.e., geometric match between the Fc aromatic cyclopentadienyl (Cp) rings and the hydrophobic CB[7] inner cavity), hydrophobic interactions, and ion-dipole interaction, if applicable.^{2,37} Figure 1.4A shows an X-ray crystal structure of a Fc residing within the CB[7] chamber upon encapsulation. The result reveals that Fc possess some rotational freedom inside the cavity, and that it adopts two independent positions in CB[7] with angles at 79° (more energetically favorable) and 22°, respectively; these angles are measured between the main axis of Fc (across the center of the two Cp ring) and CB[7] (across the center of the two carbonyl portals).²⁰ However, it should be noted of that this is not a generalized case as substituents on the Fc core would impact the overall complexation. By incorporating two cationic trimethylammoniummethyl (-CH₂-N⁺-(CH₃)₃) substituents to one of the Cp rings, the main axis of Fc tilts 43.7° relative to the main axis of CB[7] (Figure 1.4B).²⁸ This is not surprising as the tilting allows both cationic arms to protrude through the CB[7] cavity and interact with the electronegative carbonyl portals; such ion-dipole interactions indeed ensure a much stronger host-guest binding.^{2,28} Moreover, the deviation from the commonly observed enthalpy-entropy compensation for synthetic host-guest complexation systems permits the extreme affinity, in which the decrease (unfavorable) in entropy due to conformational restriction upon complexation is compensated by a large entropy gain from desolvation.^{2,28} This is attributed to the cavity volume of CB[7] that prevents the internal water molecules (7 ~ 8) from establishing energetically stable H-bond networks; therefore, the complete release of these high-energy water molecules to the bulk solution lead to a high energy gain, giving rise to the total change in ΔS .^{2,28}

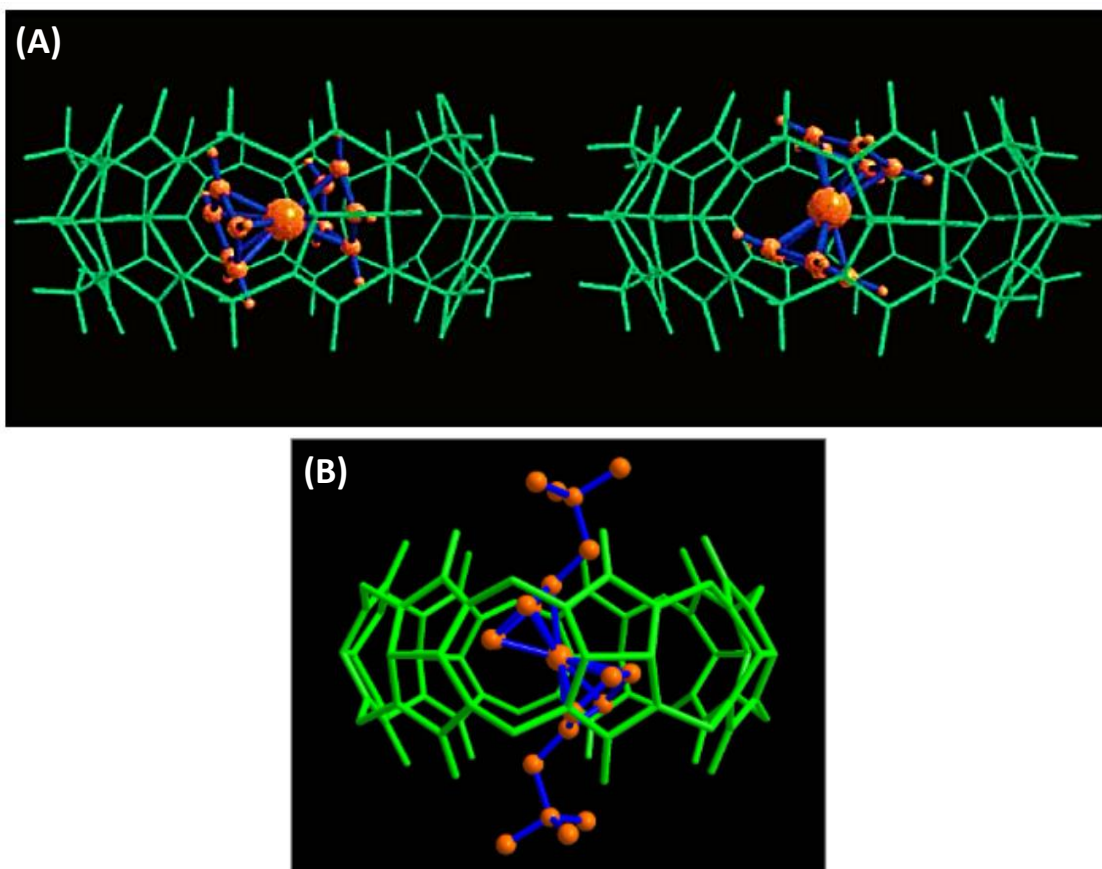


Figure 1.4 (A) X-ray crystal structure showing the Fc adopts two orientations inside the CB[7] host cavity. These relative position angles are 79 and 22°, respectively. (B) X-ray crystal structure showing the orientation of a dicationic Fc derivatives (bis(trimethylammoniomethyl)ferrocene), which resides within the CB[7] chamber at a relative position angles of 43.7°.

Note: (A) Reprinted with permission from Ref 20. Copyright (2005), *American Chemical Society*. (B) reprinted with permission from Ref 28. Copyright (2007), *The National Academy of Sciences of the USA*.

The difference in the binding affinities between Fc derivatives and CB[7] can be investigated by performing conventional electrochemical studies in solution. As shown in Figure 1.5, a decrease in the overall current has been observed upon successful host-guest complexation.^{20–22} This is attributed to the bulk size and hydrodynamic radius of CB[7] that affects the effective diffusion coefficient of the free Fc derivatives upon complexation.²⁰ Additionally, the observation of the positive shift (~ 110 mV) in the corresponding $E_{1/2}$ upon host-guest complexation reveals that Fc with a positively charged substituent established a much stronger interaction with CB[7], i.e., the ferrocene form of the monocationic Fc derivative is more stable than the ferrocenium form (Figure 1.5A).

In contrast, only a minor shift in $E_{1/2}$ (~ 4 mV) was noted with the neutral Fc guest (Figure 1.5B), which reflects the minimal effect of CB[7] stabilization.^{20,21} These results confirm the enhanced binding stability for Fc@CB[7] when positively charge substituents are incorporated into the Cp ring of Fc. With other spectroscopic techniques, e.g., ^1H NMR, and ^{13}C NMR, the binding affinity of CB[7] toward other Fc derivatives in solution have been confirmed to be in the range of 10^7 - 10^{15} M^{-1} (Figure 1.6). In contrast, the binding between CB[7] and anionic ferrocene (deprotonated ferrocenecarboxylic acid, FcCOO^-) is negligible, mainly due to the strong electrostatic repulsion exerted from the carbonyl portals to the negatively charged substituent.²⁰

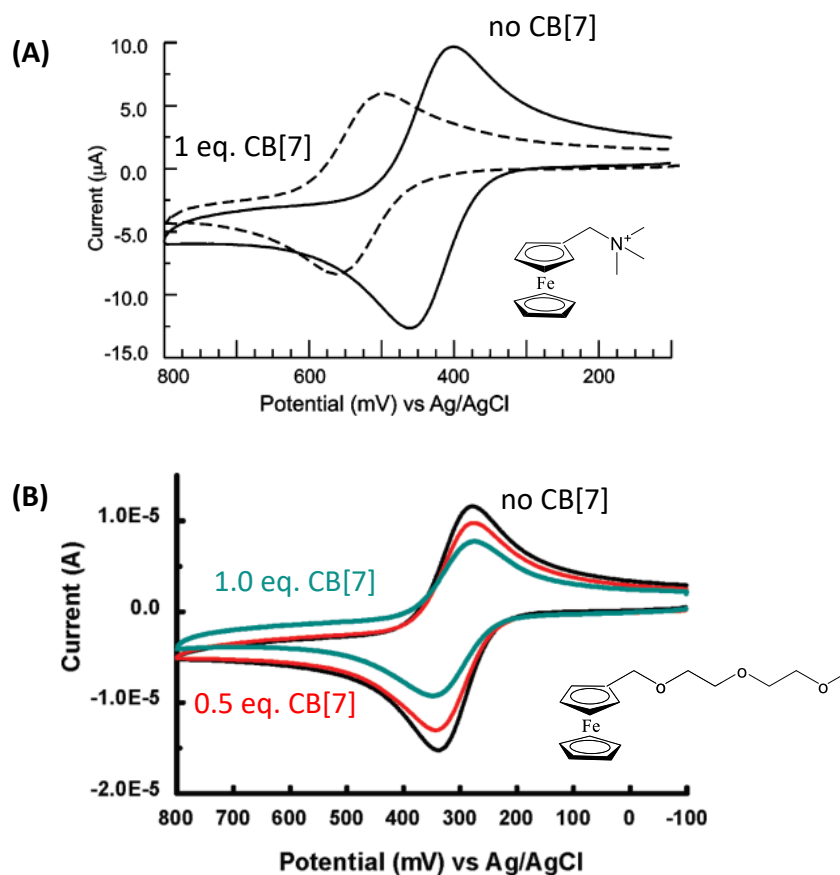
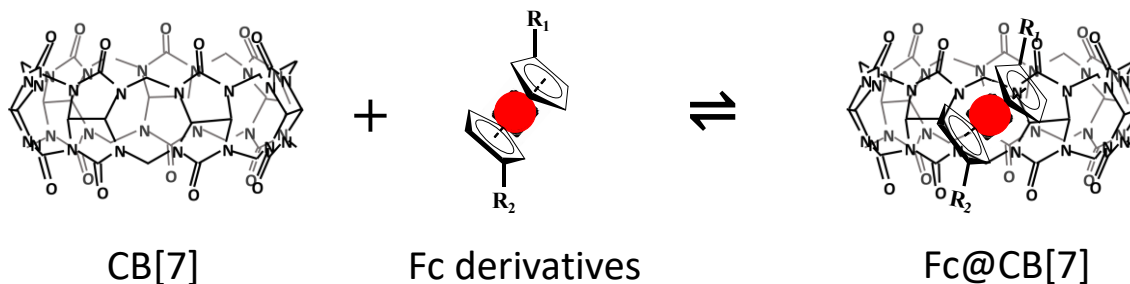


Figure 1.5 Cyclic voltammetric responses of (A) monocationic Fc derivatives and (B) mono-substituted neutral Fc derivative before and after adding an equivalent amount of CB[7]. Scan rate was kept at 0.1 V/s.

Note: (A) Reprinted with permission from Ref 20. Copyright (2005), *American Chemical Society*. (B) Reprinted with permission from Ref 21. Copyright (2009), *American Chemical Society*.



	R1	R2	K_f (M^{-1})
F1	-CH ₂ OH	-H	(3.2 0.5) 10 ⁹
F2	-CH ₂ OH	-CH ₂ OH	7.4 10 ⁶
F3	-CH ₂ (O(CH ₂) ₂) ₂ OCH ₃	-H	1.4 10 ⁷
F4	-CH ₂ (O(CH ₂) ₂) ₂ OCH ₃	-CH ₂ (O(CH ₂) ₂) ₂ OCH ₃	3.6 10 ⁶
F5	-CH ₂ N ⁺ H(CH ₃) ₂	-H	(2.4 0.8) 10 ¹²
F6	-CH ₂ N ⁺ (CH ₃) ₃	-H	(4.1 1.0) 10 ¹²
F7	-CH ₂ N ⁺ (CH ₃) ₃	-CH ₂ N ⁺ (CH ₃) ₃	(3.0 1.0) 10 ¹⁵

Figure 1.6 Formation constants (K_f) of CB[7] towards some Fc derivatives with different structural features upon Fc@CB[7] host-guest inclusion complexes in solution.

Note: F1, and F5 - F7 are from Ref 2, and F2 – F4 are from Ref 21. F2 – F4 are relative K values measured by ¹HNMR via a competition experiment with cobaltocenium.

1.1.4. Interfacial Fc@CB[7] host-guest complexation

For the ultrahigh binding affinity, various Fc@CB[7] complexes have been explored as immobilization motifs for the development of biosensor.^{10,38–40} However, their host-guest binding properties on surface have been rarely investigated, which is partially due to the challenges of the current CB[7] immobilization methods (particularly the low solubility of CB[7] in common organic solvents). Therefore, research efforts on derivatizing CB[7] have been devoted to attach desired functional groups for improved solubility and reactivity. To date, the derivatization has been achieved via three strategies; (1) using substituted glycoluril in the acid-catalyzed condensation reaction (Figure 1.1);^{41,42} (2) oxidizing the equatorial hydrogens using a strong oxidant (e.g., potassium

persulfate) to generate hydroxyl groups;⁴³ and (3) preparing a monohydroxy-CB[7] via irradiating its mixture with H₂O₂.^{44,45}

The successful derivatization of CB[7] enables its chemical immobilization on solid surfaces for developing biosensors and devices. For example, allyloxy-functionalized CB[7] can be covalently attached to a vinyl-terminated self-assembled monolayers (SAMs) prepared on gold via olefin metathesis reaction;¹⁰ hydroxylated CB[7] can react with N-hydroxysuccinimidyl Sepharose beads;⁴⁰ allyloxy-functionalized CB[7] can be attached to a thiol-terminated silicon surface via thiol-ene “click” reaction.⁴⁶ Nonetheless, the reaction conditions are not satisfying as they either require specific organic solvents or prolonged reaction time to complete, and in some cases a specific reaction chamber is needed to assist the reaction.^{40,46,47}

At the same time, the discovery of the replacement of citric acid ligands by acetone on gold nanoparticles leads to the idea of direct deposition of non-derivatized CB[7] on gold surfaces.⁴⁸ Though the spectroscopic characterizations (FTIR, XPS) indicate that the CB[7] orientate themselves perpendicularly with respect to the gold surface, the subsequent CV studies revealed the drawbacks of such monolayers. The rather large capacitive currents⁴⁸ confirm that the coverage of CB[7] on surface is low, non-uniform, and not stable, which in turn, jeopardizes the overall quality of the monolayer for further application development.

Our group started to tackle the challenges of immobilizing CB[7] for studying interfacial Fc@CB[7] host-guest complexation at molecular interfaces a few years ago.³⁷ Instead of directly immobilizing CB[7] onto a surface, a Fc-terminated SAMs (Fc-SAMs) on gold was formed first (Figure 1.7). By carefully “titrating” the Fc-SAM with CB[7] in the micromolar range and measuring the corresponding electrochemical signal, they were able to determine the formation constant (K_f), $(7.3 \pm 1.8) \times 10^4 \text{ M}^{-1}$, based on the law of mass action.³⁷ Further kinetics studies revealed that the slow dissociation rate constant ($k_d = (1.3 \pm 0.2) \times 10^{-3} \text{ s}^{-1}$) may be the major factor for the overall stabilization of the interfacial Fc@CB[7] complex. It was pointed out that these values may not accurately reflect the true host-guest binding nature at interface as the formation of Fc clusters and

the partially folding of the Fc-terminated thiols within the binary SAMs can prevent their complexation. In this case, the surface-immobilized Fc lacks of rotational freedom for adopting the most energetically favorable orientation within the CB[7] chamber upon complexation.³⁷

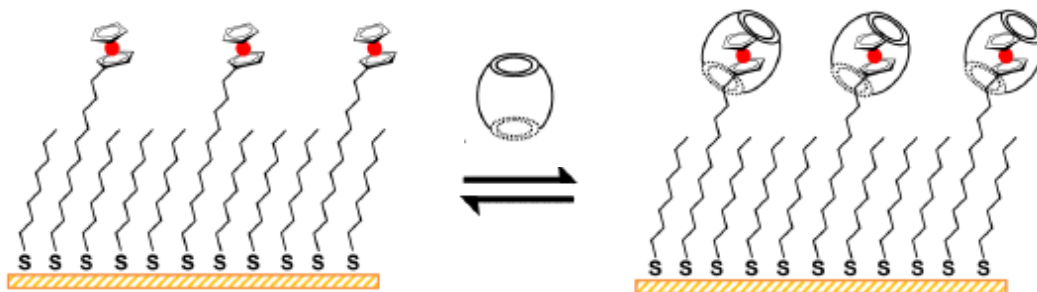


Figure 1.7 Host-guest binding of CB[7] toward surface-immobilized Fc at a molecular interfaces. The binary SAMs are made from 11-Ferrocenyl-1-undecanethiol and 1-octanethiol.

Note: Reprinted with permission from Ref 37. Copyright (2017), *American Chemical Society*. Slight modifications were made to the figure.

1.2. Self-Assembled Monolayers (SAMs)

Self-assembled monolayers (SAMs) are single layers of organic molecules (typically 1 ~ 3 nm thick) formed spontaneously from the solution or the gas phase on a surface.⁴⁹ This surface is not limited to noble metals but extend to metal oxides, silicon, and even liquid metals, like mercury. It has been shown experimentally that properly formed SAMs are densely packed with high degrees of orientation and molecular order.⁵⁰ Upon SAMs' formation, the chemical and physical properties of the surface can be altered to have desirable functionalities for fundamental studies and application development, such as colloid science, material science, and microelectronic devices.^{49,51} Furthermore, with the growing interests in the development of DNA-based biosensors, surface immobilization of DNA strands of various lengths and sequences have been explored via incorporating thiolated DNA into a monolayer of alkanthiolates on gold surfaces.^{52,53}

1.2.1. Alkanethiolate SAMs on gold

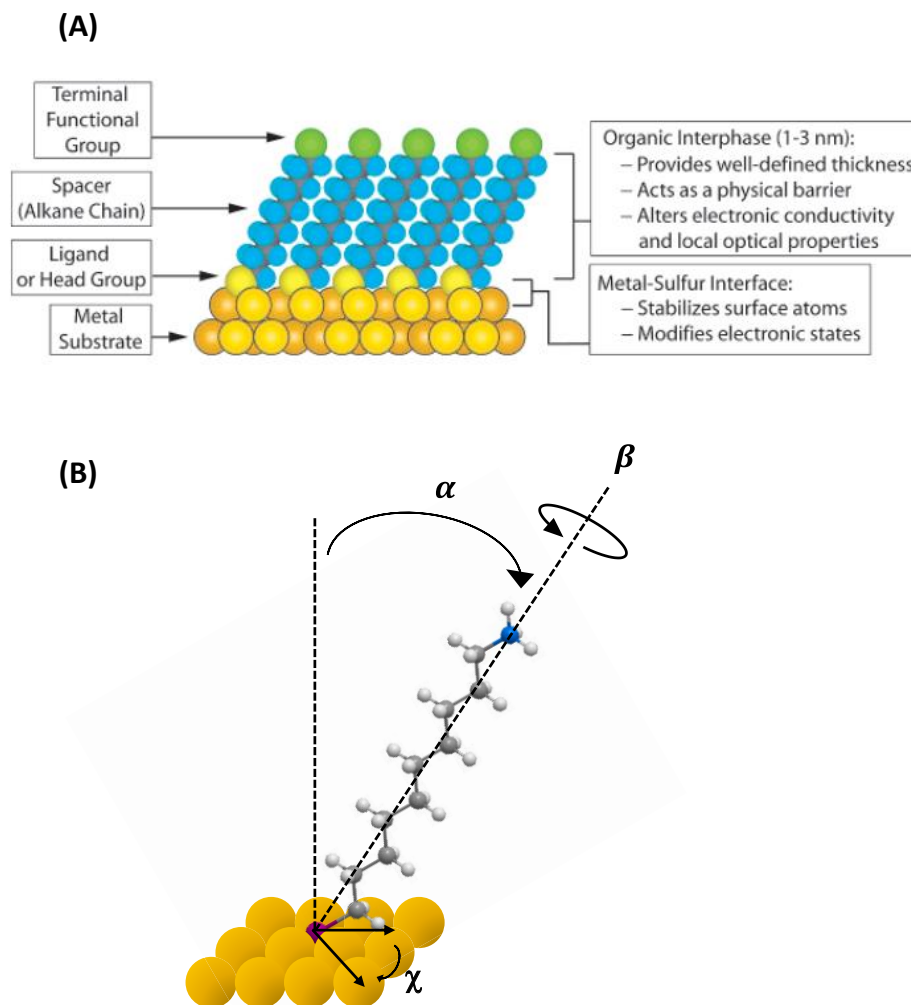


Figure 1.8 (A) Illustration of an ideal single-component SAM of alkanethiolates formed on gold (111) surface. (B) Orientation of single long-chain alkanethiol adsorbed on gold (111) with defined tilt angle (α), rotation angle (β), and projection angle (χ). Typically, $\alpha = 30^\circ$, $\beta = 55^\circ$, and $\chi = 14^\circ$. The purple atom is sulfur and the blue atom is the carbon from the end methyl group of the alkanethiol.

Note: (A) is adapted with permission from Ref 49. Copyright (2005), *American Chemical Society*.

SAMs of alkanethiols on gold have been extensively studied. The ordering of alkanethiols into a highly oriented “assembly” is driven by two dominant factors, the strong affinity between the sulfur and gold (100 ~ 200 kJ/mol),⁵⁴ and the lateral van der Waals interactions (4 ~ 8 kJ/mol per methylene unit for long carbon chain).⁵⁵ As illustrated in Figure 1.8A, long chain alkanethiols are adsorbed on Au (111) with the hydrocarbon chains

tilted to an particular angle. This maximizes the overall van der Waals interactions between alkane chains and ensures the most effective packing.⁵⁶ The orientation is defined by three parameters (Figure 1.8B), the tilt angle (α , the angle between the surface normal and the alkanethiol backbone); the twist angle (β , along the axis of alkanethiol backbone); and the precession angle (χ , molecular projection).⁵⁶ Upon forming SAMs atop, the wettability of the gold surface is altered depending on the polarity of the terminal groups (e.g., $-\text{CH}_3$ for hydrophobic, and $-\text{COOH}$ for hydrophilic).⁵⁶ Furthermore, SAMs on solid substrates have been widely used for preventing metal cations in the electrolyte from non-specifically adsorbing on the electrode surface.⁵⁷ In addition, alkanethiolate SAMs with redox-active terminal groups have been adapted to study long-range electron transfer kinetics and to determine associated parameters (e.g., the tunneling constant, electronic coupling coefficient, and electron transfer rate constant).⁵⁸

Other substrates in addition to gold have been explored to “support” SAMs. However, they are either less studied or less well accessible compared to gold, or they are susceptible to external influence (Table 1.1). Yet, it would be biased to conclude that gold is the best substrate among other options. Whitesides and coworkers pointed out that five distinctive characteristics make the gold substrate stands out:⁴⁹ (1) they can be easily fabricated, i.e., readily prepared by vapor deposition, sputtering, or electrodeposition, and commercially availability; (2) they can be patterned by a combination of lithographic tool and chemical etchants; (3) they can be handled under ambient conditions; (4) they can be used as substrates for various spectroscopic (e.g., surface-plasmon resonance spectroscopy, infrared spectroscopy, and ellipsometry) and electrochemical techniques (e.g., cyclic voltammetry); and (5) they can be used as substrates for supporting biological systems.

Table 1.1 Pros and cons of commonly used solid substrates for supporting SAMs.

Solid Substrate	Pros	Cons
Gold	<ul style="list-style-type: none"> - Inertness in the presence of almost all reagents but form strong bonding with thiols (in turn make high-quality SAMs) - Ideal for electrochemical and spectroscopic studies⁵⁹ 	<ul style="list-style-type: none"> - Expensive
Silver	<ul style="list-style-type: none"> - Produce high-quality SAMs with relatively simpler structure⁶⁰ 	<ul style="list-style-type: none"> - Oxidized readily in air - Toxic to cells⁶¹
Copper	<ul style="list-style-type: none"> - High electromigration resistance - High thermal stability and conductivity⁶² 	<ul style="list-style-type: none"> - oxidized readily in air⁶²
Palladium	<ul style="list-style-type: none"> - Relatively smaller grains (better candidate for preparing micro- and nanostructures)⁶³ - Offer catalytic properties - Biocompatible⁶¹ - Stable at room temperature⁴⁹ - Cost-effective 	<ul style="list-style-type: none"> - Much less studied compared to gold⁴⁹ - More expensive compared to gold substrate
Platinum	<ul style="list-style-type: none"> - Larger overpotential of gold for hydrogen reduction⁵⁹ - Easily moldable - Offer catalytic properties - Anti-corrosion 	<ul style="list-style-type: none"> - SAMs degrade and oxidized severely after one month⁶⁴
Mercury	<ul style="list-style-type: none"> - Defect-free - Renewable (by washing) - Molecularly smooth surface⁵⁰ 	<ul style="list-style-type: none"> - Must be handled with extreme care (toxic) - Narrow potential window due to mercury oxidation⁶⁵

The typical approach of preparing SAMs on gold for fundamental studies or applications is to create binary SAMs so that the desired functional groups are uniformly dispersed on the surface (Langmuir-type adsorption process).⁶⁶ The two conventional methods (co-adsorption and post-assembly exchange) are illustrated in Figure 1.9. It has been found that these two methods result in very different molecular heterogeneity in the mixed SAMs.⁶⁷ Indeed, the difference in chain lengths, terminal groups (e.g., polarity, solubility) of the thiols, the mole ratio in the co-assembly solution, and the time of exchange process in the post-assembly exchange method all contribute to the final distribution/composition of the binary SAMs on gold.^{60,68,69}

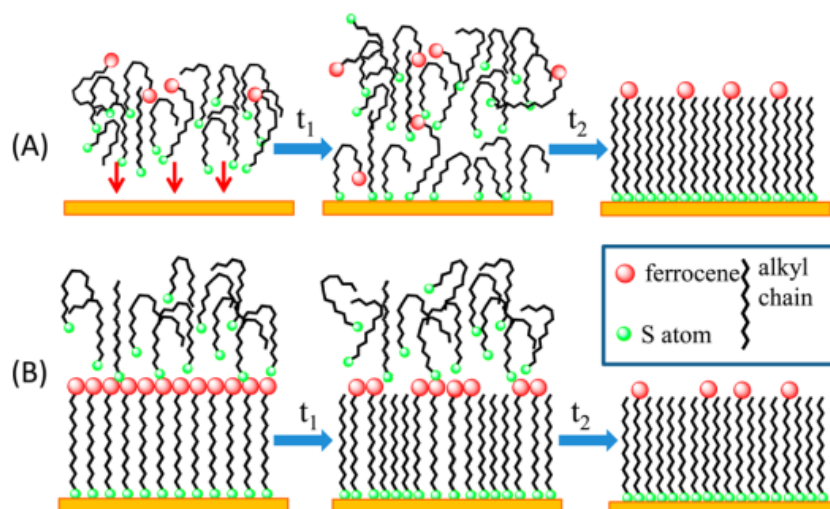


Figure 1.9 Schematic diagrams of (A) co-adsorption, in which the gold substrate is incubated in a binary solution of the two thiols and (B) Post-assembly exchange, in which the gold substrate is treated in a thiol followed by a subsequent treatment with another precursor.

Note: Reprinted with permission from Ref 67. Copyright (2014), *American Chemical Society*.

1.2.2. Formation of thiolated DNA SAMs on gold and the challenges

Another emerging field of SAMs is the assembly of thiolated DNA strands on gold for the purpose of molecular sensing. In combination with electrochemical techniques, many biological recognition events (from hybridization to DNA/protein interactions) can

be efficiently converted to analytical signals for the analyte quantitation. The highly programmable nature of new selection tools (e.g., “SELEX”) promotes the search for new functional DNA modules that can be confined to gold as novel sensing platforms. Examples include the detection of cocaine using highly selective aptamers;⁷⁰ quantitation of potassium ions using a G-quadruplex;⁷¹ and the detection of thrombin in diluted blood serum with a rationally designed coupled-ligand deoxyribosensor.⁷² All of these have been accomplished by monitoring redox reactions occurring on the electrode surface, from which the variation in the currents associated with immobilized DNA probes (tethered with redox moieties), either conformationally or structurally.

Traditionally, DNA biosensors are prepared by tethering one end of the thiolated oligonucleotides on gold via thiol-gold interactions followed by the passivation with mercaptohexanol (MCH) to remove non-specifically adsorbed oligonucleotides (through base-pair adsorption on gold) and lower their density across the surface (Figure 1.10).^{53,73} This has been thought to be an “ideal” sensing surface that targets would be able to access and interact with each of the surface-bound oligonucleotides. However, morphology characterizations have confirmed that traditional methods failed to reproducibly produce a homogeneous surface as clusters and aggregates of the oligonucleotides present.⁷⁴ This was examined by incorporating a dual-labeled ssDNA, which has a thiol at the 5’ – end for tethering on gold and a fluorescent tag on the 3’- end.⁷⁴ Shown in Figure 1.11 are fluorescence images of three independent samples: two prepared strictly followed the traditional ssDNA/MCH method (Figure 1.10) and the other prepared in a reverse order (MCH/ssDNA).⁷⁵ It is clear that even prepared from the same method (Figure 1.11A), the surface morphologies of two ssDNA/MCH samples appear very different and are highly heterogeneous with some regions high in DNA densities than others, which reflects the low reproducibility of the traditional DNA surface immobilization method. Similarly, treating the MCH SAMs with ssDNA appear nonuniform as well, i.e., with small regions of high fluorescent specks (Figure 1.11B), which indicates that the preferential exchange occurs at defects of the SAM surface. Nevertheless, several new surface preparation methods have been explored lately, such as, employing the ratiometric approach by incorporating two redox-active tags on the same DNA at different positions (more details in Section 5.2)⁷⁶,

or using a DNA tetrahedron structure with pendant probe DNA at one vertex and three thiol groups at the other three vertices on the same plane for improved spacing.⁷⁷

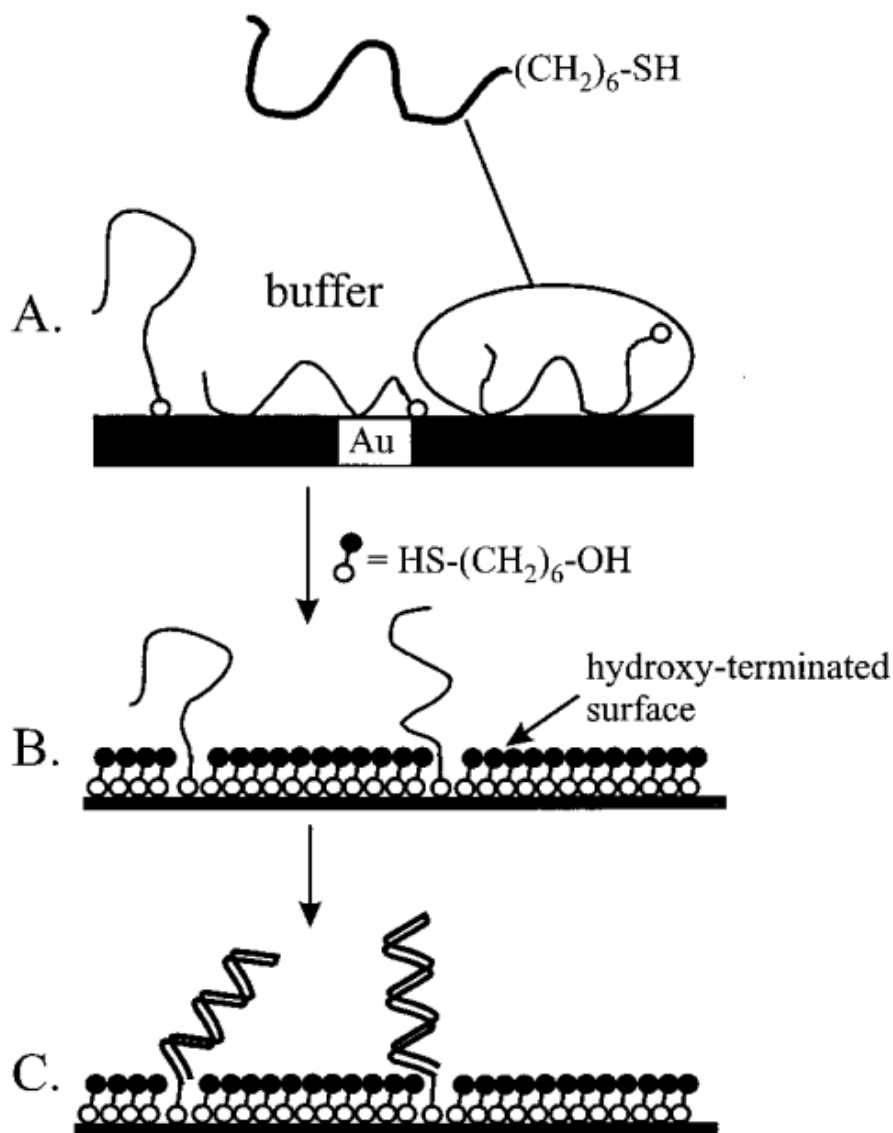


Figure 1.10 Schematic diagram of preparing thiolated DNA monolayers on gold. (A) Thiolated single-stranded DNA (HS-ssDNA) adsorbed on gold surface via the thiol-gold and backbone-gold interactions. (B) Adsorption of mercaptohexanol (MCH) displacing non-specifically adsorbed DNA and preventing the interaction between the DNA backbone and gold surface. (C) Hybridization of complementary strands on the prepared DNA/MCH SAMs.

Note: Reprinted with permission from Ref 53. Copyright (1998) Not subject to U.S. Copyright, *American Chemical Society*

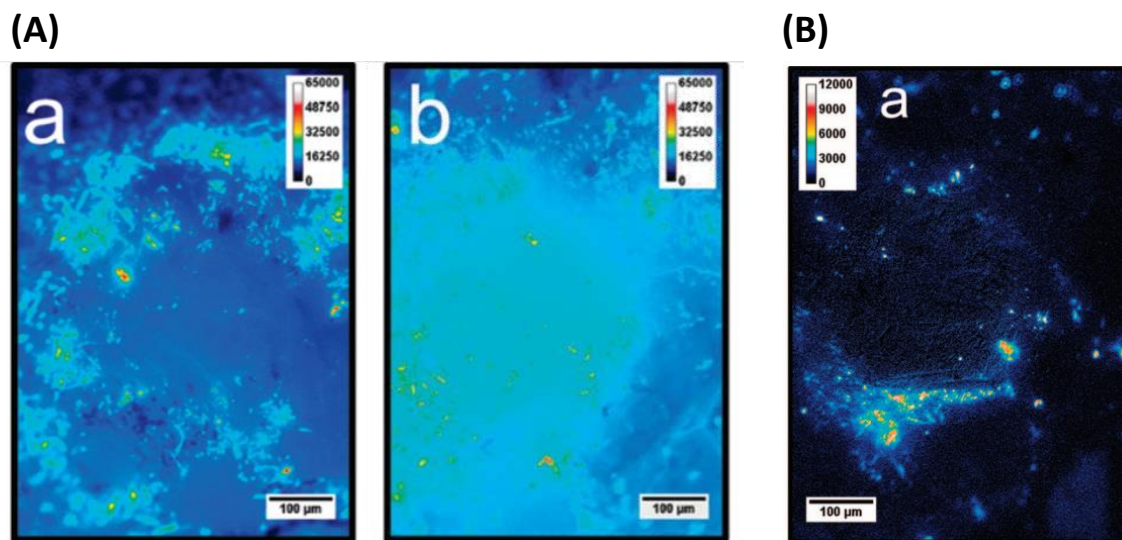


Figure 1.11 Fluorescence images taken at open circuit potential of independently prepared fluorescent-labelled (A) (a) ssDNA/MCH modified gold surfaces, (b) another example of a ssDNA/MCH layer, and (B) (a) MCH/ssDNA layer. The intensity of fluorescence is rendered as a range of colors, shown in the color-intensity bar.

Note: Reprinted with permission from Ref 75. Copyright (2009), *American Chemical Society*.

1.3. Click Reaction on Surface

The term “click chemistry” was coined by Sharpless and co-workers in 2002;⁷⁸ to be considered as a “click” reaction, certain characteristics must be fulfilled: (1) easily accessible reagents, (2) no need of a solvent or a solvent that is benign (e.g., water), (3) insensitive to oxygen, (4) high yield, (5) stereospecific products, and (6) easily removable by-products without the need of chromatographic techniques.⁷⁹ These features are attributed to the high thermodynamic driving force ($> 20 \text{ kcal mol}^{-1}$), promoting the reaction to reach the completion with high selectivity.⁷⁸ Four major types of click reactions have been identified, including cycloaddition (Cu(I)-catalyzed Huisgen 1,3-dipolar cycloaddition of azide-alkynes); nucleophilic ring-openings (openings of strained heterocyclic electrophiles); non-aldol carbonyl chemistry (hydrazone/oxime ether formation, and amide/isourea formation); and multiple carbon bond additions (the formation of different three-member rings, and Michael addition).⁸⁰ Among all these

reactions, the Cu(I)-catalyzed azide-alkyne cycloaddition (CuAAC) has proven to be the most effective and widely used method in Click chemistry that nearly 100% of the publications across diverse research areas refer this as the click reaction.⁸⁰

CuAAC reaction is a Huisgen 1,3-dipolar cycloaddition that involves a 1,3-dipole azide-functionalized molecule and dipolarophile alkyne-functionalized molecule to produce a five-member ring in the present of Cu(I) catalyst (Figure 1.12). Before the discovery of Cu(I) catalyst by Sharpless and Meldal, the reaction was depending on elevated temperature and prolonged reaction duration, which results in a mixture of 1,4- and 1,5-triazole regio-isomers.⁷⁹ In comparison, other metal catalysts employed in azide-alkyne cycloaddition, e.g., like Zn(II),^{81,82} and Ru(II),^{83,84} require either challenging reaction conditions or further purification of the products, besides the relatively low yield.

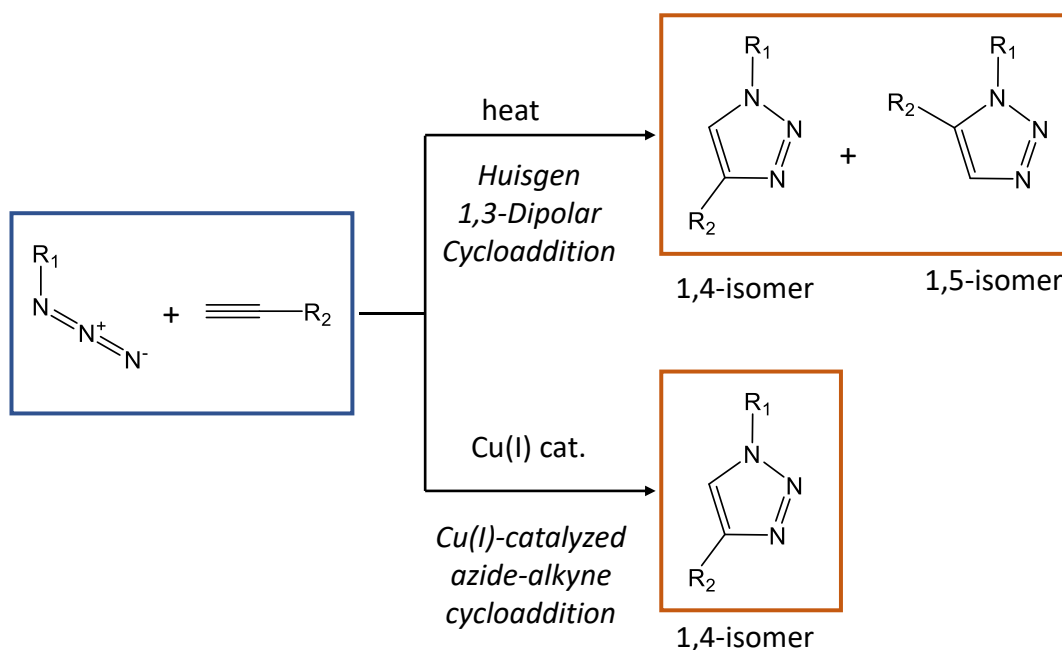


Figure 1.12 Comparison between thermally activated and copper(I)-catalyzed Huisgen 1,3-azide-alkyne cycloaddition.

As for the development of sensors and other molecular electronics, the efficient and convenient immobilization of specific molecules on surface is of practical importance.⁸⁵ Many surface reaction routes fail to do so as they either produce multilayer structures, or require specific reaction conditions (e.g., elevated temperature or photochemical

activation).^{86–88} One of the great characteristics of the CuAAC is that the reaction takes place in a high degree of orthogonal manner, meaning that the specific ligation process can be done even in the presence of other unprotected, complex, and highly reactive molecules.⁸⁹ Thus, this reaction promises efficient route for surface immobilization, which can be performed on silicon, glass, gold, silica gel, and many other solid substrates (Figure 1.13).⁸⁹ Chidsey et al. demonstrated that an azide-modified surface (either gold or silicon) can serve as a versatile platform for attaching various alkyne-functional molecules.^{85,90,91} Moreover, CuAAC reaction has been employed in the field of nanotechnology to address the insolubility problem of carbon nanotubes during the solution phase processing and manipulation for appropriate assemblies.⁹² Particularly by incorporating alkyne-functionalized groups to single-walled carbon nanotubes (SWNTs), azide-terminated polystyrene chains were successfully attached with an overall coverage of 45%; such a modification enables their high solubilities in a wide range of organic solvents.⁹² In addition, CuAAC is suitable for immobilizing biomolecules onto surface giving its mild reaction conditions; Sun et al. attached a variety of azide-labelled protein affinity ligands and proteins on glass for designing chip-based assays and bioactive implant surfaces.⁹³

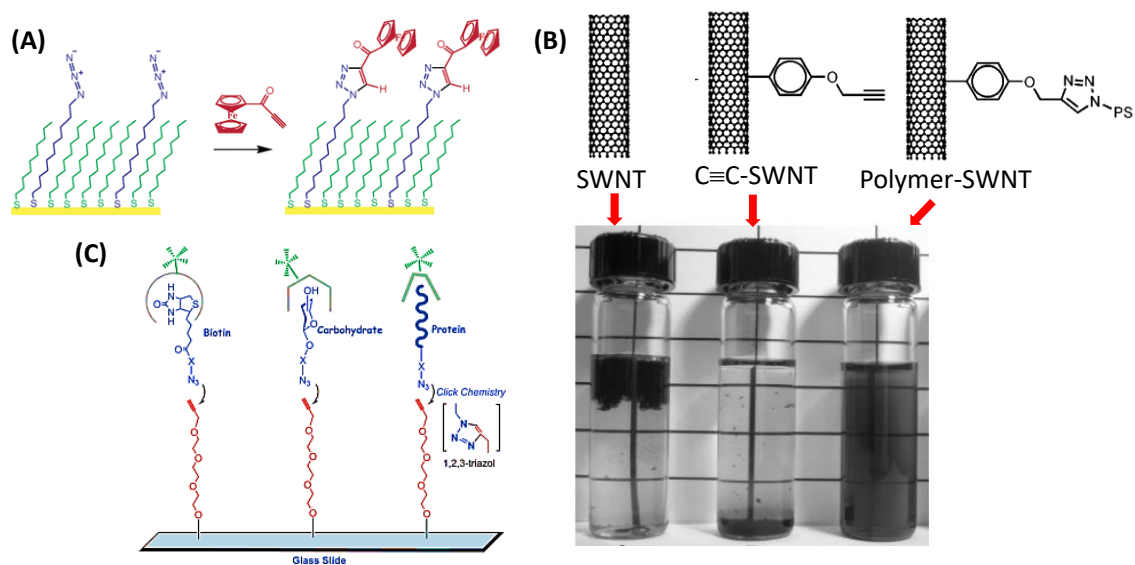


Figure 1.13 Schematic illustrations of performing CuAAC reactions on solid substrates: (A) gold, (B) singled-walled carbon nanotube, and (C) glass.

Note: (A) reprinted with permission from Ref 91. Copyright (2004), *American Chemical Society*. (B) reprinted with permission from Ref 92. Copyright (2005), *American Chemical Society*. (C) Reprinted with permission from Ref 93. Copyright (2006), *American Chemical Society*.

1.4. Motivation and Outline of This Thesis

Because of the ultrahigh in-solution binding stabilities of CB[7] towards neutral and cationic Fc derivatives, these supramolecular complexes have been explored as surface immobilization linkers or structural conjunction motifs in developing biosensors and other molecular devices. However, the formation of supramolecular guest-host complexes on surface have been rarely studied; this is partially due to the challenges in preparing high-quality CB[7]-terminated surfaces (suffering from either poor stability or inconvenient and time-consuming procedure). Therefore, finding a more efficient surface reaction to chemically tether CB[7] on surface is essential for gaining insights into the interfacial complexation of CB[7] and Fc derivatives. In this thesis, the aim is to prepare a stable and well-organized CB[7] monolayer to carry out interfacial guest-host studies. As shown in Figure 1.14, I will explore the feasibility of using CuAAC to chemically tether alkyne-functionalized CB[7] (\equiv -O-CB[7]) onto binary azido SAMs and to characterize thus-formed CB[7] monolayers with both electrochemical and structural techniques. The host-guest recognition ability of such surface-immobilized CB[7] will be subsequently investigated with various ferrocene derivatives, not only to assess their formation thermodynamics/kinetics but also to compare with the previously reported Fc@CB[7] complexation on surfaces.

Beside this introductory chapter that summarizes the relevant literature pertaining to the thesis topic, the thesis includes a chapter on introducing surface characterization techniques, including cyclic voltammetry, Fourier-transform infrared spectroscopy, water contact angle measurements, and X-ray photoelectron spectroscopy. In Chapter 3, I will describe the experimental details of the sample preparation and characterization. Subsequently, results and discussion are presented in Chapter 4. The last chapter is to summarize the key findings and presents the future work.

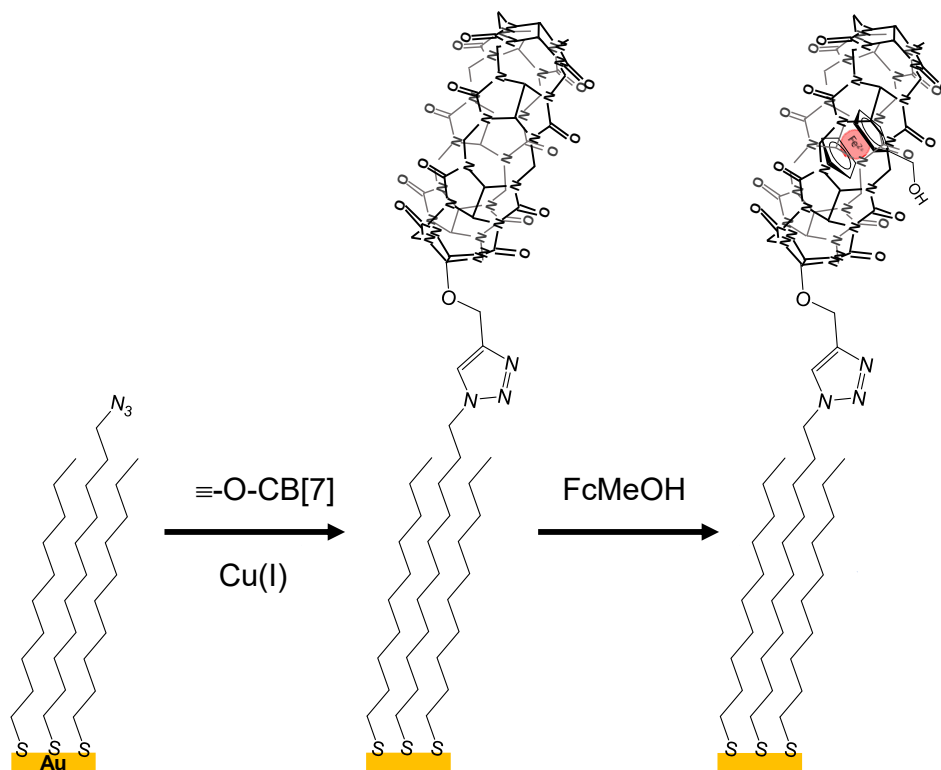


Figure 1.14 Schematic diagram showing chemical attachment of alkyne-functionalized CB[7] (≡-O-CB[7]) onto a binary azide-terminated SAM on gold surface via CuAAC reaction followed by subsequent supramolecular complexation with ferrocenemethanol (FcMeOH).

Note: Reprinted with permission from Ref 118. Copyright (2022), *American Chemical Society*. Slight modifications were made to the figure.

Chapter 2.

Instrumental Techniques

2.1. Cyclic Voltammetry (CV) and Electrochemical Cells

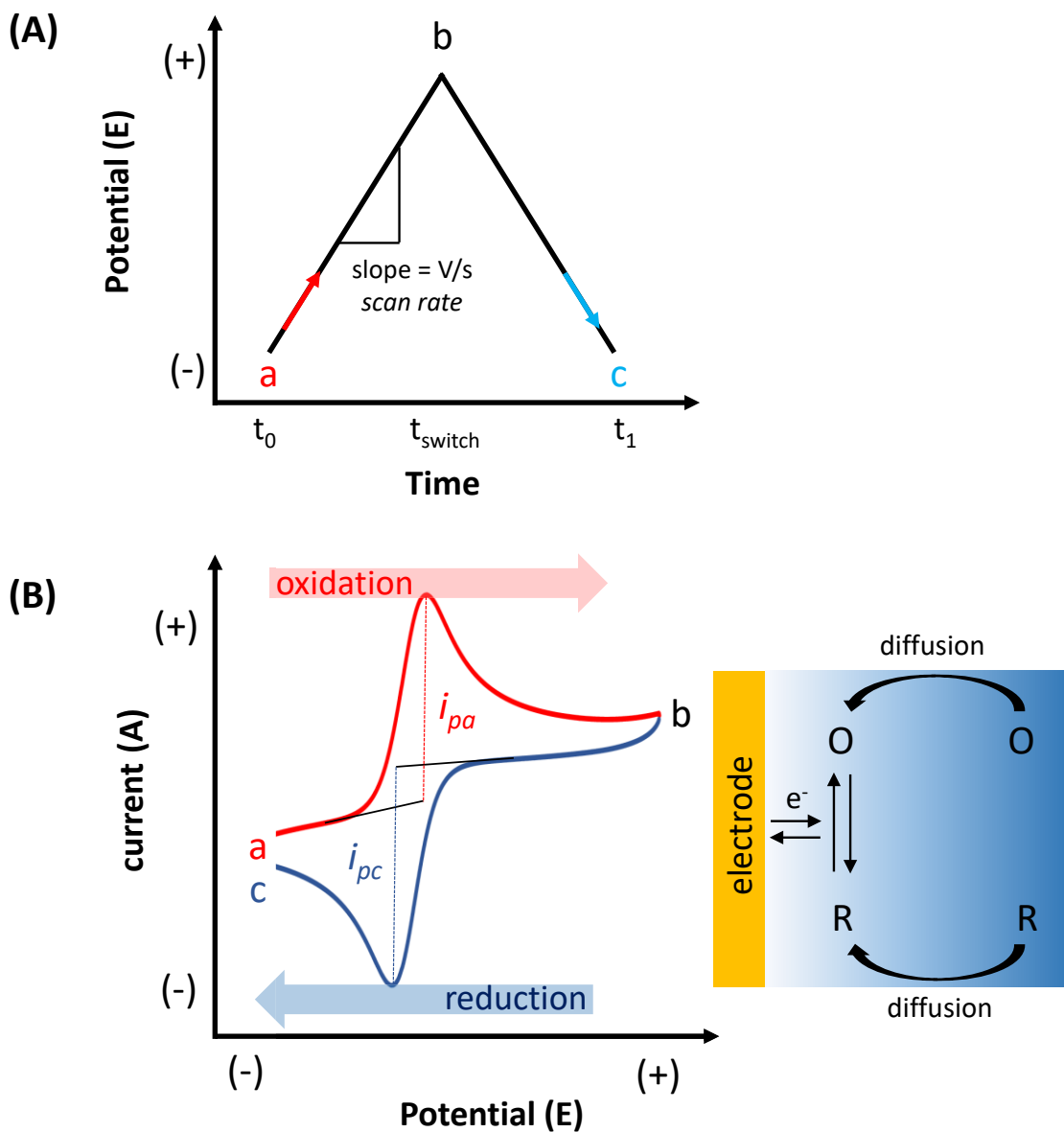


Figure 2.1 (A) Cyclic voltammetry potential waveform. (B) Representative CV response of reversible redox-active species. The inset next to (B) shows the diffusion process of redox species toward the electrode surface.

Cyclic voltammetry (CV) is one of the most popular electrochemical methods and has been extensively used for studying the redox properties of molecules either in solution or on surface. To conduct a CV measurement, a linear scan for a particular potential range is performed at a designated scan rate (v) followed by a reverse scan to the initial potential (Figure 2.1A), while the current is recorded simultaneously. As shown in Figure 2.1B, the presence of a reversible electroactive species (e.g., $\text{Fe}(\text{CN})_6^{4-}$) in the supporting electrolyte induces a pair of redox peaks. Oxidation of the species occurs as the potential sweeps positively and the reduction occurs during the reverse scan. The position of these peaks in the CV voltammogram is related to the electrode potential, which can be described by the Nernst equation:⁹⁴⁻⁹⁶

$$E = E^{0'} + \frac{RT}{nF} \ln \frac{[\text{Ox}]}{[\text{Red}]} \quad (2.1)$$

where E is the potential of an electrochemical cell, $E^{0'}$ is the formal potential, R is the gas constant ($8.314 \text{ J mol}^{-1} \text{ K}^{-1}$), T is the absolute temperature (K), n is the total number of electrons transferred in the reaction, and F is the Faraday constant (96485 C mol^{-1}). Particularly, $E^{0'}$ is dependent on the experimental conditions, which is often estimated based on the average of the two peak potentials ($E^{0'} \approx E_{1/2}$).⁹⁵ For a reversible redox reaction (providing that the electron transfer rate is rather fast), the separation between the peaks (also known as the peak-to-peak separation) is governed by the diffusion of the redox species from the bulk solution to the electrode surface;⁹⁴ the decrease in the post-peak current is due to the gradually declined concentration of the redox species near the electrode as they are being converted electrochemically.⁹⁵

As illustrated in Figure 2.1A, the slope of the linear relationship between the time and the applied potential is the scan rate (v), which affects the double layer formed at the electrode/electrolyte interface, and it influences the current for the redox reaction. For a reversible redox reaction in solution, the Randles-Ševčík equation is used to describe the effect of scan rate on the peak current (i_p):^{94,97,98}

$$i_p = 0.446nFAC^0 \left(\frac{nFvD_0}{RT} \right)^{1/2} \quad (2.2)$$

where A is the effective surface area of the working electrode, C^0 is the concentration of the redox molecule (mol/cm^3) and D_o is its diffusion coefficient (cm^2/s). Upon constructing the plot of i_p as a function of $v^{1/2}$, a linear relationship is expected for solution-diffused redox molecules (Eq. 2.2).

In contrast, for redox molecules that are adsorbed on electrode, the i_p is linearly related to the v as shown below:^{94,99}

$$i_p = vA \Gamma \frac{n^2 F^2}{4RT} \quad (2.3)$$

where, Γ is the surface density of the electrode-adsorbed species in mol cm^{-2} . Because the adsorbed species are constrained on the surface (no diffusion process involved), a symmetric pair of redox peaks are typically observed (Figure 2.2).^{58,94} A zero peak-to-peak separation is expected for a reversible redox system (as no mass transport of the redox-active species to the electrode surface from the bulk solution being involved), but it becomes vulnerable at faster scan rates or in the case of slow electron transfer kinetics.^{58,95} Furthermore, the total amount of Faradic charge (Q) transported between the redox-active species and the electrode during the redox reaction can be quantitated by integrating either the oxidation (orange shaded) or reduction peak (blue shaded) (Figure 2.2).⁹⁴

$$Q = nFA\Gamma \quad (2.4)$$

As observed from the CV responses of both solution-diffused and electrode-adsorbed redox species (Figure 2.1B and Figure 2.2), the “area” between the two baselines of redox peaks (i.e., the background current) is the capacitive current (I_c).^{58,95,100} The presence of the capacitive current is due to the accumulation of ions (unrelated to any redox reaction) on the electrode surface when the applied potential changes, making the electrode-solution interface a capacitor.¹⁰⁰

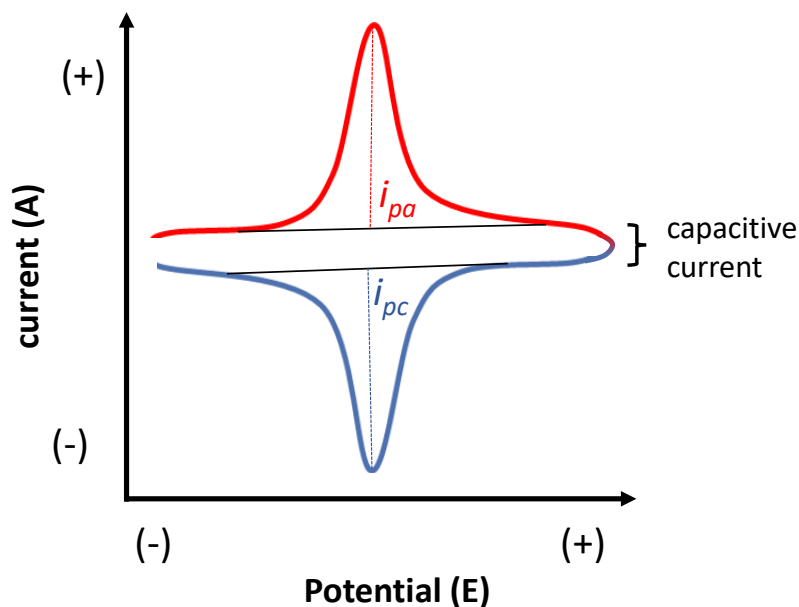


Figure 2.2 Representative CV response of a reversible electrode-adsorbed redox-active species.

Generally, electrochemical measurements are carried out in a three-electrochemical cell that can hold a desired volume of electrolyte, a working electrode (WE), reference electrode (RE), and a counter electrode (CE).⁹⁵ A schematic representation of this basic setup is shown in Figure 2.3. Depending on the potential applied to the system, either oxidation or reduction of a redox-active analyte of interest occurs on the WE. The CE or auxiliary electrode is added to complete the circuit so that the electric current can flow through the system. The RE is designed with stable composition of known electrode potential, which acts as a reference to control and measure the potential applied to the working electrode. To meet the requirements for different analyses, there are a wide variety of electrodes to choose from. The choice of WE is important as it provides different potential windows or promote/reduce the adsorption of species. Popular WEs are platinum, gold, glassy carbon, and liquid mercury. We should be cautious when using liquid mercury electrode as it is toxic to human health and problematic for the environment.⁹⁵ For RE, if the electrochemical measurements are done in a aqueous media, either AgCl/Ag electrode, standard hydrogen electrode, or saturated calomel electrode can be used;

whereas RE based on the Ag^+/Ag couple are commonly employed in organic media. In the mean time, a platinum wire or disk is typically used as the CE.⁹⁵

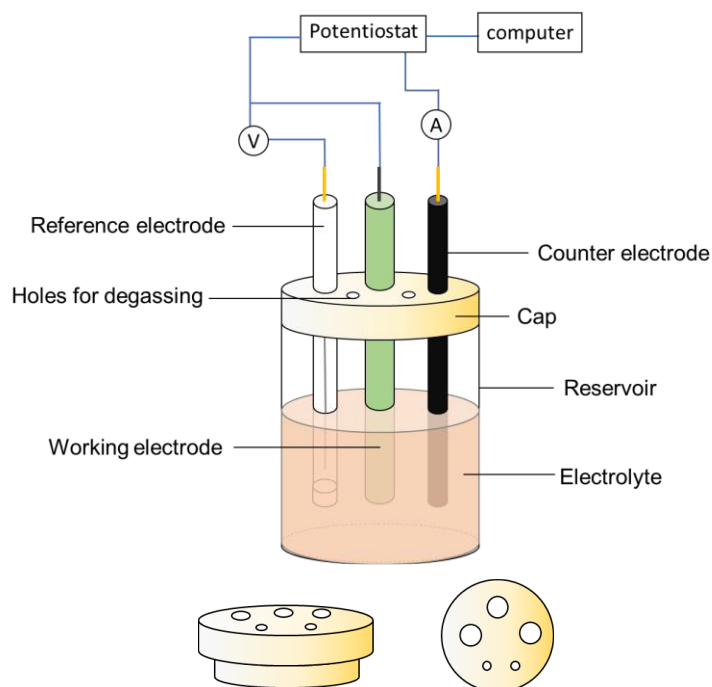


Figure 2.3 Schematic representation of a three-electrode electrochemical cell for CV measurements of solution diffused redox molecules. During measurements, the three electrodes (working, reference, and counter electrodes) are submerged in the same electrolyte solution. The additional two holes on the cap is for degassing the solution with a N_2 or Ar line.

In order to perform electrochemical measurements on redox-active molecules adsorbed on chip-type electrodes, the electrochemical cell needs to be specially designed. Figure 2.4 shows the configuration of such a cell, which was patented by Ge and Yu, and manufactured at the SFU mechanical shop.¹⁰¹ Unlike the conventional electrochemical cell (requires few mL solutions), only 800 μL of electrolyte is required for the measurements. This allows us to work with rather expensive samples, such as modified DNA strands. More importantly, it allows the use of gold slides (glass slides coated with a thin gold film) to be used as the working electrode, which is popular for immobilizing thiols.

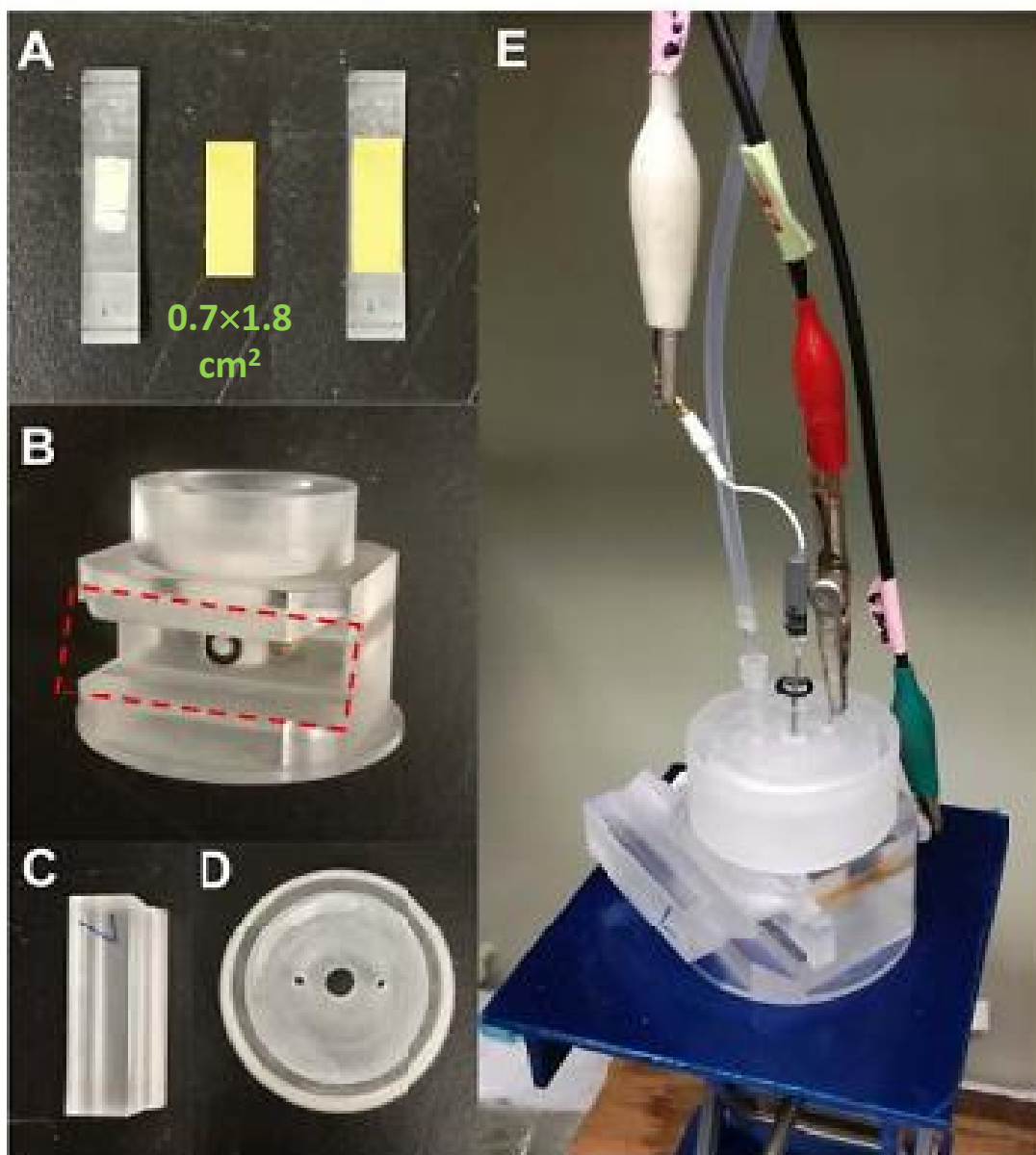


Figure 2.4 Schematic view of the single-chamber electrochemical cell made of Plexiglas V-grade acrylic resin. **A:** plate for mounting a working electrode (i.e., a gold slide with a dimension of $0.7 \times 1.8 \text{ cm}^2$). **B:** main body of the cell with a top-opening for adding electrolyte solutions, and a side slot (indicated by the red dashed rectangle) for attaching the working electrode. The opening with an O-ring seal located in the middle of the slot defines the area of working electrode exposed to the electrolyte in the cell. **C:** holder to lock the working electrode-mounting plate inside the slot. **D:** cap with three holes for inserting an reference electrode, a counter electrode, and an inert gas line. **E:** photo of the assembled cell that is ready for performing measurements.

Note: Adapted with permission from Ref 101. Copyright (2018), *American Chemical Society*. The fabrication of the electrochemical cell has been patented: Ge, B.; H.-Z. Yu. An electrochemical cell designed for sheet-shaped working electrode. CN210720234U, 2020.

2.2. Fourier-Transform Infrared Spectroscopy (FTIR)

Infrared (IR) spectroscopy is developed to characterize compound structure and composition as a vibrational spectroscopic technique.¹⁰² The measurements are performed within the IR region of the electromagnetic spectrum (10 - 15000 cm^{-1}), which can be further divided into three sub-regions: far-IR (FIR, 10 - 400 cm^{-1}), mid-IR (MIR, 400 - 4000 cm^{-1}), and near-IR (NIR, 4000 - 15000 cm^{-1}).¹⁰³ Because the associated energy within the IR region is smaller compared to the UV and visible radiations, it is only capable of inducing changes between vibrational and rotational states of molecular species being analyzed.¹⁰⁴ A net change in dipole moment during molecular vibration or rotation upon absorbing IR radiation is a must in order to be IR active. All the rotational and vibrational energy levels are quantized that a matched IR radiation frequency can interact with an electric field induced by the molecular activities.¹⁰⁴ However, for solid and liquid samples, rotations are rarely observed; therefore, broadened vibrational bands are often found for these samples. Vibrations can be separated into two motions: one is stretching (symmetrical and asymmetrical) and the other is bending (scissoring, rocking, wagging, and twisting), affecting either the bond length or the bond angle.¹⁰³ The molecular geometry defines the vibration modes and for that there are $3N-5$ for linear molecules and are $3N-6$ for non-linear molecules, where N is the number of atoms in a molecule.¹⁰⁵ The spectra can be collected either in transmittance (T) or absorbance ($A = -\log T$) mode, with respect to the wavenumber ($\tilde{\nu} = 1/\lambda$).

Generally, a FTIR spectrometer consists of: (1) an IR source, (2) an interferometer system, (3) a sample compartment, and (4) a detector.¹⁰² The interferometer is the core component in FTIR that it is used to modulate wavelength from a broadband IR source. As shown in Figure 2.5, upon striking on the beam splitter, half of the incident light beam reflects off the surface and reach a stationary mirror whereas the other half transmits through to reach a linearly movable mirror that can be held at equally spaced points.¹⁰⁶ Once the two half beams reach the mirrors, they reflect off and recombine at the beam splitter either constructively or destructively before passing through the sample in the sample compartment. This is achieved by the displacement of the movable mirror such that

the overall distance ($2 \times d_{OB}$) travelling by the beam results in a wave that is either in phase (constructive interference) or out of phase (destructive interference) in reference to the other beam when combining. The difference in pathlength (δ) between d_{OA} and d_{OB} is given by:

$$\delta = 2 \times (d_{OB} - d_{OA}) \quad (2.7)$$

An interferogram is generated based on the output light intensities against δ , which can be translated into the actual spectrum via Fourier transformation.^{102,105}

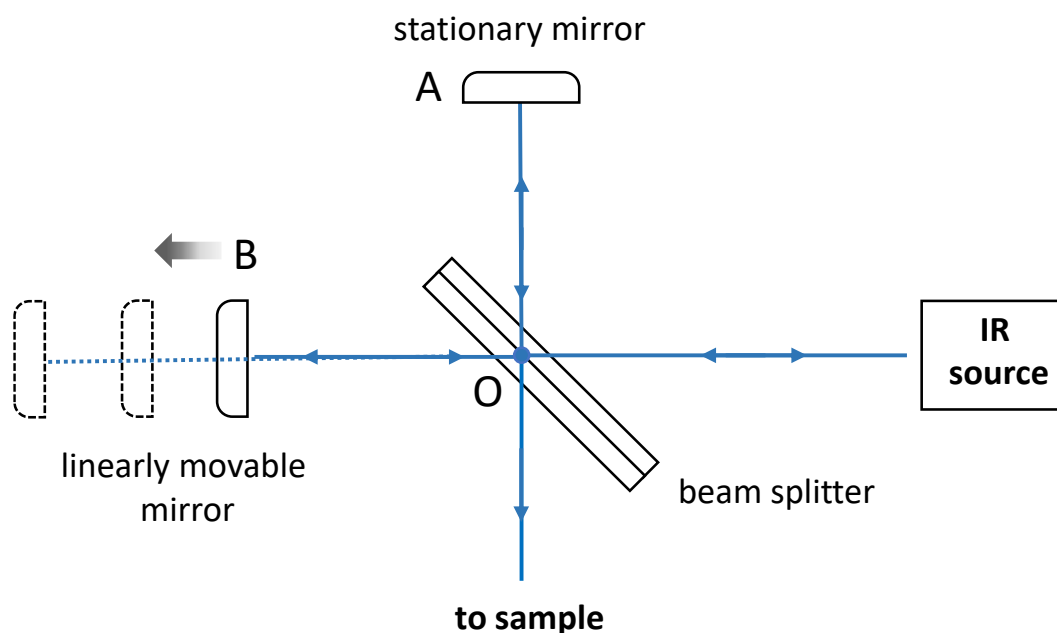


Figure 2.5 Schematic optical diagram of an interferometer in FTIR. The two mirrors are positioned perpendicular to one another.

Specular (shiny) reflection-adsorption IR spectroscopy which operating at a grazing angle analysis is specifically designed for characterizing thin film on a metal substrate by “exposing” the sample to p-polarized light.¹⁰² Therefore, the component dipoles perpendicular to the strongly reflecting surface are excited.¹⁰⁷ When employing the p-polarized light, it enhances the sensitivity due to the polarization effect on a reflective surface to the greatest when the incident angle (θ) is above 80° to the surface normal. This intensification is achieved because upon striking the metal surface at large incident angles,

it induces a phase shift of approximately 90° , which results in a combination of the incident and reflected beam to a standing wave, that is largely p-polarized.^{108–110} The desired incident angle is attained by employing two tilt mirrors as shown in Figure 2.6.¹⁰⁸

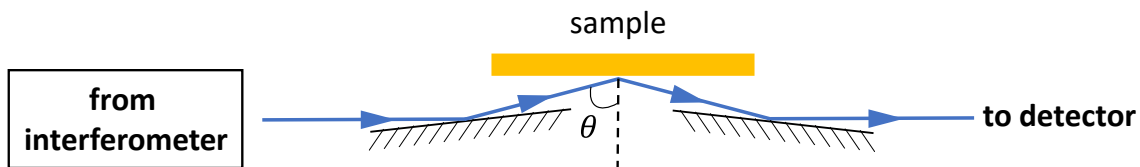


Figure 2.6 Schematic diagram showing angle of incident with the sample by employing two tilt mirrors.

These characteristics make reflection-absorption FTIR an useful tool in assessing monolayer formation and surface reaction taking place on a reflective surface; indeed, FTIR has been used widely in characterizing SAM on gold surfaces.^{37,48,90,111} As shown in Figure 2.7, characteristic peaks for both single-component SAM of undecanethiol (Figure 2.7b) and ferrocenylundecanethiol (Figure 2.7e), and their binary SAMs (Figure 2.7c & d) can be identified based on the symmetrical and asymmetrical vibrational modes of methylene group ($-\text{CH}_2-$), terminal methyl group ($-\text{CH}_3$), and $-\text{CH}$ group from the Cp ring of Fc terminal group. By comparing these peak positions from each individual FTIR spectrum to a reference sample of octadecanethiol SAM (Figure 2.7a), the level of structural organization/molecular ordering of these SAMs can be assessed based on similar peak positions.⁶⁷

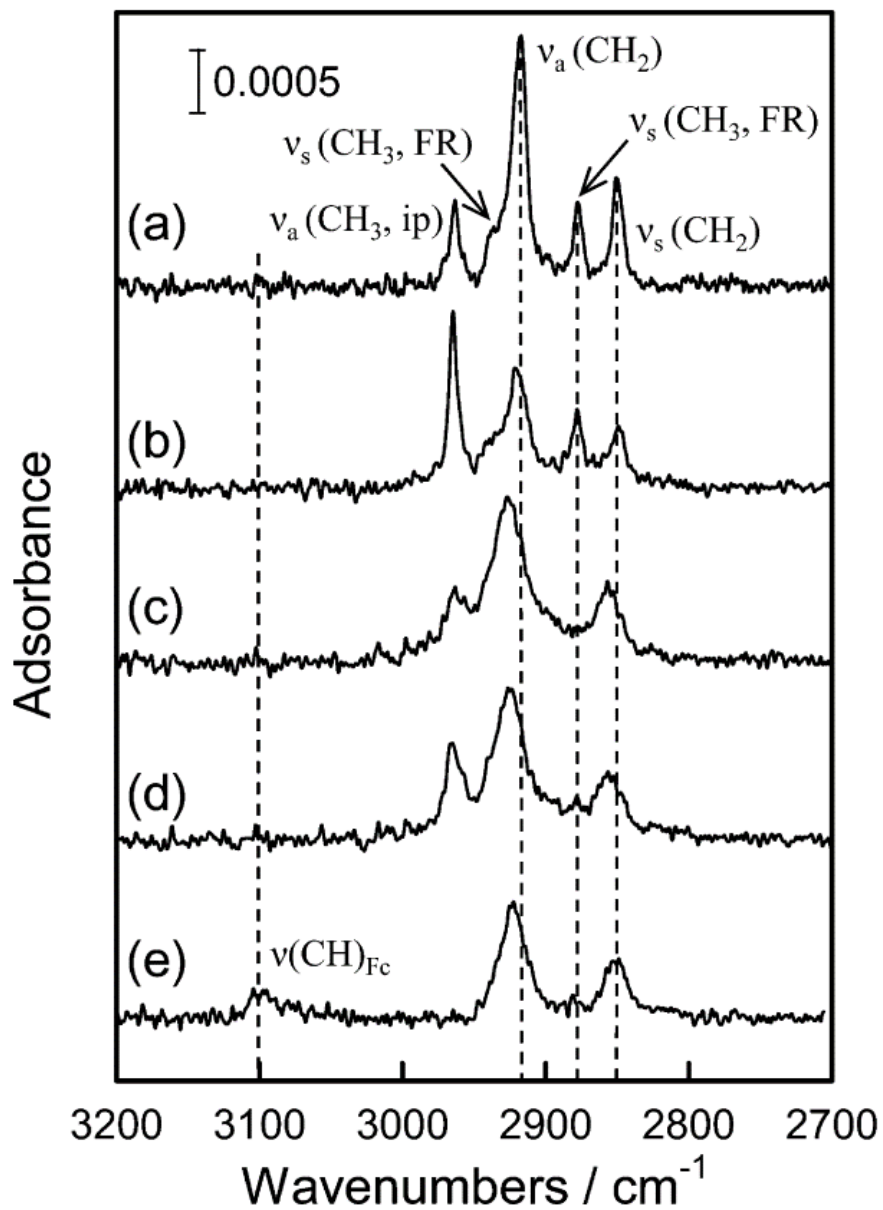


Figure 2.7 FTIR spectra of (a) octadecanethiol SAM on gold (C18S-Au), (b) undecanethiol SAM on gold (C11S-Au), (c) ferrocenylundecanethiol/undecaethiol SAMs on gold (FcC11S-/C11S-Au) prepared by the postassembly exchange method, (d) FcC11S-/C11S-Au prepared by coadsorption method, and (e) FcC11S-Au.

Note: (A) Reprinted with permissions from Ref 67. Copyright (2014), *American Chemical Society*.

2.3. Water Contact Angle Measurement

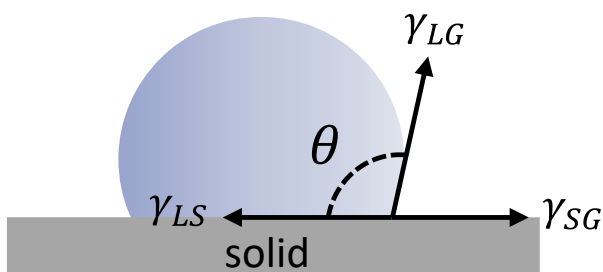


Figure 2.8 Schematic of a water drop on a solid surface showing contact angle (θ) that is determined by a balance of the interfacial tensions of solid-gas (γ_{SG}) and solid-liquid (γ_{SL}), and the horizontal projection of the liquid-gas (γ_{LG}) on the solid surface ($\gamma_{LG} \cos \theta$).

To define the wettability of a solid surface, water contact angle measurements come into place. The contact angle is defined by the thermodynamic equilibrium established between three interfacial tensions: liquid-gas (γ_{LG}), liquid-solid (γ_{LS}), and solid-gas (γ_{SG}) at interfaces where they meet (Figure 2.8). As described by the Young's equation, the relationship between the water contact angle (θ) and the three interfacial tensions is:¹¹²

$$\cos \theta = \frac{\gamma_{SG} - \gamma_{SL}}{\gamma_{LG}} \quad (2.8)$$

The common accepted definitions of surface wettability are: 1) a surface is hydrophilic (high in surface energy) when $10^\circ < \theta < 90^\circ$; 2) hydrophobic when $90^\circ < \theta < 150^\circ$; and 3) superhydrophobic when $150^\circ < \theta < 180^\circ$.¹¹³ In fact, the use of water contact angle on characterizing self-assembled monolayers (SAM) has been extensive.^{37,90,111,114} The variation in the measured θ is mainly due to the terminal groups of the SAMs, which is in direct contact with the water droplets; therefore, it provides insight into the packing density and heterogeneity of the SAMs prepared.

Shown in Figure 2.9 is a schematic diagram of an optical goniometer that are used for measuring water contact angles. A modern device typically consists of a high-resolution camera for capturing the amplified image of the liquid drop, a horizontal light source, and a sample stage. In addition, a microliter syringe/pipette is needed for delivering a desired amount of liquid ($1 \sim 2 \mu\text{L}$).

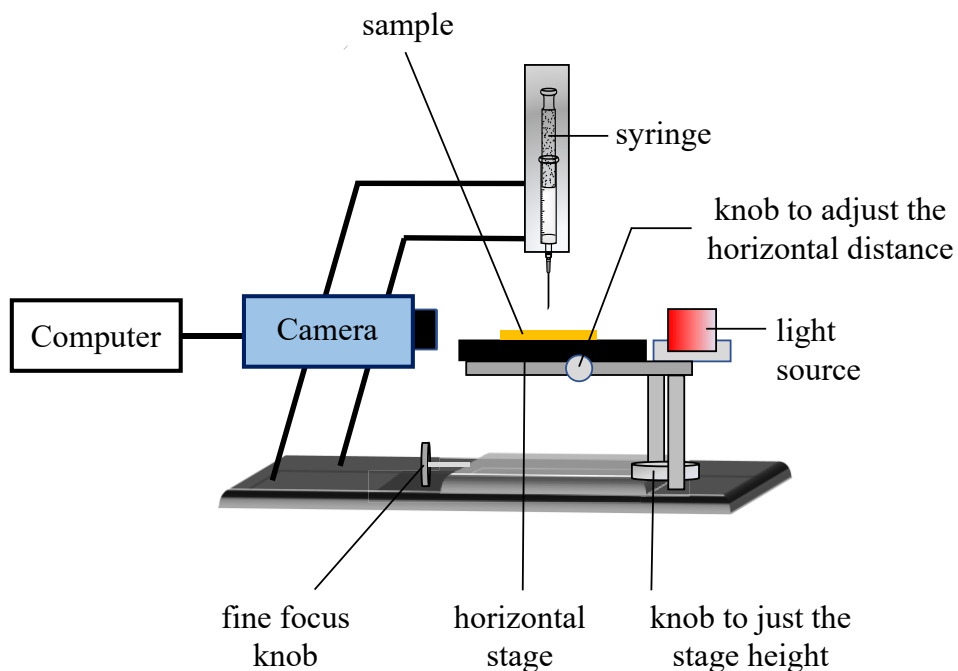


Figure 2.9 Schematic diagram of contact angle measurement setup with the sessile drop method drawn based on the AST VCA system goniometer.

2.4. X-Ray Photoelectron Spectroscopy (XPS)

The X-ray photoelectron spectroscopy (XPS) uses monochromatic X-ray to irradiate a sample of interest for probing the outer surface chemical composition (within the first 10 nm).¹¹⁵ Typically, an XPS instrument consists of (1) an X-ray source which are generally equipped with Mg or Al targets because of the narrow bandwidths (K_{α} : 0.8 – 0.9 eV) and suitable filters for enhanced resolution; (2) a series of chambers that allows samples to be loaded at atmospheric pressure but analyzed under vacuum; (3) an electron energy analyzer

for spreading the emitted electrons based on their kinetic energy; (4) a detector, and (5) a data analysis system (Figure 2.10).¹⁰⁴ The analysis on electron energies is carried out in a concentric charged hemispherical analyzer such that electrons are “bent” to trajectories when entering the analyzer and positioned on the detector at the opposite end; therefore, their radii of curvature of projectile depends on their kinetic energies.¹¹⁶

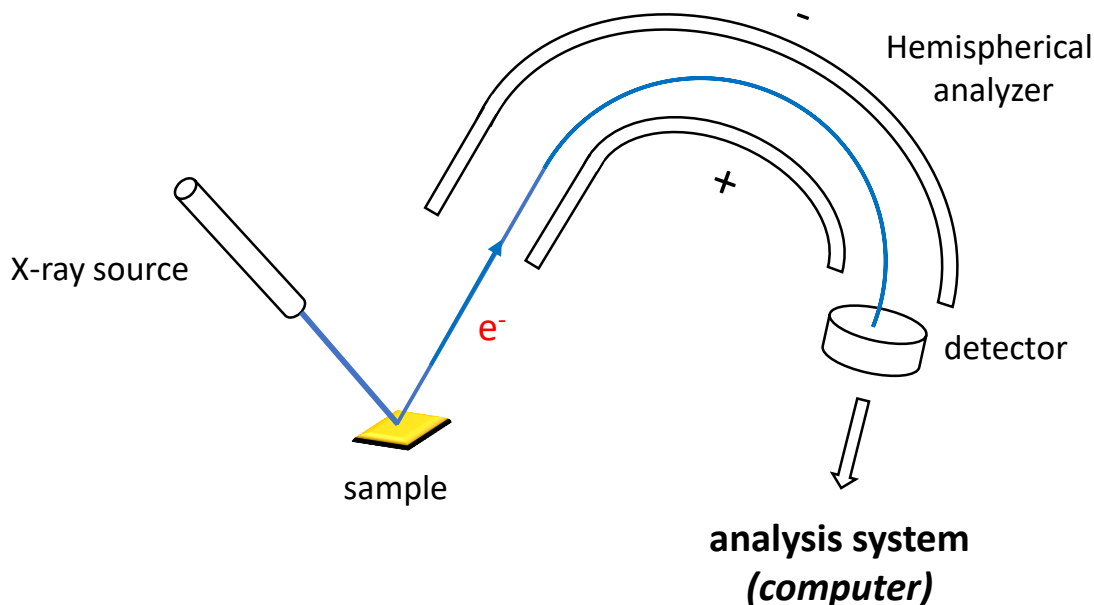


Figure 2.10 Basic components of an XPS instrument using a hemispherical field analyzer.

The XPS works based on the photoelectric effect that only the incoming X-ray beam with energy exceeds the threshold frequency (ν) can displace an electron from the core orbital (Figure 2.11). The binding energy (E_b) of the electron can be calculated as below:¹⁰⁴

$$E_b = E_{h\nu} - E_k - w \quad (2.9)$$

where $E_{h\nu}$ is the energy of the incoming X-ray photon, E_k is the kinetic energy of the electron measured by the instrument detector, and w is the work function of the spectrometer. By plotting a graph of emitted electron population against the measured E_b based on the recorded kinetic energy (E_k), a survey spectrum can be acquired for qualitative

identifying the elemental composition of the sample surface over a wide binding range. Furthermore, a high-resolution scan can be obtained for a closer analysis on the chemical shift to reveal the oxidation states and structure of an element.

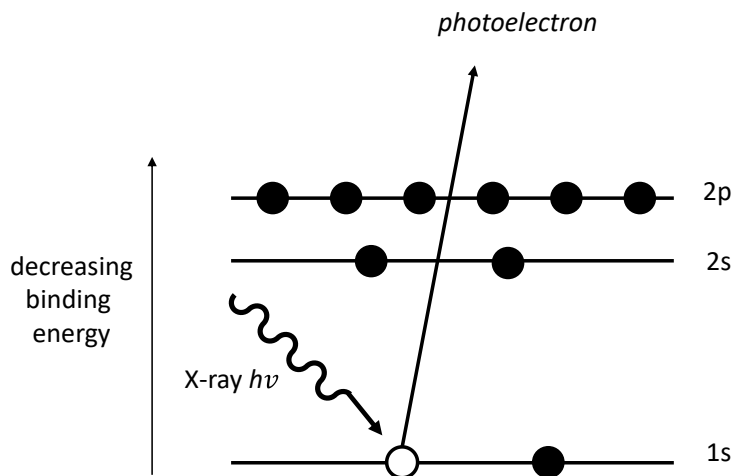


Figure 2.11 Schematic diagram of the mechanism of electron emission in XPS.

Besides the atomic composition, XPS provides information on the structure and oxidation state of the sample being examined.¹⁰⁴ For example, Figure 2.12 shows XPS spectra collected from a binary SAM prepared in deposition solutions of increasing mole fraction of 11-mercaptoundecanol with n-decanethiol on gold (HOC11S/C10S-Au) in the O 1s and C 1s regions.¹¹⁷ The composition of a binary SAMs can be controlled by varying the composition of the deposition solution. As shown in Figure 2.12A, reducing the amount of HOC11SH results in a gradual decreasing O 1s peak. As shown in Figure 2.12B, the shoulder peak appeared at 286.6 eV is for the carbon that is bound to the hydroxyl. Because of the electron withdrawing ability of O, the C 1s electron experiences a higher effective nuclear charge compared to the methyl group; therefore, the observed binding energy becomes slightly higher.

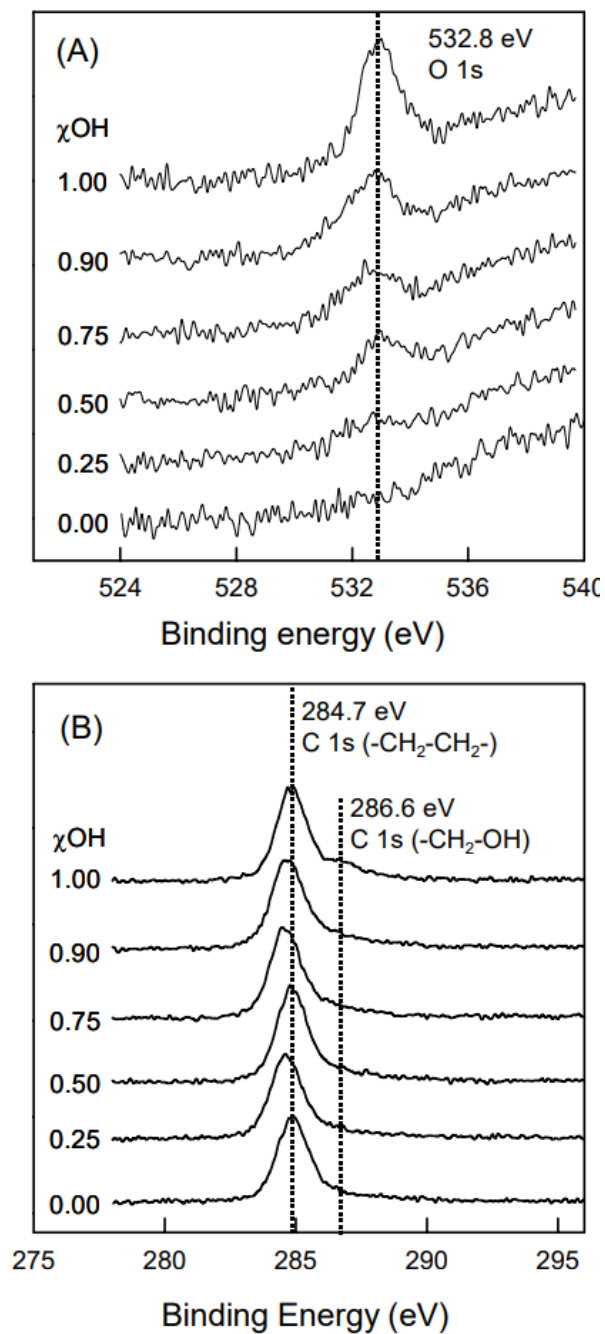


Figure 2.12 XPS characterization of gold slides modified in binary deposition solutions that contain different mole fraction of HOC11SH and C10SH. (A) O 1s region and (B) C 1s region.

Note: Reprint with permission from Ref 117. Copyright (2004). Wiley-VCH Verlag GmbH & Co. KGaA, Weinheim.

Chapter 3.

Experimental Details

In this chapter, I will detail the experimental procedures on the chemical attachment of $\equiv\text{-O-CB}[7]$ onto azide-terminated SAMs, including the surface optimization and the determination of reaction efficiency. The surface characterizations are also described. Furthermore, procedures on carrying out the thermodynamic and kinetics studies between selective Fc derivatives of different structural features with the surface-immobilized CB[7] are described.

Note: This chapter is adapted with permission from:

Chen, K. S.; Qi, L.; Chen, J.; Wang, R.; Yu, H.-Z. “Click” cucurbit[7]uril hosts on self-assembled monolayers: quantitative supramolecular complexation with ferrocene guests. *J. Phys. Chem. C.* **2022**, *126*, 1661-1671. Copyright (2022), *American Chemical Society*.¹¹⁸

3.1. Reagents and Materials

11-azido-1-undecanethiol (N₃C₁₁SH, >95%) was purchased from ProChimia Surfaces Sp. z. o.o. (Gdynia, Poland); 1-decanethiol (C₁₀SH, 99%), ferrocenemethanol (FcMeOH, 97%), tris(3-hydroxypropyltriazolylmethyl)amine (THPTA, 95%), copper(II) sulfate pentahydrate (CuSO₄·5H₂O, ≥98.0%), L-ascorbic acid (AA, 99%), bromoethane (EtBr, 98%), (dimethylaminomethyl)ferrocene (FcN, ≥ 95%), aminoferrocene (FcNH₂, ≥98.0%), tris(hydroxymethyl)aminomethane (Tris, ≥ 99.8%), ferrocenecarboxylic acid (FcCOOH, 97%), and ferroceneacetic acid (FcAcCOOH, 98%) tris(hydroxymethyl)aminomethane (Tris, ≥ 99.8%) were purchased from Sigma-Aldrich (St. Louis, MO). Ethanol (EtOH, 95%) was from Commercial Alcohols (Toronto, Canada). Hydrogen peroxide (H₂O₂, 30%) was purchased from Avantor Performance Materials (Pennsylvania, US). Sulfuric acid TraceMetal Grade (H₂SO₄) was purchased from Fisher Scientific Company (New Hampshire, US). All chemicals were of ACS reagent grade and used as received. Gold slides (glass slide coated with 5 nm Cr and 100 nm Au) were purchased from Evaporated Metal Films (EMF) Crop. (Ithaca, NY). Ultrapure water (deionized water > 18.2 MΩ cm) used for making all aqueous solutions was produced from a Barnstead EASYpure UV/UF compact water system (Dubuque, IA).

The synthesis of the alkyne-functionalized CB[7] (≡-O-CB[7]) was performed by Dr. Jia Chen from University of Macau. In brief, the reaction was started with the preparation of monohydroxy-CB[7] (HO-CB[7]) via a photoelectrochemical method (to generate a hydroxyl radical) developed by Ouari and co-workers^{44,45} followed by reacting with propargyl bromide to produce ≡-O-taz-CB[7].¹¹⁹ The synthesis of the cationic Fc derivative, FcN⁺Br⁻ (dimethylethylferrocenylmethylammonium bromide) was also based on literature procedures by treating FcN with bromoethane for a prolonged period.^{120,121} Detailed procedures and product characterization are presented in Appendix A (A2 & A3).

3.2. Surface Modification and Host Guest Complexation (Fc@CB[7])

To properly fit the specially designed electrochemical cell (Figure 2.4), gold slides need to be cut to a dimension of $0.7 \times 1.8 \text{ cm}^2$. These pre-cut slides were cleaned with Piranha solution (3:1 v/v mixture of concentrated H_2SO_4 and 30% H_2O_2) at $90 \text{ }^\circ\text{C}$ for 10 min (Caution: *Piranha solution reacts violently with organics; it must be handled with extreme care*) followed by rinsing with copious amounts of deionized distilled water prior to any surface modification or analysis. Preparation of a binary N3C11S-/C10S-self-assembled monolayer on gold slide (N3C11S-/C10S-Au) follows the conventional co-adsorption method described in the literatures.^{67,122} These monolayers were formed by immersing Piranha-cleaned gold slides in individual deoxygenated 95% ethanolic deposition solutions that contains different mole fractions of N3C11SH and C10SH ($\chi_{sol}^{N3} = 0, 25, 50, 75, \text{ and } 100\%$) for 24 h. The total concentration of the two thiol molecules were kept at 1 mM. Then, the modified gold slides were removed from the deposition solution and were rinsed with excess amount of 95% EtOH and deionized water thoroughly and dried under a stream of N_2 gas.

To access the practicality of attaching the $\equiv\text{-O-CB[7]}$ on the gold surface via CuAAC, a reaction mixture of $250 \text{ }\mu\text{M}$ $\equiv\text{-O-CB[7]}$, $100 \text{ }\mu\text{M}$ Cu^{2+} , 2.5 mM AA, and $500 \text{ }\mu\text{M}$ THPTA were deposited on the N3C11S-Au ($\chi_{sol}^{N3} = 100\%$). After the reaction had been proceeded for 4 h, the CB[7]-modified gold surface (CB[7]-O-taz-C11S-Au) was rinsed with excess amount of deionized water and was incubated in $50 \text{ }\mu\text{M}$ FcMeOH for 1 h. The exact same procedure was carried out when looking for the optimal χ_{sol}^{N3} for attaching the greatest number of $\equiv\text{-O-CB[7]}$ onto the SAMs. And to determine the efficiency of attaching $\equiv\text{-O-CB[7]}$ via CuAAC onto the N3C11S-/C10S-Au ($\chi_{sol}^{N3} = 75\%$), the reaction was quenched by washing the reacted surface with excess amount of deionized water at different time followed by immersion in $50 \text{ }\mu\text{M}$ FcMeOH for 1 h.

The comparative study on the host-guest complexation of surface-immobilized CB[7] toward selected Fc derivatives (FcMeOH, FcNH₂, FcN⁺Br⁻, FcCOO⁻, and

FcAcCOO⁻) was carried out by treating CB[7]-O-taz-C11S-/C10S-Au ($\chi_{sol}^{N3} = 75\%$) with varied concentrations of each Fc derivative in 10 mM Tris-HClO₄ (pH 7.4) buffer. The binding kinetics of FcMeOH toward the surface-immobilized CB[7] was examined based on the time-dependence cyclic voltammetry (CV) study in 100 nM FcMeOH. The dissociation kinetics was monitored by placing the saturated FcMeOH@CB[7]-O-taz-C11S-/C10S-Au in 10.0 mM Tris-HClO₄ buffer that was free of FcMeOH.

3.3. Surface characterizations

The CV measurements were carried out with a CHI 1040A electrochemical analyzer (Austin, TX) as potentiostat and a Faraday cage at room temperature. To ensure the accuracy and reproducibility of the experimental data, all measurements were taken under the protection on N₂ gas in deoxygenated electrolyte solutions. The three-electrode chemical cell used is shown in Figure 2.4 shown in Section 2.1. The area of the working electrode (gold slide) was defined by an O-ring seal located to the side of the electrochemical cell. The effective area ($A = 0.15 \pm 0.01 \text{ cm}^2$) was estimated based on Eq. (2.2) by measuring CVs in 1.0 mM K₃Fe(CN)₆ prepared in 0.1 M KCl at different scan rates. The counter and reference electrodes were platinum and Ag|AgCl|1M KCl, respectively.

The reflection absorption FTIR spectra were collected with a Nicolet Magna 560 Fourier transform infrared spectrometer (Madison, WI) that can focus the p-polarized IR laser at an angle (θ) of 80° on the gold samples. The interferometer is equipped with a KBr beam splitter. A liquid-nitrogen cooled mercury cadmium telluride (MCT) detector was used to record the spectra. All the FTIR spectra was recorded as absorbance *vs.* wavenumber (cm⁻¹) against a background scan performed on a Piranha-cleaned bare gold surface.

All the wettability measurements on the gold surface between modifications were accessed with a goniometer (AST VCA system, Billerica, MA) with the sessile drop method by depositing 1.5 μl of Ultrapure water on the tested surfaces.

The XPS data were obtained with the help of Dr. Michael Wang from the 4D Labs using an Axis Ultra surface analysis spectrometer (Kratos Analytical Ltd., Manchester, UK) equipped with a monochromatized Al K_{α} radiation source (150 W at 1486.6 eV).

Chapter 4.

Results and Discussion

In this chapter, I will detail the results obtained in studying the chemical attachment of $\equiv\text{-O-CB}[7]$ onto azide-terminated SAMs, including the surface optimization and the determination of reaction efficiency. After that, the interfacial formation constants of selective Fc derivatives with distinct structural features toward the surface-immobilized CB[7] were systematically evaluated. Results on the kinetics studies on the association and dissociation process between FcMeOH and the surface-immobilized CB[7] are also discussed.

Note: This chapter is adapted with permission from:

Chen, K. S.; Qi, L.; Chen, J.; Wang, R.; Yu, H.-Z. “Click” cucurbit[7]uril hosts on self-assembled monolayers: quantitative supramolecular complexation with ferrocene guests. *J. Phys. Chem. C*. **2022**, *126*, 1661-1671. Copyright (2022), *American Chemical Society*.¹¹⁸

4.1. “Click” \equiv -O-CB[7] Hosts on N3C11S-Au SAM Surface

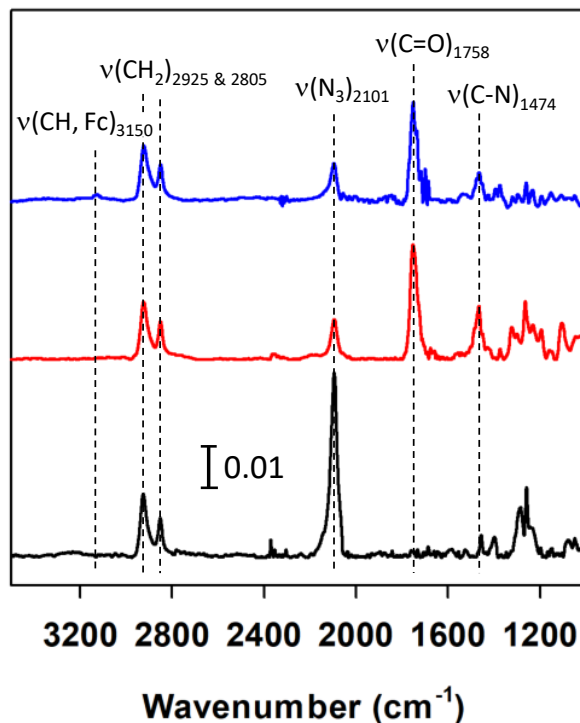


Figure 4.1 Reflection-adsorption FTIR spectra of N3C11S-Au before (black) and after the chemical attachment of \equiv -O-CB[7] via CuAAC (red), and after the incubation of CB[7]-O-taz-C11S-Au in 50 μ M FcMeOH for 1 h (blue).

Note: Reprinted with permission from Ref 118. Copyright (2022), American Chemical Society.

To start with, I have used a single-component 11-azido-1-undecanethiolate SAM on gold (N3C11S-Au) to evaluate the feasibility of the covalent attachment of \equiv -O-CB[7] in the presence of Cu^{2+} and sodium ascorbate; that is, ascorbate reduces Cu^{2+} to Cu^+ , which acts as the catalyst in CuAAC. After letting the surface reaction to proceed for 4 h, the surface CuAAC was quenched with a sufficient amount of deionized water. The immobilization of \equiv -O-CB[7] on the azide-terminated SAM was first confirmed by FTIR spectroscopy (Figure 4.1). By comparing the spectra before (black curve) and after (red curve) “clicking” \equiv -O-CB[7] on N3C11S-Au, it is concluded that approximately 75% of azide group ($-\text{N}_3$) on the SAM surface participated in the CuAAC reaction as the $\nu(\text{N}_3)$ peak at 2101 cm^{-1} decreased to about 1/4 of its original height.⁹⁰ The appearance of two other strong peaks, $\nu(\text{C-N})$ peak at 1474 cm^{-1} , provides further evidence for the successful

conjugation of $\equiv\text{-O-CB}[7]$ with the N3C11S-Au surface.⁴⁸ More importantly, a new peak was observed at 3150 cm^{-1} upon treating the resultant CB[7]-O-taz-C11S-Au with FcMeOH, which is the characteristic vibration mode of the -CH group of Fc ($\nu(\text{CH})_{\text{Fc}}$).¹¹¹ The acquired FTIR results not only confirm the success of tethering $\equiv\text{-O-CB}[7]$ on azide-terminated SAM to prepared CB[7]-O-taz-C11S-Au but also show their ability of binding molecular Fc guests.

Additionally, I have investigated the surface wettability to monitor the surface CuAAC for the covalent attachment of $\equiv\text{-O-CB}[7]$ and the subsequent complexation with FcMeOH guests. As shown in Figure 4.2, a clear decrease in the water contact angle after clicking $\equiv\text{-O-CB}[7]$ was observed, which is due to the existence of more polar carbonyl portals on CB[7].²⁰ Upon treating the CB[7]-O-taz-C11S-Au in FcMeOH, a slight increase in contact angle from $26 \pm 3^\circ$ to $66 \pm 2^\circ$ was observed. Though this a lot lower than that reported for ferrocenylalkanethiolate SAMs on gold (approximately 81°),^{68,112} this observation again confirms the formation of the inclusion complex between FcMeOH and surface-immobilized CB[7], for which the rather hydrophobic Fc “cores” are not directly exposed to the solution.



Figure 4.2 Water contact angle measurements on the N3C11S-Au before (left) and after the tethering of $\equiv\text{-O-CB}[7]$ via CuAAC (middle), and upon the subsequent incubation in $50\ \mu\text{M}$ FcMeOH for 1 h. The volume of the water droplet for each measurement was kept at $1.5\ \mu\text{l}$. The standard deviations were based on 3 randomly selected spots on three independently prepared gold samples.

Note: Reprinted with permission from Ref 118. Copyright (2022), *American Chemical Society*.

The modified gold samples were also subjected for electrochemical analysis. By means of CV, the complexation of surface-immobilized CB[7] hosts and solution-diffused Fc guests was quantitatively assessed. As shown in Figure 4.3A, no distinct redox peaks were detected for either N3C11S-Au (black curve) or upon tethering CB[7] (red curve), while a slight decrease in the capacitive current is evident. Remarkably, the addition of FcMeOH induced a pair of clear-cut redox peaks at $E^\circ = +189$ mV vs. Ag|AgCl, which correspond to the oxidation and reduction of FcMeOH/Fc⁺MeOH. By collecting CVs at different scan rates (Figure 4.3B), a linear relationship between the peak current and scan rate was established and it confirms that the acquired redox responses are of adsorbed FcMeOH (Figure 4.3C); that is, FcMeOH is indeed encapsulated by the surface-immobilized CB[7] (FcMeOH@CB[7]) based on Eq. (2.3). And the corresponding surface density of FcMeOH@CB[7] (Γ_{Fc}) can be determined using Eq. (2.4), which is $(4.3 \pm 0.2) \times 10^{-11}$ mol/cm². Because such an inclusion complex forms at 1:1 ratio (i.e., Γ_{Fc} equals to that of the surface-immobilized CB[7], $\Gamma_{CB[7]}$), the $\Gamma_{CB[7]}$ value is predicted to be lower than that of a theoretical closely packed CB[7] monolayer.³⁸ This is likely attributed to the bulky size of CB[7] that the already attached CB[7] hosts would likely prevent the CuAAC from taking place in proximity.¹⁵ In fact, this hypothesis is also consistent with the IR results that indicate that only 75% of the -N₃ groups have reacted (Figure 4.1).

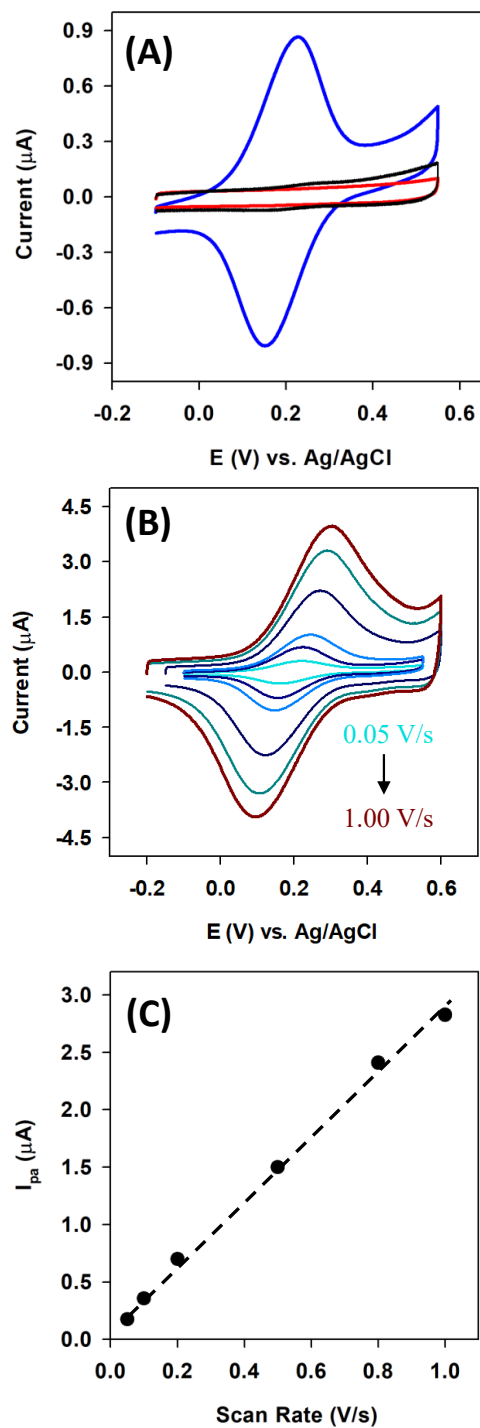


Figure 4.3 (A) Cyclic voltammetry of N3C11S-Au before (black) and after the tethering of $\equiv\text{O-CB}[7]$ via CuAAC (red), and after incubating the CB[7]-O-taz-C11S-Au in 50 μM FcMeOH for 1 h (blue). The scan rate was kept at 0.1 V/s and the electrolyte was 10 mM Tris-HClO₄ (pH 7.4). (B) Corresponding voltammograms of the same system obtained at different v . And (C) A plot for the corresponding reduction peak current (I_p) as a function of v . The dashed line is the best fit linear line to the experimental data ($R^2 = 0.99$).

Note: Reprinted with permission from Ref 118. Copyright (2022), American Chemical Society.

4.2. Optimization of the Binary SAMs and Surface “Clicking” Efficiency

With the above success, I subsequently optimized reaction conditions to maximize the amount of \equiv -O-CB[7] hosts that can be covalently attached to the SAM surface. It has been demonstrated previously that depending on the length and derivatization of diluent thiols, one can vary the distribution and coverage of desired functional groups in mixed SAMs.^{60,68} Therefore, series of binary SAMs of N3C11S-/C11S-Au were prepared from binary 95% EtOH deposition solutions containing different mole fractions of N3C11SH ($\chi_{sol}^{N_3}$) and C10SH. The goal was to have isolated, uniformly distributed N₃-terminated groups on the surface, by which minimization on the steric hindrance during CuAAC can be achieved to ensure that CB[7] hosts are immobilized at the highest coverage. Though, as discussed in Section 1.2.1. that two conventional methods can be used to prepare binary SAMs, the post-assembly exchange approach is not preferred as the passivation take places in defects, which leads to either cluster formation of -N₃ (preformed -N₃ monolayer upon exchanging with C10SH) or low surface coverage of -N₃ (preformed C10SH monolayer upon exchanging with N3C11SH). We will be examining the dependence of the exchange process and the diluent alkyl chain length, which is beyond the scope of this study.

The new appearance of the S 2p at 162.5 eV and the positive shift in Au 4f (from 83.5 to 85.3 eV) in the XPS survey scans (not included) acquired before and after the surface thiolation confirms the formation of the SAMs on Au. As shown in Figure 4.4A, upon decreasing the $\chi_{sol}^{N_3}$ in the deposition solution, the intensity of N 1s peak of the N atom either bound to the methylene (397.7 eV) or being part of the N₃-terminal group (401.6 eV) decreases dramatically; both peaks are no longer discernible at $\chi_{sol}^{N_3} = 25\%$ (Figure 4.4A). The presence of N₃-terminal groups on the surface is also confirmed with the shoulder peak at 281.9 eV for the C 1s region (Figure 4.4B), which increases with higher $\chi_{sol}^{N_3}$ in the deposition solution. Further quantitative analyses of the XPS data show that the surface coverage of N₃ groups and the solution composition is not proportional, as the N3C11SH has a lower affinity to gold in comparison with the diluent C10SH and it has tendency to form clusters at high surface densities (Figure 4.4C & D). Additionally, the

compelling decrease in water contact angle from 110° to 66° confirms the non-linear correlation between the surface and deposition solution compositions (Figure 4.5).

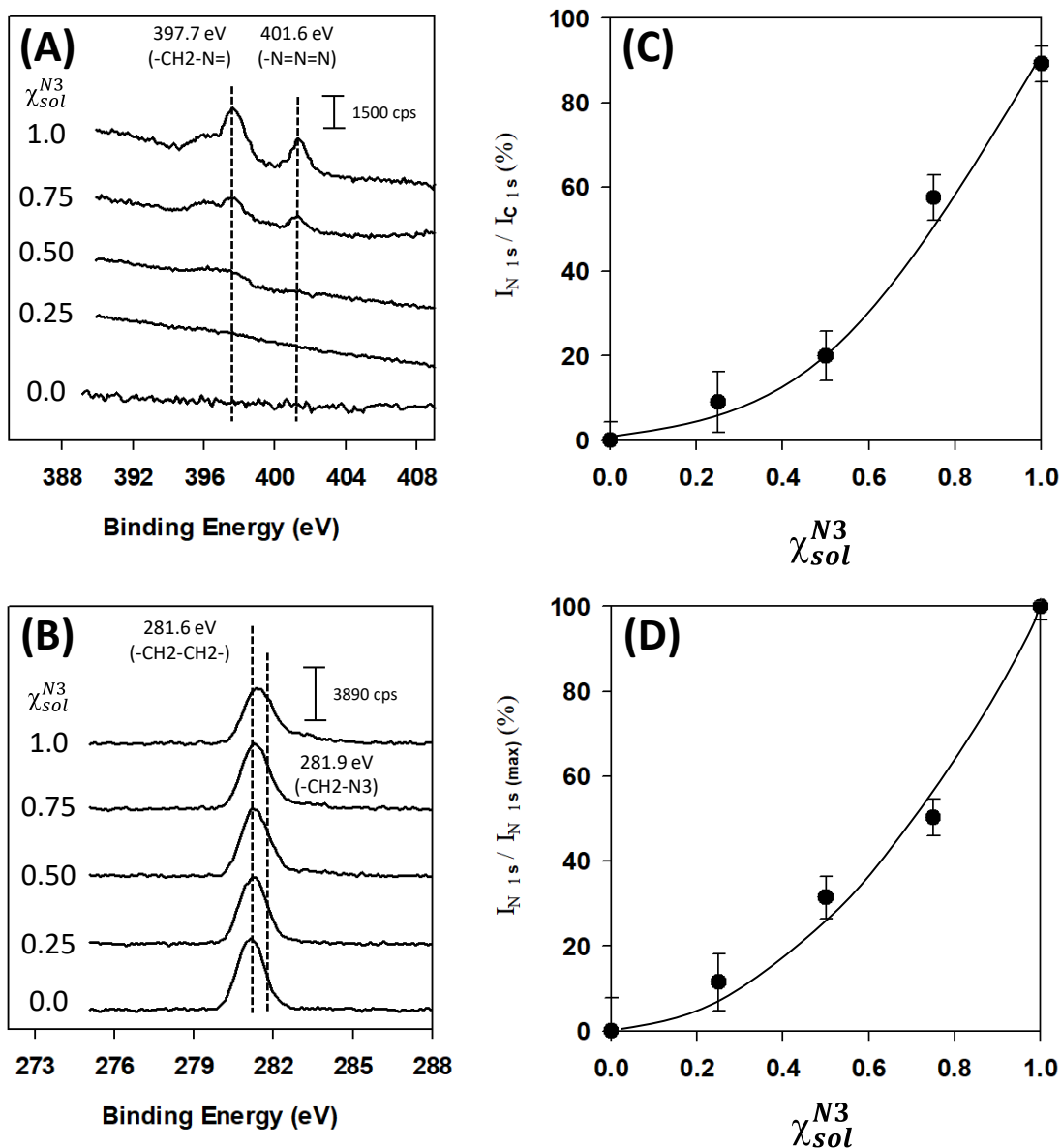


Figure 4.4 XPS spectra of (A) N 1s and (B) C 1s of gold sides modified in different 95% EtOH deposition solutions contains different mole fractions of N₃C11SH/C10SH ($\chi_{sol}^{N_3}$). (C) Relationship between the normalized intensity of N₃ ($I_{N\ 1s} / I_{C\ 1s}$) on the surface. (D) Relationship between molar fraction of N₃ on the surface and the solution position. The solid line is to guide the eye only.

Note: Reprinted with permission from Ref 118. Copyright (2022), American Chemical Society.

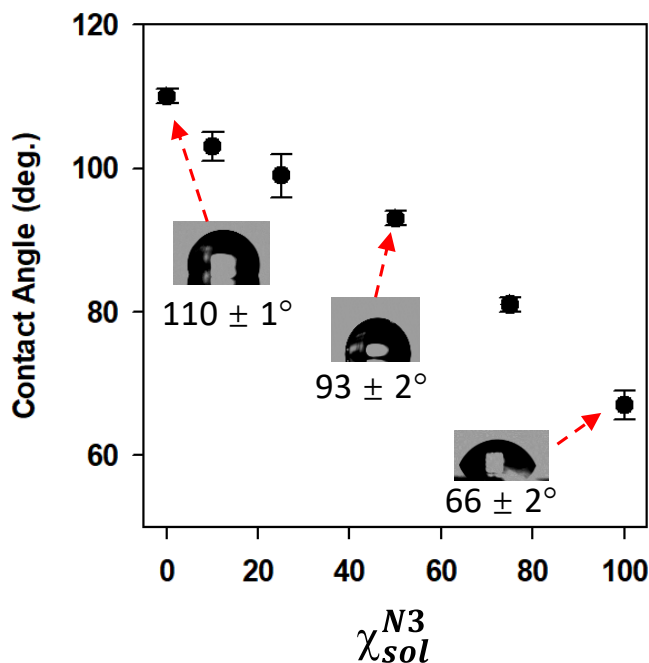


Figure 4.5 Water contact angle measurements on the modified gold plotted as a function of the N3C11SH/C10SH (χ_{sol}^{N3}) in 95% EtOH deposition solutions. The insets show the images of 1.5 μ l of deionized water droplet on the corresponding modified gold surface.

Note: Reprinted with permission from Ref 118. Copyright (2022), American Chemical Society.

As shown in Figure 4.6A, CV responses upon incubating with 50 μ M FcMeOH become much stronger initially upon increasing the χ_{sol}^{N3} in the binary deposition solution but reach the maximum at $\chi_{sol}^{N3} = 75\%$; indeed, a 15% decrease was observed in the surface density of the interfacial FcMeOH@CB[7] host-guest inclusion complexes when using pure N3C11S-Au SAM ($\chi_{sol}^{N3} = 100\%$) to immobilize CB[7] hosts (Figure 4.6B).

In fact, the $\Gamma_{CB[7]}$ ($(4.6 \pm 0.3) \times 10^{-11}$ mol/cm²) obtained from the binary SAMs prepared with $\chi_{sol}^{N3} = 75\%$ agrees with the FTIR data in Figure 4.1 (black vs. red) that a single-component N3C11S-Au is not optimal for “clicking” the greatest number of \equiv -O-CB[7] onto surface. Though the maximal $\Gamma_{CB[7]}$ obtained herein is 38% less compared to a theoretical fully packed CB[7] (calculated with the molecular diameter of 1.6 nm) on Au substrate (7.2×10^{-11} mol/cm²);³⁸ this is reasonable because intermolecular interactions between CB[7] are not considered in the calculation. Nonetheless, it is higher than that of a physical-deposition prepared CB[7] monolayer on Au (4.3×10^{-11} mol/cm²).³⁸

More importantly, due to the much weaker gold-carbonyl interactions, physisorbed CB[7] may be easily removed from the surface, confirming the importance of covalently attaching CB[7] on surfaces.

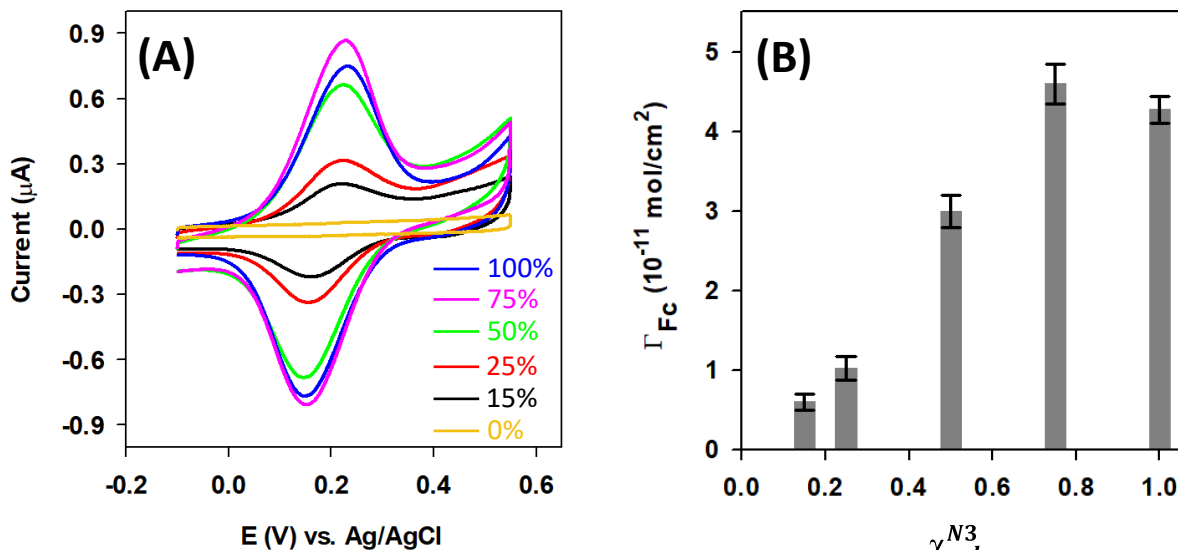


Figure 4.6 (A) Representative CV responses of N3C11S-/C10S-Au prepared from different 95% EtOH with various χ_{sol}^{N3} upon clicking $\equiv\text{-O-CB[7]}$ and incubation in 50 μM FcMeOH for 1 h. The scan rate was kept at 0.1 V/s. (B) Corresponding Γ_{Fc} determined based on the integrated charge of the oxidation peaks from (A) as a function of χ_{sol}^{N3} . The error bars represent the standard deviations based on three independently prepared samples.

Note: Reprinted with permission from Ref 118. Copyright (2022), American Chemical Society.

Upon confirming $\chi_{sol}^{N3} = 75\%$ as the optimal composition to prepare binary N3C11S-/C10S-Au, I proceeded to assess the efficiency of the CuAAC reaction for immobilizing $\equiv\text{-O-CB[7]}$ hosts. To do so, I performed the surface CuAAC in the same manner as described above but quenched the reaction by washing away the reactants at different time periods. By taking CV measurements upon the addition of FcMeOH, the determined Γ_{Fc} was used to monitor the progress of the CuAAC reaction. As shown in Figure 4.7A, the corresponding redox peaks become more pronounced as the reaction time increases. It is also evident that the Γ_{Fc} increases exponentially as a function of the CuAAC reaction time. It reaches the “plateau” within 30 min (Figure 4.7B), which is far more efficient than other reported methods.^{10,40,46} For example, the reaction of attaching hydroxylated CB[7] on N-hydroxysuccinimidyl Sepharose beads requires 48 h to complete.⁴⁰ Though the tethering of allyloxy-functionalized CB[7] on a thiol-terminated surface via

thiol-ene “click” reaction needs a much shorter reaction time (~ 3 h), it requires the use of a photoreaction chamber.⁴⁶ More importantly, the CuAAC occurs in an aqueous environment, while other reactions typically require particular organic solvents.^{40,46,123} Considering the mild condition and outstanding efficiency, it is concluded that CuAAC is an ideal approach for tethering $\equiv\text{O-CB}[7]$ hosts on azide-terminated SAMs.

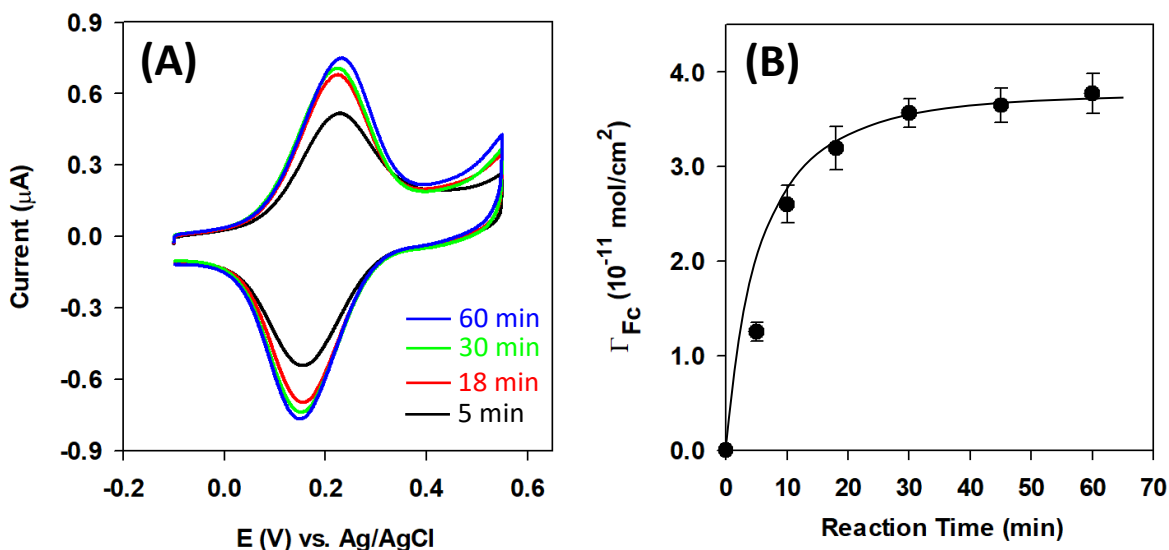


Figure 4.7 (A) Representative CV responses upon treating the N3C11S-/C10S-Au ($\chi_{sol}^{N3} = 75\%$) with $\equiv\text{O-CB}[7]$ via CuAAC for different reaction periods and followed by treatment in $50 \mu\text{M}$ FcMeOH for 1 h. The scan rate was kept at 0.1 V/s , and the electrolyte was 10.0 mM Tris- HClO_4 (pH 7.4). (B) Corresponding Γ_{Fc} determined based on the integrated charge of the oxidation peaks from (A) as a function of reaction time. The error bars represent the standard deviations based on the three independently prepared samples.

Note: Reprinted with permission from Ref 118. Copyright (2022), American Chemical Society.

4.3. Thermodynamics and Kinetics of Host-Guest Complexation on Surface

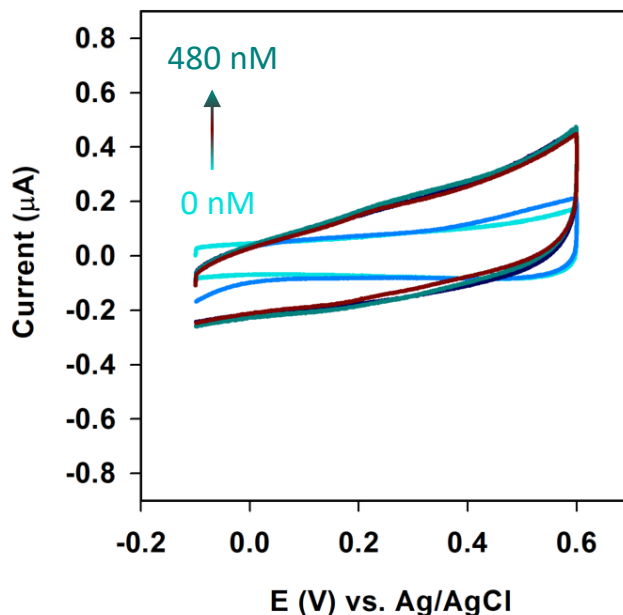


Figure 4.8 Representative CV of incubation of N3C11S-/C10S-Au ($\chi_{sol}^{N3} = 75\%$) in increasing concentrations of FcMeOH for 1 h each. The scan rate was kept at 0.1 V/s.

Note: Reprinted with permission from Ref 118. Copyright (2022), American Chemical Society.

The above promising results motivated us to investigate the binding affinity and efficiency between the surface-immobilized CB[7] hosts and FcMeOH guests in the solution. First, the non-specific adsorption of FcMeOH on the surface of N3C11S-/C10S-Au ($\chi_{sol}^{N3} = 75\%$) was examined. And it is found to be negligible since no pairs of redox peaks was detected (Figure 4.8), but the enlarged capacitive current over time suggests the accumulation of ions on SAMs over time. When incubating the CB[7]-O-taz-C11S-/C10S-Au with increasing concentrations of FcMeOH, the obtained redox peaks became much more pronounced (Figure 4.9A). Meanwhile, the corresponding Γ_{Fc} increased monotonically and began to plateau when the concentration of FcMeOH was beyond 0.4 μM (Figure 4.9B). This assures the accurate determination of both thermodynamic and kinetic parameters of the Fc@CB[7] complexation on the surface (vide infra). With the equilibrated $\Gamma_{Fc(eq)}$ at each concentration, the formation constant (K_f) can be determined based on the following equations:



$$K_f = \frac{\Gamma_{\text{Fc}(eq)}}{[\text{FcMeOH}]_{(eq)} \times \Gamma_{(\text{CB}[7])_{(eq)}}} \quad (4.2)$$

$$\Gamma_{\text{CB}[7](eq)} = \Gamma_{\text{Fc}(max)} - \Gamma_{\text{Fc}(eq)} \quad (4.3)$$

where, $\Gamma_{\text{Fc}(eq)}$ can be directly determined from the integrated charge of the oxidation peak of the FcMeOH@CB[7] host-guest inclusion complex, for which a prolonged incubation (4 h) ensures that the equilibrium is reached. To calculate the K_f value, two assumptions have been made: (1) all surface immobilized CB[7] hosts are available for complexation with FcMeOH guests such that the surface density of the unoccupied CB[7] ($\Gamma_{\text{CB}[7](eq)}$) can be determined using Eq. (4.3); (2) $[\text{FcMeOH}]_{(eq)}$ is approximated as the initial $[\text{FcMeOH}]$ because the amount of FcMeOH in the solution ($\geq 3 \times 10^{15}$ molecules) is in great excess compared with that of CB[7] hosts on the surface ($\cong 2.6 \times 10^{13}$ molecules). In this way, determination on K_f values at different FcMeOH concentrations can be carried out; as shown in Figure 4.9C, they are consistent within experimental uncertainties with an average of $(1.6 \pm 0.3) \times 10^7 \text{ M}^{-1}$. It is possible to extract the K_f values based on the Langmuir adsorption isotherm, as well; however, it would involve additional assumptions for determining the surface concentrations of complexes and free hosts (i.e., surface immobilized CB[7] with no FcMeOH accommodated).⁶⁶ Though it is still smaller than that determined in the solution (10^9 M^{-1}),³² such a high binding affinity indeed exceeds other widely used inclusion complexes, for example, Fc@cyclodextrin pairs, whose K_f values rarely achieve 10^4 M^{-1} in solution.¹²⁴ Furthermore, it shows remarkable improvement in the stability of the Fc@CB[7] complex on the surface compared to the previous system (nearly over 3 orders of magnitude), in which Fc guests are immobilized on the surface ($< 10^5 \text{ M}^{-1}$, described in Section 1.1.4).³⁷ It is likely attributed to the less restriction on the rotational freedom of FcMeOH guests in the present system; for example, solution-diffused FcMeOH guests have the “freedom” to adopt energetically favorable orientations to fit the CB[7] “cage.”²⁰

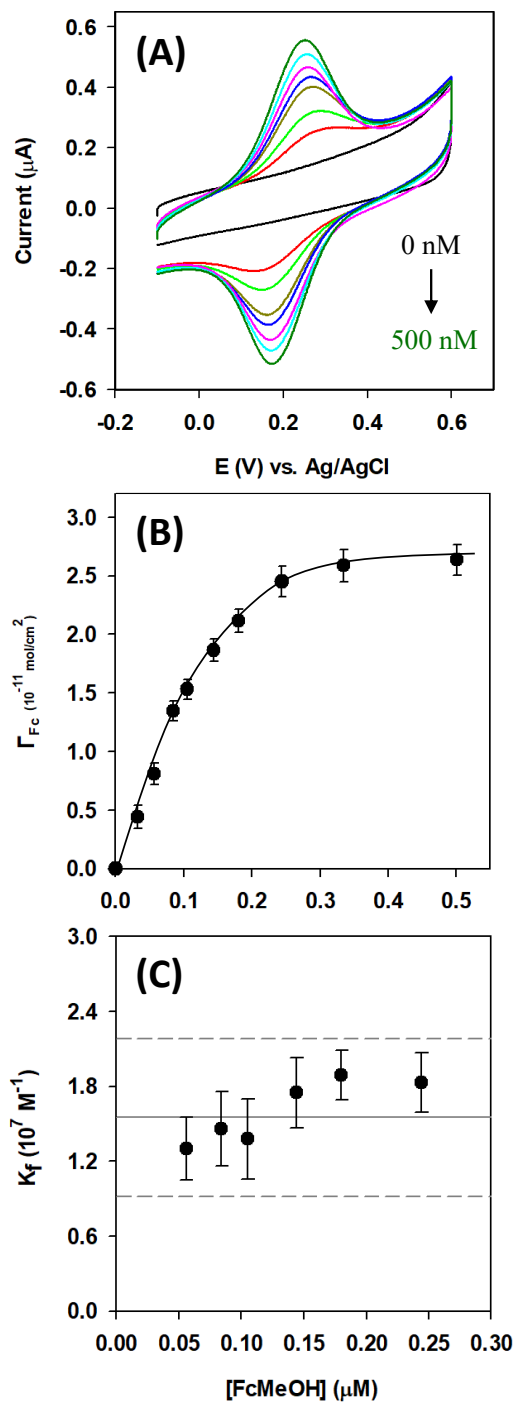


Figure 4.9 Thermodynamics study. (A) Representative CV responses upon treating the CB[7]-O-taz-C11S-Au in increasing FcMeOH concentrations. The scan rate was kept at 0.1 V/s. (B) Corresponding equilibrated surface density of FcMeOH@CB[7] (Γ_{Fc}) based on the integrated charge of the oxidation peaks from (A) as a function of [FcMeOH]. The solid line is to guide the eyes only. (C) Interfacial formation constant (K_f) determined at different [FcMeOH]. The solid and dashed lines show the average and standard deviation of the determined K_f values based on three independent replicates.

Note: Reprinted with permission from Ref 118. Copyright (2022), American Chemical Society.

In addition to the thermodynamic stability, a kinetic study, that is, to determine the binding (k_a) and dissociation (k_d) rate constants, is essential for a better understanding of the host-guest complexation on the surface and its practical application for the immobilization/conjugation chemistry. With the present system, it is easy to investigate the binding (complexing) kinetics as I can determine the surface density of the FcMeOH@CB[7] complex by performing CV measurements at different incubation periods. As displayed in Figure 4.10A, there were no discernible redox peaks at 20 s of the incubation in 100 nM FcMeOH; with a longer incubation time, the CV peaks resulting from the formation of FcMeOH@CB[7] complexes became progressively stronger. In particular, the determined Γ_{Fc} values (of interfacial FcMeOH@CB[7] complexes) increased initially and reached the maximum in about 200 min (Figure 4.10B). With the same assumption that all surface-immobilized CB[7] hosts are capable of complexing with FcMeOH guests, the amount of free $\Gamma_{CB[7]}$ can be estimated with Eq. (4.3). As illustrated in Eq. (4.4), this surface complexation reaction is a second-order process, in which both $\Gamma_{CB[7]}$ and the concentration of FcMeOH in the solution need to be taken into account. For this reason, the rate law is expressed as follows

$$rate = k_a \times [FcMeOH] \times \Gamma_{CB[7]} \quad (4.4)$$

where k_a is the second-order rate constant for the formation of the FcMeOH@CB[7] inclusion complex on the surface. As discussed above, the concentration of FcMeOH can be considered as a constant as it is in great excess compared to $\Gamma_{CB[7]}$; therefore, the rate law can be simplified to a pseudo-first-order equation

$$rate = k' \times \Gamma_{CB[7]} = k' \times [\Gamma_{Fc(max)} - \Gamma_{Fc(t)}] \quad (4.5)$$

where k' is the pseudo-first-order rate constant, which can be determined from the integrated rate law derived from Eq. (4.5)

$$\ln \left[\frac{\Gamma_{Fc(max)} - \Gamma_{Fc(t)}}{\Gamma_{Fc(max)}} \right] = \ln \left[1 - \frac{\Gamma_{Fc(t)}}{\Gamma_{Fc(max)}} \right] = -k' \times t \quad (4.6)$$

Based on the best linear fit to the correlation between $\ln[1 - \Gamma_{Fc(t)}/\Gamma_{Fc(max)}]$ and incubation time (t), the k' value was found to be $(2.6 \pm 0.3) \times 10^{-4} \text{ s}^{-1}$ (Figure 4.10C). In considering

the concentration of FcMeOH (100 nM) used in the measurements, the k_a for the binding between FcMeOH and surface-bound CB[7] was determined to be $(2.6 \pm 0.4) \times 10^3 \text{ M}^{-1} \text{ s}^{-1}$.

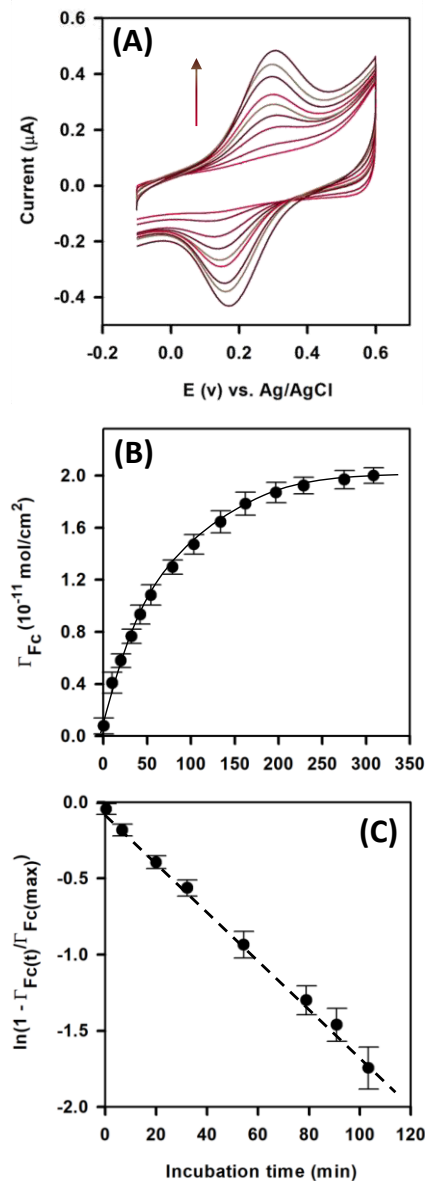


Figure 4.10 Association kinetic study. (A) Representative CV responses measured upon treating the CB[7]-O-taz-C11S-Au in 100 nM of FcMeOH prepared in 10 mM Tris-HClO₄ (pH 7.4) for different time period. The scan rate was kept at 0.1 V/s. (B) Corresponding surface density of FcMeOH@CB[7] (Γ_{Fc}) based on the integrated charge of the oxidation peaks from (A) as a function incubation time in 100 nM FcMeOH. (C) The relationship between $\ln [1 - \Gamma_{Fc(t)}/\Gamma_{Fc(max)}]$ and the incubation time (t). The dashed line is the best linear fit ($R^2 = 0.99$). The error bars represent standard deviations based on three independently prepared samples.

Note: Reprinted with permission from Ref 118. Copyright (2022), American Chemical Society.

It is also important to examine the dissociation process of FcMeOH from the FcMeOH@CB[7] inclusion complexes on the surface; as such, I have incubated CB[7]-O-taz-C11S-/C10S-Au in a high concentration of FcMeOH (1.0 μM) for a prolonged period of time (4 h) to reach the maximum surface density of FcMeOH@CB[7] complexes (maximum Γ_{Fc}). Upon transferring the sample to a FcMeOH-free buffer solution (10 mM Tris-HClO₄ at pH 7.4), the dissociation process of FcMeOH from the surface via CV measurements was monitored. As shown in Figure 4.11A, a notable decrease in the redox peak (represented by Γ_{Fc}) was observed within the first 30 min, but prolonged incubation shows only limited effect. Remarkably, there was less than 50% loss over a 4.5 h period (Figure 4.11B). Simpler than the binding kinetics, such a dissociation process can be directly treated as a first-order reaction so that its rate constant (k_d) can be determined from the following rate laws

$$\text{rate} = k_d \times \Gamma_{\text{Fc}(t)} \quad (4.7)$$

$$\ln \left[\frac{\Gamma_{\text{Fc}(t)}}{\Gamma_{\text{Fc}(\text{max})}} \right] = -k_d \times t \quad (4.8)$$

Indeed, the experimentally determined $\ln[\Gamma_{\text{Fc}(t)}/\Gamma_{\text{Fc}(\text{max})}]$ is inversely proportional to the incubation time (t). From the best linear fit to the experimental data as shown in Figure 4.11C, k_d was calculated to be $(5.1 \pm 0.3) \times 10^{-5} \text{ s}^{-1}$.

The difference between these rate constants and previously determined values ($k_a = 47 \pm 5 \text{ M}^{-1} \text{ s}^{-1}$ and $k_d = (1.3 \pm 0.2) \times 10^{-3} \text{ s}^{-1}$)³⁷ from the system where Fc guests are immobilized on the surface is substantial (Section 1.1.4); that is, the association rate constant is about three orders of magnitude larger, while the dissociation constant is much smaller. As mentioned above, this is related to the bulky size of CB[7] so that its attachment to azide-terminated SAMs occurs in an “isolated” but uniform manner (i.e., reduced steric hindrance in CuAAC), which permits the accommodation of FcMeOH guests to surface-bound CB[7] hosts facile and favorable. This is, in turn, leads to the inhibited dissociation of FcMeOH from FcMeOH@CB[7] complexes on the surface.

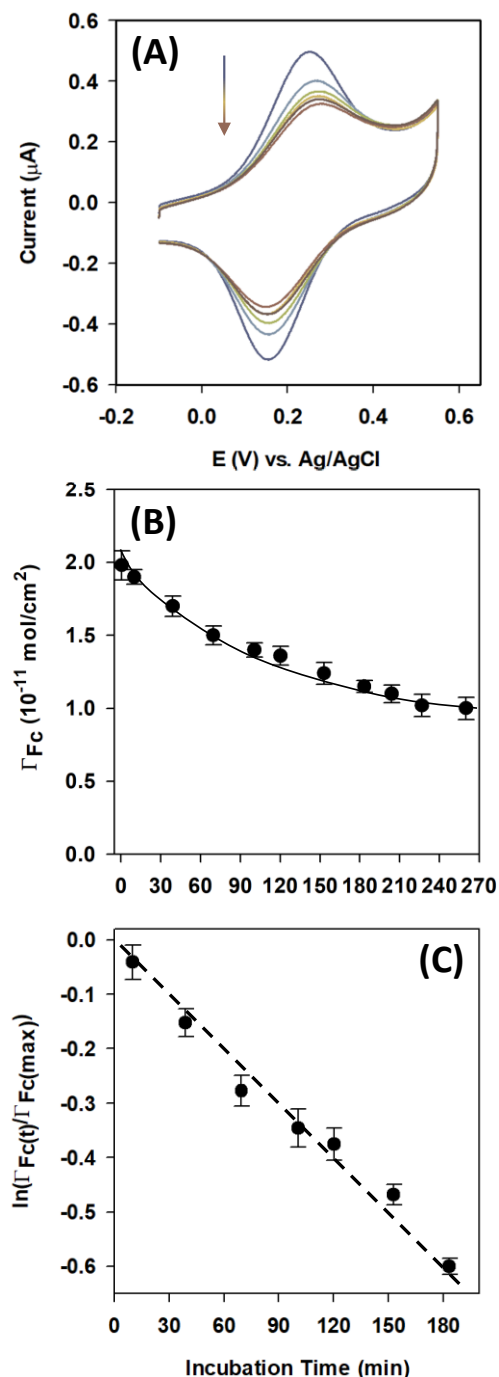


Figure 4.11 Dissociation kinetic study. (A) Representative CV responses after incubating a saturated FcMeOH@CB[7]-O-taz-C11S-Au in 10 mM Tris-HClO₄ (pH 7.4) that was free of FcMeOH for extended time. The scan rate was kept at 0.1 V/s. (B) Corresponding surface density of FcMeOH@CB[7] (Γ_{Fc}) based on the integrated charge of the oxidation peaks from (A) as a function incubation time in FcMeOH-free buffer. (C) The relationship between $\ln(\Gamma_{Fc}(t)/\Gamma_{Fc}(max))$ and the incubation time (t). The dashed line is the best linear fit ($R^2 = 0.99$). The error bars represent standard deviations based on three-independently prepared samples.

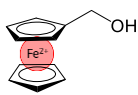
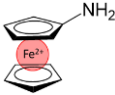
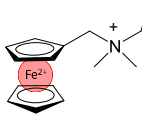
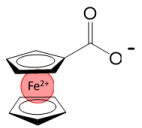
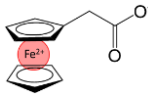
Note: Reprinted with permission from Ref 118. Copyright (2022), American Chemical Society.

The formation constant, $K_f = (5.1 \pm 0.8) \times 10^7 \text{ M}^{-1}$, calculated based on the ratio of the k_a and k_d determined above, is, in fact, similar to that directly determined from the law of mass action (Eq. (4.2)) with varying concentrations of FcMeOH. The somewhat smaller K_f from the “titration study” is likely due to the deviation from a true equilibrium, especially in the lower concentration range (Figure. 4.9C). Moreover, the different solution conditions (salt) besides FcMeOH concentration differences in these two types of measurements may also influence the accuracy of determining thermodynamic/kinetic constants; it has been shown that different metal cations interact with the electronegative carbonyl portals of CB[7] and influence the accuracy of CV measurements (different background currents).^{125,126} In fact, it is noticeable that the capacitive current continues to grow as the incubation time becomes longer in the CV scans (Figure 4.9A, & 4.10A), which suppresses the redox signals to some extent and makes the surface charge integration less accurate. Nevertheless, the general agreement presented above between the two K_f values confirms the validity of our thermodynamic and kinetic analyses of the formation of host–guest inclusion complexes on surface. More importantly, these K_f values are about three orders of magnitude higher than those previously determined when Fc guests were immobilized on the surface instead.³⁷ As discussed in Section 1.1.3 that Fc can adopt two different orientations within the CB[7] cage; one is more thermodynamically favored than the other.²⁰ As discussed above, in the present system, the absence of restriction on rotation freedom gives the solution-diffused Fc guests the mobility to orientate themselves into surface-immobilized CB[7] hosts to adopt a more stable configuration. Specifically, compared to the former system,³⁷ in which Fc guests might be buried within the SAMs or form clusters,⁶⁸ a more homogeneous distribution of CB[7] hosts on the surface is expected due to its bulked size and shape.¹⁵ This not only prevents surface-immobilized CB[7] hosts from getting too close to each other but also provides adequate space for Fc guests to access the CB[7] “cages.”

4.4. Surface-Immobilized CB[7] Hosts for Quantifying the Complexation with Other Fc Derivatives

As discussed in Section 1.1.2, unlike other synthetic macrocyclic host molecules, such as cyclodextrin (CD), the symmetric electronegative carbonyl portals of CB[7] “invite” additional non-covalent interactions (ion–dipole and dipole–dipole) to the complexation system for achieving ultrahigh stability with Fc derivatives in the solution.^{2,20,21} Hence, for a better understanding of the formation of host–guest inclusion complexes on the surface, a set of representative Fc derivatives for complexing with surface-immobilized CB[7] hosts was explored. Besides FcMeOH tested above, both neutral (FcNH₂)¹²⁷ and charged compounds ((FcN⁺Br⁻, FcCOO⁻, and FcAcCOO⁻) were chosen; by controlling the pH with Tris-HClO₄ buffer at pH 7.4, the FcCOO⁻ and FcAcCOO⁻ are in their deprotonated forms (i.e., negatively charged).¹²⁸ As shown in Figure 4.12, representative CV responses when incubating CB[7]-O-taz-C11S-/C10S-Au with selected Fc derivatives showed significant differences (particularly when varying their concentrations). Based on these CV data and following the same procedure as outlined above, the respective formation constants for these Fc derivatives are summarized in Table 4.1.

Table 4.1 Formation constants (K_f) of selective Fc derivatives toward CB[7]-O-taz-C11S-Au.

Fc Derivative	FcMeOH	FcNH ₂	FcN ⁺ Br ⁻	FcCOO ⁻	FcAcCOO ⁻
Fc Structure					
K_f (10^7 M^{-1})	1.6 0.5	22 4	66 8	no discernible binding	1.2 0.3

All the K_f were calculated based on CV results upon incubation in increasing concentrations (10 – 500 nM) of each of the Fc derivatives prepared in 10.0 mM Tris-HClO₄ (pH 7.4).

Note: Reprinted with permission from Ref 118. Copyright (2022), American Chemical Society.

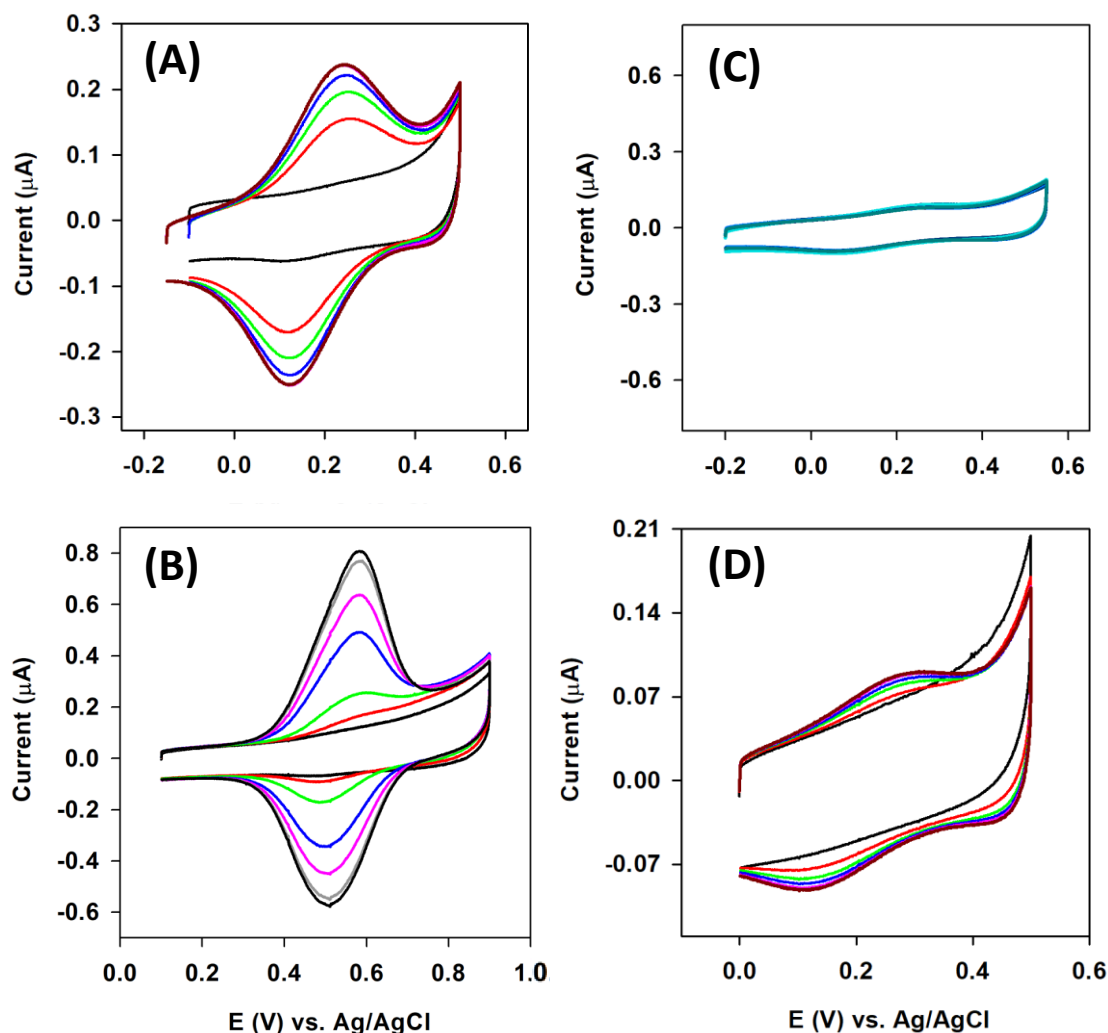


Figure 4.12 Representative cyclic voltammograms of individual CB[7]-O-taz-C11S-Au treating in increasing concentrations (0 - 450 nM) of (A) FcNH₂, (B) FcN⁺Br⁻, (C) FcCOO⁻, and (D) FcAcCOO⁻. The scan rate was kept at 0.1 V/s.

Note: Reprinted with permission from Ref 118. Copyright (2022), American Chemical Society.

Though FcMeOH and FcNH₂ are neutral at pH 7.4, the K_f of the latter is ten times larger, which is in agreement with the results observed in the solution (10^{12} vs 10^9 M⁻¹).¹²⁹ At the same time, the K_f of FcN⁺Br⁻ is $(6.6 \pm 0.8) \times 10^8$ M⁻¹, which is much higher than that of neutral derivatives (e.g., FcMeOH). It is believed that this is likely attributed to the positively charged substituents that generate favorable ion-dipole interactions with the electronegative carbonyl portals of CB[7].^{21,22} Different from the pronounced CV responses for FcNH₂ (Figure 4.12A) and FcN⁺Br⁻ (Figure 4.12B), no discernible binding was observed between FcCOO⁻ guests and surface-immobilized CB[7] hosts as the CV

curves overlapped with each other with no clear Faradic responses; even the concentration of FcCOO^- continued to increase (Figure 4.12C). This agrees with the observation of Jeon et al. in the solution,²⁰ which makes the determination of K_f not feasible. However, with an additional methyl group (-CH₂-) to position -COO⁻ away from the ferrocene core, a pair of redox peaks gradually appeared when CB[7]-O-taz-C11S-/C10S-Au was treated in increased concentrations of deprotonated FcAcCOO^- (Figure 4.12D). In addition, the corresponding K_f is determined to be $(1.2 \pm 0.3) \times 10^7 \text{ M}^{-1}$. The complexation indeed occurs likely because of the increased distance between the negatively charged substitute and the Fc core as the electrostatic repulsion with the carbonyl portals of CB[7] becomes less effective.³⁰ Even though its K_f is at the same magnitude as that of FcMeOH toward the surface-immobilized CB[7], the significantly low Γ_{Fc} (Figure 4.12D vs. Figure 4.9A) suggests that the binding with the surface-immobilized CB[7] is not kinetically favorable. As discussed by Kaifer et al.,¹³⁰ the negative charges on the substituent exert a repulsion toward the carbonyl portals, creating a higher activation barrier to be accommodated inside the CB[7] chamber. With these results, it is evident that “clicking” $\equiv\text{-O-CB[7]}$ onto pre-assembled azide-terminated SAMs does not affect the capability of CB[7] hosts for recognizing structural differences of Fc derivatives.

4.5. Obstacles and Potential for Future Applications.

The data presented above, particularly the different complexation affinities between surface-bound CB[7] hosts and Fc guests in the solution, demonstrate that the choice of an appropriate Fc derivative as the tag for the desired biological macromolecules and the length of the linker that connects the Fc tag are crucial. The former is to enable the efficient binding of the Fc-labeled biomolecules toward surface-immobilized CB[7], and the latter is to compensate for the electrostatic repulsion exerted by the electronegative carbonyl portals of CB[7]. Furthermore, the type and concentration of salts in the buffer should be carefully examined as studies have pointed out that they can interact with the carbonyl portals of CB[7] to reduce the K_f of Fc@CB[7] by competition.^{125,126} Nevertheless, it has

been managed to prepare biosensors and molecular devices with neutral Fc derivatives or by incorporating a positively charged ferrocene moiety onto a biomolecule such that the above mentioned obstacles can be overcome.^{10,38,40} The overall quality of thus prepared biosensing surfaces is exceptional, with high sensitivity and specificity in recognizing targeted molecules/analytes.

Chapter 5.

Summary and Future Direction

5.1. Conclusions

In summary, the covalent attachment of $\equiv\text{O-CB}[7]$ onto binary azide-terminated SAMs on gold via CuAAC is efficient and can be readily evaluated using both surface analysis and electrochemical techniques. The surface-bound CB[7] hosts retain their capability toward binding various Fc guests, and the process can be quantitatively analyzed based on conventional CV measurements. Remarkably, the formation constants of interfacial FcMeOH@CB[7] host-guest inclusion complexes are three orders of magnitude higher than those determined previously (CB[7] on Fc-terminated SAMs), which makes it an “ideal” platform for studying the binding behavior of CB[7] toward different Fc derivatives on the surface. This is likely attributed to the unperturbed rotational freedom of the Fc derivatives in solutions that allow them to adopt the more energetically favorable orientation within the “cage” of surface-immobilized CB[7] hosts. By and large, this study augments the feasibility of using a supramolecular inclusion complex as a novel conjugation pair for the development of biosensors and molecular devices.

5.2. Future Work

As the ultimate goal of this research was to exploring potential application of supramolecular host-guest pairs as immobilization/conjugation motifs for the development of biosensors and other molecular devices with improved sensitivity and reliability (reproducibility), an immediate study would be tethering Fc-labelled DNA strands on surface via the formation the formation of interfacial Fc@CB[7] complexes and creating a ratiometric electrochemical sensor. The concept of ratiometric sensors can traced back to the seminal work of Ellington and co-workers in 2014.⁷⁶ It was achieved by incorporating

two redox-active tags on the same DNA probe but at different positions: one serves as the signal probe, whose electrochemical signal changes upon target binding; the other serves as an internal reference, whose signal remains constant regardless of the target binding (Figure 5.1A).⁷⁶ The detection was carried out by monitoring the current ratio between the signal probe and the internal reference after target binding.

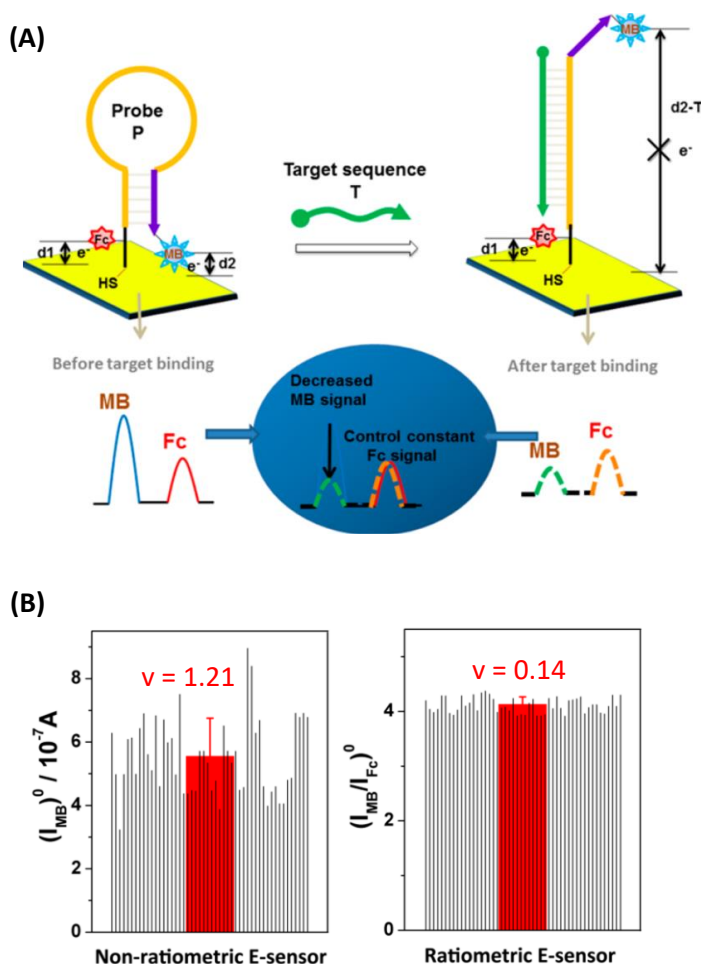


Figure 5.1 (A) Schematic illustrating the mechanism of the electrochemical DNA sensor with ratiometric analyses. The distance between the ferrocene tag (Fc) and the gold electrode remains unchanged before and after the binding of the target sequence (T) to the DNA probe (P), whereas the electrons transfer from methylene blue (MB) to the electrode surface get disrupted due to the elongated distance after T binding. (B) Comparison on the background signals (before target binding) measured from 2 sets of 50 individual electrode samples prepared based on the (left) single-labelled method and the (right) dual-labelled method (ratiometric analyses). The black histograms represent the background responses of 50 individual measurements over eight electrodes. Average values are represented by the red bars, and the red error bars in the red bars represented the SD for 50 individual measurements.

Note: Adapted with permission from Ref 76. Copyright (2014), American Chemical Society.

The significance of employing the ratiometric strategy (dual labelling) is the improvement in the reproducibility that has been discussed in Section 1.2.2 (e.g., clustering and aggregation of DNA probes on surface). As shown in Figure 5.1B (left), the standard deviation (SD) obtained using 8 electrodes (including the same electrodes on different days and different electrodes on the same day) with the ratiometric design only has a variance of 0.14, which is remarkably lower by an order of magnitude than the one (1.21) obtained from the conventional design (single labelling). Thus, the ratiometric approach is far more robust, reliable, and reproducible than the classic design which relies on electrochemical “absolute value”.

As depicted in Figure 5.2, we can adapt the supramolecular conjugation motif investigated in this thesis to design a novel ratiometric DNA sensor for either DNA or protein targets. In this case, the ferrocene guest not only serves as a conjugation probe for attaching Fc-labelled biomolecules (e.g., DNA probes) to the surface-immobilized CB[7] but also acts as the internal reference. A multiply charged redox cation, like hexaammineruthenium (III) ($[\text{Ru}(\text{NH}_3)_6]^{3+}$), which binds electrostatically to the negatively charged DNA phosphate backbone,⁶⁶ can be employed as the redox label for monitoring the binding of target to the surface. Upon incubation of such electrode with a solution containing analytes (e.g., hen egg white protein lysozyme), the surface CV response decreases substantially due to the reduction in the binding sites on the phosphate backbone for electrostatic interaction with $[\text{Ru}(\text{NH}_3)_6]^{3+}$ (Figure 5.2). As a result, decreases in the relative currents ($I_{[\text{Ru}(\text{NH}_3)_6]^{3+}}/I_{\text{Fc}}$) reflect the target analyte binding events taking place on the electrode surface, and can be used to construct a dose-response curve.

The proposed detection system possesses following key features: (1) the pre-assembled binary SAMs prevent the non-specific binding of DNA probe onto the surface; (2) the bulk-size, surface-immobilized CB[7] can prevent DNA probes from forming clusters and aggregates; (3) the number of DNA probes can be determined based on the 1:1 host-guest binding between the Fc and CB[7]; and (4) the introduction of a redox cation allows for the target quantitation based on the signal ratio between the two tags.

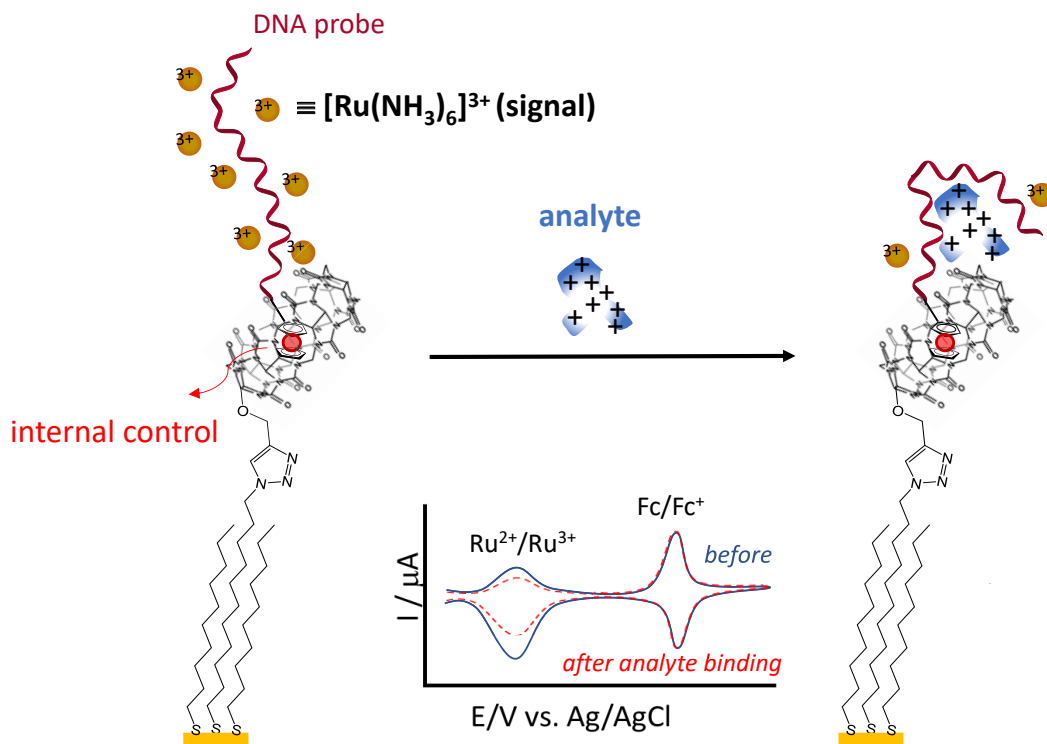


Figure 5.2 Schematic view of employing Fc@CB[7] as the conjugation motif for constructing ratiometric electrochemical biosensors. a redox cation (e.g., $[\text{Ru}(\text{NH}_3)_6]^{3+}$) will be adapted as the second signal probe. Note: details need to be presented for people to understand the entire design.

In fact, this robust interfacial Fc@CB[7] host-guest inclusion complex can be utilized for preparing many other types of biosensors and molecular devices with desirable functions. Beyond the gold substrate that is ideal for electrochemical studies, other more popular biochip substrates, such as glass and silicon, should be also examined for immobilizing supramolecular hosts and forming inclusive complexes with functional guests. Not only the surface chemistry needs to be investigated, but also the choice of guests that have either optical or redox properties deserves further screening and development. Of course, beyond CB[7], other cucurbit[n]uril homologues that have different, and exciting properties can be new topics of future studies.

References

- (1) Wright, D. S. 1.30 – Host-guest chemistry – p-block systems. In *Comprehensive inorganic chemistry II from elements to applications*, 2nd ed.; Reedijk, J., Poeppelmeier, K., Eds.; Elsevier: Burlington, 2013; 953-967.
- (2) Shetty, D.; Khedkar, J. K.; Park, K. M.; Kim, K. Can we beat the biotin-avidin pair?: cucurbit[7]uril-based ultrahigh affinity host-guest complexes and their applications. *Chem. Soc. Rev.* **2015**, *44*, 8747–8761. <https://doi.org/10.1039/c5cs00631g>.
- (3) Rekharsky, M. V; Inoue, Y. Complexation thermodynamics of cyclodextrins. *Chem. Rev.* **1998**, *98*, 1875-1918. <https://doi.org/10.1021/cr970015o>.
- (4) González, M.; Argaraña, C. E.; Fidelio, G. D. Extremely high thermal stability of streptavidin and avidin upon biotin binding. *Biomol. Eng.* **1999**, *16*, 67–72. [https://doi.org/10.1016/S1050-3862\(99\)00041-8](https://doi.org/10.1016/S1050-3862(99)00041-8).
- (5) Avidin-biotin interaction. Thermo Fisher Scientific. <https://www.thermofisher.com/ca/en/home/life-science/protein-biology/protein-biology-learning-center/protein-biology-resource-library/pierce-protein-methods/avidin-biotin-interaction.html> (accessed Jan 29, 2022).
- (6) Masarik, M.; Kizek, R.; Kramer, K. J.; Billova, S.; Brazdova, M.; Vacek, J.; Bailey, M.; Jelen, F.; Howard, J. A. Application of avidin-biotin technology and adsorptive transfer stripping square-wave voltammetry for detection of dna hybridization and avidin in transgenic avidin maize. *Anal. Chem.* **2003**, *75*, 2663–2669. <https://doi.org/10.1021/ac020788z>
- (7) Jain, A.; Cheng, K. The principles and applications of avidin-based nanoparticles in drug delivery and diagnosis. *J. Control Release.* **2017**, *245*, 27–40. <https://doi.org/10.1016/j.jconrel.2016.11.016>.
- (8) Cartun, R. W.; Taylor, C. R.; Dabbs, D. J. Techniques of immunohistochemistry: principles, pitfalls, and standardization. In *Diagnostic Immunohistochemistry Theranostic and Genomic Applications*, 5th ed.; Dabbs, D. J., Ed; Elsevier, 2017; pp 1-46
- (9) Hermanson, G. T. (Strept)avidin-biotin systems. In *Bioconjugate Techniques*, 3rd ed.; Audet, J., Preap, M., Eds.; Academic Press: London, 2013; 465-505.
- (10) Hwang, I.; Baek, K.; Jung, M.; Kim, Y.; Kyeng, M. P.; Lee, D. W.; Selvapalam, N.; Kim, K. Noncovalent immobilization of proteins on a solid surface by cucurbit[7]uril-ferrocenemethylammonium pair, a potential replacement of biotin-avidin pair. *J. Am. Chem. Soc.* **2007**, *129*, 4170–4171. <https://doi.org/10.1021/ja071130b>.

- (11) Heinz, T.; Rudkevich, D. M.; Rebek, J. Pairwise selection of guests in a cylindrical molecular capsule of nanometre dimensions. *Nature*. **1998**, *394*, 764–766. <https://doi.org/10.1038/29501>.
- (12) Zhang, C.; Wang, H.; Zhong, J.; Lei, Y.; Du, R.; Zhang, Y.; Shen, L.; Jiao, T.; Zhu, Y.; Zhu, H.; Li, H.; Li, H. A mutually stabilized host-guest pair. *Sci. Adv.* **2019**, *5*, 6707–6708. <https://doi.org/10.1126/SCIADV.AAX6707>.
- (13) Ma, Y.-L.; Sun, C.; Li, Z.; Wang, Z.; Wei, J.; Cheng, Q.; Zheng, L.-S.; Chang, X.-Y.; Li, K.; Wang, R.; Jiang, W. Biomimetic recognition-based bioorthogonal host-guest pairs for cell targeting and tissue imaging in living animals. *CCS Chem.* **2021**, *3*, 2143–2155. <https://doi.org/10.31635/ccschem.021.202101178>.
- (14) Behrend, R.; Meyer, E.; Rusche, F. Condensation products from glycoluri and formaldehyde. *Liebigs Ann. Chem.* **1905**, *339*, 1–37. <https://doi.org/10.1002/JLAC.19053390102>.
- (15) Lee, J. W.; Samal, S.; Selvapalam, N.; Kim, H.-J.; Kim, K. Cucurbituril homologues and derivatives: new opportunities in supramolecular chemistry. *Acc. Chem. Res.* **2003**, *36*, 621–630. <https://doi.org/10.1021/ar020254k>.
- (16) Isaacs, L. The mechanism of cucurbituril formation. *Isr. J. Chem.* **2011**, *51*, 578–591. <https://doi.org/10.1002/ijch.201100022>.
- (17) Hwang, I.; Jeon, W. S.; Kim, H. J.; Kim, D.; Kim, H.; Selvapalam, N.; Fujita, N.; Shinkai, S.; Kim, K. Cucurbit[7]uril: a simple macrocyclic, ph-triggered hydrogelator exhibiting guest-induced stimuli-responsive behavior. *Angew. Chem. Int. Ed.* **2007**, *46*, 210–213. <https://doi.org/10.1002/anie.200603149>.
- (18) Bardelang, D.; Udachin, K. A.; Leek, D. M.; Margeson, J. C.; Chan, G.; Ratcliffe, C. I.; Ripmeester, J. A. Cucurbit[n]urils (n = 5–8): a comprehensive solid state study. *Cryst. Growth Des.* **2011**, *11*, 5598–5614. <https://doi.org/10.1021/cg201173j>.
- (19) Chio, W. I. K.; Xie, H.; Zhang, Y.; Lan, Y.; Lee, T. C. SERS biosensors based on cucurbituril-mediated nanoaggregates for wastewater-based epidemiology. *Trends Anal. Chem.* **2022**, *146*, 116485–116493. <https://doi.org/10.1016/j.trac.2021.116485>.
- (20) Jeon, W. S.; Moon, K.; Park, S. H.; Chun, H.; Ko, Y. H.; Lee, J. Y.; Lee, E. S.; Samal, S.; Selvapalam, N.; Rekharsky, M. V.; Sindelar, V.; Sobransingh, D.; Inoue, Y.; Kaifer, A. E.; Kim, K. Complexation of ferrocene derivatives by the cucurbit[7]uril host: a comparative study of the cucurbituril and cyclodextrin host families. *J. Am. Chem. Soc.* **2005**, *127*, 12984–12989. <https://doi.org/10.1021/ja052912c>.
- (21) Cui, L.; Gadde, S.; Li, W.; Kaifer, A. E. Electrochemistry of the inclusion complexes formed between the cucurbit [7]uril host and several cationic and neutral ferrocene derivatives. *Langmuir*. **2009**, *25*, 13763–13769. <https://doi.org/10.1021/la9015096>.

- (22) Yi, S.; Li, W.; Nieto, D.; Cuadrado, I.; Kaifer, A. E. Probing the tolerance of cucurbit[7]uril inclusion complexes to small structural changes in the guest. *Org. Biomol. Chem.* **2013**, *11*, 287–293. <https://doi.org/10.1039/c2ob26834e>.
- (23) Szejtli, J. Introduction and General Overview of Cyclodextrin Chemistry. *Chem. Rev.* **1998**, *98*, 1743–1754. <https://doi.org/10.1021/cr970022c>.
- (24) Ogoshi, T.; Yamagishi, T.-A. Chapter 1: Historical Background of macrocyclic compounds. In *Pillararenes: monographs in supramolecular chemistry*; Ogoshi, T., Ed; The Royal Society of Chemistry: Cambridge; 1–22.
- (25) Szejtli, J. Utilization of cyclodextrins in industrial products and processes. *J. Mater. Chem.* **1997**, *7*, 575–587. <https://doi.org/10.1039/A605235E>.
- (26) Kim, K.; Selvapalam, N.; Hyun, D. O. Cucurbiturils—a new family of host molecules. *J. Incl. Phenom. Macrocycl. Chem.* **2004**, *50*, 31–36. <https://doi.org/10.1007/s10847-004-8835-7>.
- (27) Chen, Y.; Klimczak, A.; Galoppini, E.; Lockard, J. V. Structural interrogation of a cucurbit[7]uril-ferrocene host-guest complex in the solid state: a raman spectroscopy study. *RSC Advances.* **2013**, *3*, 1354. <https://doi.org/10.1039/c2ra21584e>.
- (28) Rekharsky, M. V.; Mori, T.; Yang, C.; Ko, Y. H.; Selvapalam, N.; Kim, H.; Sobransingh, D.; Kaifer, A. E.; Liu, S.; Isaacs, L.; Chen, W.; Moghaddam, S.; Gilson, M. K.; Kim, K. A synthetic host-guest system achieves avidin-biotin affinity by overcoming enthalpy-entropy compensation. *PNAS.* **2007**, *104*, 20737–20742. <https://doi.org/10.1073/pnas.0706407105>.
- (29) Ong, W.; Kaifer, A. E. Unusual electrochemical properties of the inclusion complexes of ferrocenium and cobaltocenium with cucurbit[7]uril. *Organometallics.* **2003**, *22* (21), 4181–4183. <https://doi.org/10.1021/om030305x>.
- (30) Sobransingh, D.; Kaifer, A. E. New dendrimers containing a single cobaltocenium unit covalently attached to the apical position of newkome dendrons: electrochemistry and guest binding interactions with cucurbit[7]uril. *Langmuir.* **2006**, *22*, 10540–10544. <https://doi.org/10.1021/la061188o>.
- (31) Marquez, C.; Nau, W. M. Polarizabilities inside molecular containers. *Angew. Chem. Int. Ed.* **2001**, *40*, 4387–4390. [https://doi.org/10.1002/1521-3773\(20011203\)40:23<4387::AID-ANIE4387>3.0.CO;2-H](https://doi.org/10.1002/1521-3773(20011203)40:23<4387::AID-ANIE4387>3.0.CO;2-H).
- (32) Moghaddam, S.; Yang, C.; Rekharsky, M.; Ko, Y. H.; Kim, K.; Inoue, Y.; Gilson, M. K. New ultrahigh affinity host-guest complexes of cucurbit[7]uril with bicyclo[2.2.2]octane and adamantane guests: thermodynamic analysis and evaluation of m2 affinity calculations. *J. Am. Chem. Soc.* **2011**, *133*, 3570–3581. <https://doi.org/10.1021/ja109904u>.

- (33) Cao, L.; Šekutor, M.; Zavalij, P. Y.; Mlinarić-Majerski, K.; Glaser, R.; Isaacs, L. Cucurbit[7]uril-guest pair with an attomolar dissociation constant. *Angew. Chem. Int. Ed.* **2014**, *53*, 988–993. <https://doi.org/10.1002/anie.201309635>.
- (34) Šekutor, M.; Molčanov, K.; Cao, L.; Isaacs, L.; Glaser, R.; Mlinarić-Majerski. Design, synthesis, and x-ray structural analyses of diamantane diammonium salts: guests for cucurbit[n]uril hosts. *Eur. J. Org. Chem.* **2014**, 2533–2542. <http://dx.doi.org/10.1002/ejoc.201301844>.
- (35) Liu, S.; Ruspic, C.; Mukhopadhyay, P.; Chakrabarti, S.; Zavalij, P. Y.; Isaacs, L. The cucurbit[n]uril family: prime components for self-sorting systems. *J. Am. Chem. Soc.* **2005**, *127*, 15959–15967. <https://doi.org/10.1021/ja055013x>.
- (36) Fabbrizzi, L. The ferrocenium/ferrocene couple: a versatile redox switch. *ChemTexts.* **2020**, *6*, 1–20. <https://doi.org/10.1007/s40828-020-00119-6>.
- (37) Qi, L.; Tian, H.; Shao, H.; Yu, H. Z. Host-guest interaction at molecular interfaces: binding of cucurbit[7]uril on ferrocenyl self-assembled monolayers on gold. *J. Phys. Chem. C.* **2017**, *121*, 7985–7992. <https://doi.org/10.1021/acs.jpcc.7b01135>.
- (38) Lee, D. W.; Park, K. M.; Gong, B.; Shetty, D.; Khedkar, J. K.; Baek, K.; Kim, J.; Ryu, S. H.; Kim, K. A simple modular aptasensor platform utilizing cucurbit[7]uril and a ferrocene derivative as an ultrastable supramolecular linker. *Chem. Commun.* **2015**, *51*, 3098–3101. <https://doi.org/10.1039/c4cc08027k>.
- (39) Neiryneck, P.; Brinkmann, J.; An, Q.; van der Schaft, D. W. J.; Milroy, L. G.; Jonkheijm, P.; Brunsveld, L. Supramolecular control of cell adhesion via ferrocene-cucurbit[7]uril host-guest binding on gold surfaces. *Chem. Commun.* **2013**, *49*, 3679–3681. <https://doi.org/10.1039/c3cc37592g>.
- (40) Lee, D. W.; Park, K. M.; Banerjee, M.; Ha, S. H.; Lee, T.; Suh, K.; Paul, S.; Jung, H.; Kim, J.; Selvapalam, N.; Ryu, S. H.; Kim, K. Supramolecular fishing for plasma membrane proteins using an ultrastable synthetic host-guest binding pair. *Nat. Chem.* **2011**, *3*, 154–159. <https://doi.org/10.1038/nchem.928>.
- (41) Vinciguerra, B.; Cao, L.; Cannon, J. R.; Zavalij, P. Y.; Fenselau, C.; Isaacs, L. Synthesis and self-assembly processes of monofunctionalized cucurbit[7]uril. *J. Am. Chem. Soc.* **2012**, *134*, 13133–13140. <https://doi.org/10.1021/ja3058502>.
- (42) Burneet, C. A.; Lagona, L.; Wu, A.; Shaw, J. A.; Coady, D.; Fettingner, J. C.; Day, A. I.; Isaacs, L. Preparation of glycoluril monomers for expanded cucurbit[n]uril synthesis. *Tetrahedron.* **2003**, *59*, 1961–1970. [http://dx.doi.org/10.1016/S0040-4020\(03\)00150-9](http://dx.doi.org/10.1016/S0040-4020(03)00150-9).
- (43) Jon, S. Y.; Selvapalam, N.; Oh, D. H.; Kang, J. K.; Kim, S. Y.; Jeon, Y. J.; Lee, J. W.; Kim, K. Facile synthesis of cucurbit[n]uril derivatives via direct functionalization: expanding utilization of cucurbit[n]uril. *J. Am. Chem. Soc.* **2003**, *125*, 10186–10187. <https://doi.org/10.1021/ja036536c>.

- (44) Ayhan, M. M.; Karoui, H.; Hardy, M.; Rockenbauer, A.; Charles, L.; Rosas, R.; Udachin, K.; Tordo, P.; Bardelang, D.; Ouari, O. Comprehensive synthesis of monohydroxy-cucurbit[n]urils (n = 5, 6, 7, 8): high purity and high conversions. *J. Am. Chem. Soc.* **2015**, *137*, 10238–10245. <https://doi.org/10.1021/jacs.5b04553>.
- (45) Ayhan, M. M.; Karoui, H.; Hardy, M.; Rockenbauer, A.; Charles, L.; Rosas, R.; Udachin, K.; Tordo, P.; Bardelang, D.; Ouari, O. Correction: comprehensive synthesis of monohydroxy-cucurbit[n]urils (n = 5, 6, 7, 8): high purity and high conversions. *J. Am. Chem. Soc.* **2016**, *138*, 2060. <https://doi.org/10.1021/jacs.6b00188>
- (46) Ahn, Y.; Jang, Y.; Selvapalam, N.; Yun, G.; Kim, K. Supramolecular velcro for reversible underwater adhesion. *Angew. Chem. Int. Ed.* **2013**, *52*, 3140–3144. <https://doi.org/10.1002/anie.201209382>.
- (47) Ashworth, I. W.; Nelson, D. J.; Percy, J. M. Solvent effects on grubbs' pre-catalyst initiation rates. *Dalt. Trans.* **2013**, *42*, 4110–4113. <https://doi.org/10.1039/C2DT32441E>.
- (48) An, Q.; Li, G.; Tao, C.; Li, Y.; Wu, Y.; Zhang, W. A general and efficient method to form self-assembled cucurbit[n]uril monolayers on gold surfaces. *Chem. Commun.* **2008**, *17*, 1989–1991. <https://doi.org/10.1039/b719927a>.
- (49) Love, J. C.; Estroff, L. A.; Kriebel, J. K.; Nuzzo, R. G.; Whitesides, G. M. Self-assembled monolayers of thiolates on metals as a form of nanotechnology. *Chem. Rev.* **2005**, *105*, 1103–1170. <https://doi.org/10.1021/cr0300789>.
- (50) Clasohm, L. Y.; Chen, M.; Knoll, W.; Vinogradova, O. I.; Horn, R. G. Self-assembled monolayers on mercury probed in a modified surface force apparatus. *J. Phys. Chem. B.* **2006**, *110*, 25931–25940. <https://doi.org/10.1021/jp062340y>.
- (51) Ostuni, E.; Chapman, R. G.; Liang, M. N.; Meluleni, G.; Pier, G.; Ingber, D. E.; Whitesides, G. M. Self-assembled monolayers that resist the adsorption of proteins and the adhesion of bacterial and mammalian cells. *Langmuir.* **2001**, *17*, 6336–6343. <https://doi.org/10.1021/la010552a>.
- (52) Bamdad, C. A DNA self-assembled monolayer for the specific attachment of unmodified double- or single-stranded DNA. *Biophys. J.* **1998**, *75*, 1997–2003. [https://doi.org/10.1016/S0006-3495\(98\)77641-6](https://doi.org/10.1016/S0006-3495(98)77641-6).
- (53) Levicky, R.; Herne, T. M.; Tarlov, M. J.; Satija, S. K. Using self-assembly to control the structure of DNA monolayers on gold: a neutron reflectivity study. *J. Am. Chem. Soc.* **1998**, *120*, 9787–9792. <https://doi.org/10.1021/ja981897r>.
- (54) Bain, C. D.; Troughton, E. B.; Tao, Y. T.; Evall, J.; Whitesides, G. M.; Nuzzo, R. G. Formation of monolayer films by the spontaneous assembly of organic thiols from solution onto gold. *J. Am. Chem. Soc.* **1989**, *111*, 321–335. <https://doi.org/10.1021/ja00183a049>.

- (55) Wetterer, S. M.; Lavrich, D. J.; Cummings, T.; Bernasek, S. L.; Scoles, G. Energetics and kinetics of the physisorption of hydrocarbons on Au(111). *J. Phys. Chem. B*. **1998**, *102*, 9266-9275. <https://doi.org/10.1021/jp982338>.
- (56) Vericat, C.; Vela, M. E.; Benitez, G.; Carro, P.; Salvarezza, R. C. Self-assembled monolayers of thiols and dithiols on gold: new challenges for a well-known system. *Chem. Sov. Rev.* **2010**, *39*, 1805-1834. <https://doi.org/10.1039/b907301a>.
- (57) Zbieta, E.; Stolarczyk, U.; Sidoryk, K.; Cybulski, M.; Kubiszewski, M.; Stolarczyk, K. Design of therapeutic self-assembled monolayers of thiolated abiraterone. *Nanomaterials*. **2018**, *8*, 1018-1032. <https://doi.org/10.3390/nano8121018>.
- (58) Eckermann, A. L.; Feld, D. J.; Shaw, J. A.; Meade, T. J. Electrochemistry of redox-active self-assembled monolayers. *Coord. Chem. Rev.* **2010**, *254*, 1769–1802. <https://doi.org/10.1016/j.ccr.2009.12.023>.
- (59) Angnes, L.; Richter, E. M.; Augelli, M. A.; Kume, G. H. Gold electrodes from recordable CDs. *Anal. Chem.* **2000**, *72*, 5503–5506. <https://doi.org/10.1021/AC000437P>.
- (60) Laibinis, P. E.; Fox, M. A.; Folkers, J. P.; Whitesides, G. M. Comparisons of self-assembled monolayers on silver and gold: mixed monolayers derived from HS(CH₂)₂₁X and HS(CH₂)₁₀Y (X, Y = CH₃, CH₂OH) have similar properties. *Langmuir*. **1991**, *7*, 3167–3173. <https://doi.org/10.1021/la00060a041>.
- (61) Jiang, X.; Bruzewicz, D. A.; Thant, M. M.; Whitesides, G. M. Palladium as a substrate for self-assembled monolayers used in biotechnology. *Anal. Chem.* **2004**, *76*, 6116-6121. <https://doi.org/10.1021/ac049152t>.
- (62) Dilimon, V. S.; Fonder, G.; Delhalle, J.; Mekhalif, Z. Self-assembled monolayer formation on copper: a real time electrochemical impedance study. *J. Phys. Chem. C*. **2011**, *115*, 18202–18207. <https://doi.org/10.1021/jp203652y>.
- (63) Carvalho, A.; Geissler, M.; Schmid, H.; Michel, B.; Delamarche, E. Self-assembled monolayers of eicosanethiol on palladium and their use in microcontact printing. *Langmuir*. **2002**, *18*, 2406-2412. <https://doi.org/10.1021/la015596y>.
- (64) Petrovykh, D. Y.; Kimura-Suda, H.; Opdahl, A.; Lee, J. R.; Richter, J.; Tarlov, M. J.; Whitman, L. J. Alkanethiols on platinum: multicomponent self-assembled monolayers. *Langmuir*. **2006**, *22*, 2578-2587. <https://doi.org/10.1021/la050928a>.
- (65) Lee, Y.-H.; Hu, C.-C. Mercury drop electrodes. In *Encyclopedia of Applied Electrochemistry*; Kreysa, G., Ota, K.-I., Savinell, R. F., Eds.; Springer: New York, 2014; 1233-1240.

- (66) Yu, H.-Z.; Luo, C.-Y.; Sankar, C. G.; Sen, D.; Voltammetric procedure for examining DNA-modified surfaces: quantitation, cationic binding activity, and electron-transfer kinetics. *Anal. Chem.* **2014**, *75*, 3902-3907. <https://doi.org/10.1021/ac034318w>.
- (67) Tian, H.; Xiang, D.; Shao, H.; Yu, H. Z. Electrochemical identification of molecular heterogeneity in binary redox self-assembled monolayers on gold. *J. Phys. Chem. C.* **2014**, *118*, 13733–13742. <https://doi.org/10.1021/jp5040745>.
- (68) Qi, L.; Tian, H.; Shao, H.; Yu, H.-Z. Host–guest interaction at molecular interfaces: cucurbit[7]uril as a sensitive probe of structural heterogeneity in ferrocenyl self-assembled monolayers on gold. *J. Phys. Chem. C.* **2018**, *122*, 15986-15995. <https://doi.org/10.1021/acs.jpcc.8b01067>.
- (69) Bain, C. D.; Whitesides, G. M. Formation of two-component surfaces by the spontaneous assembly of monolayers on gold from solutions containing mixtures of organic thiols. *J. Am. Chem. Soc.* **1988**, *110*, 6560–6561. <https://doi.org/10.1021/ja00227a044>.
- (70) Baker, B. R.; Lai, R. Y.; Wood, M. S.; Doctor, E. H.; Heeger, A. J.; Plaxco, K. W. An electronic, aptamer-based small-molecule sensor for the rapid, label-free detection of cocaine in adulterated samples and biological fluids. *J. Am. Chem. Soc.* **2006**, *128*, 3138–3139. <https://doi.org/10.1021/ja056957p>.
- (71) Ge, B.; Huang, Y. C.; Sen, D.; Yu, H. Z. A robust electronic switch made of immobilized duplex/quadruplex DNA. *Angew. Chem. Int. Ed.* **2010**, *49*, 9965–9967. <https://doi.org/10.1002/ANIE.201004946>.
- (72) Huang, Y. C.; Ge, B.; Sen, D.; Yu, H.-Z. Immobilized DNA switches as electronic sensors for picomolar detection of plasma proteins. *J. Am. Chem. Soc.* **2008**, *130*, 8023-8029. <https://doi.org/10.1021/ja8011066>.
- (73) Herne, T. M.; Tarlov, M. J. Characterization of DNA probes immobilized on gold surfaces. *J. Am. Chem. Soc.* **1997**, *119*, 8916–8920. <https://doi.org/10.1021/ja9719586>.
- (74) Bizzotto, D.; Burgess, I. J.; Doneux, T.; Sagara, T.; Yu, H.-Z. Beyond simple cartoons: challenges in characterizing electrochemical biosensor interfaces. *ACS Sens.* **2018**, *3*, 5-12. <https://doi.org/10.1021/acssensors.7b00840>.
- (75) Murphy, J. N.; Cheng, A. K. H.; Yu, H.-Z.; Bizzotto, D. On the nature of DNA self-assembled monolayers on Au: measuring surface heterogeneity with electrochemical in situ fluorescence microscopy. *J. Am. Chem. Soc.* **2009**, *131*, 4042-4050. <https://doi.org/10.1021/ja808696p>.
- (76) Du, Y.; Joon Lim, B.; Li, B.; Sherry Jiang, Y.; Sessler, J. L.; Ellington, A. D. Reagentless, ratiometric electrochemical dna sensors with improved robustness and reproducibility. *Anal. Chem.* **2014**, *86*, 8010-8016. <https://doi.org/10.1021/ac5025254>.

- (77) Pei, H.; Lu, N.; Wen, Y.; Song, S.; Liu, Y.; Yan, H.; Fan, C. A DNA nanostructure-based biomolecular probe carrier platform for electrochemical biosensing. *Adv. Mater.* **2010**, *22*, 4754–4758. <https://doi.org/10.1002/adma.201002767>.
- (78) Kolb, H. C.; Finn, M. G.; Sharpless, K. B. Click chemistry: diverse chemical function from a few good reactions. *Angew. Chem. Int. Ed.* **2001**, *40*, 2004–2021. [https://doi.org/10.1002/1521-3773\(20010601\)40:11<2004::AID-ANIE2004>3.0.CO;2-5](https://doi.org/10.1002/1521-3773(20010601)40:11<2004::AID-ANIE2004>3.0.CO;2-5).
- (79) Kalra, P.; Kaur, R.; Singh, G.; Singh, H.; Singh, G.; Pawan; Kaur, G.; Singh, J. Metals as “click” catalysts for alkyne-azide cycloaddition reactions: an overview. *J. Organomet. Chem.* **2021**, *944*, 121846–121873. <https://doi.org/10.1016/j.jorganchem.2021.121846>.
- (80) Hein, C. D.; Liu, X. M.; Wang, D. Click chemistry, a powerful tool for pharmaceutical sciences. *Pharm. Res.* **2008**, *25*, 2216–2230. <https://doi.org/10.1007/s11095-008-9616-1>.
- (81) Meng, X.; Xu, X.; Gao, T.; Chen, B. Zn/C-catalyzed cycloaddition of azides and aryl alkynes. *European J. Org. Chem.* **2010**, *28*, 5409–5414. <https://doi.org/10.1002/ejoc.201000610>.
- (82) Morozova, M. A.; Yusubov, M. S.; Kratochvil, B.; Eigner, V.; Bondarev, A. A.; Yoshimura, A.; Saito, A.; Zhdankin, V. V.; Trusova, M. E.; Postnikov, P. S. Regioselective Zn(OAc)₂-catalyzed azide-alkyne cycloaddition in water: the green click-chemistry. *Org. Chem. Front.* **2017**, *4*, 978–985. <https://doi.org/10.1039/c6qo00787b>.
- (83) Bozorov, K.; Zhao, J.; Aisa, H. A. 1,2,3-triazole-containing hybrids as leads in medicinal chemistry: a recent overview. *Bioorganic Med. Chem.* **2019**, *27*, 3511–3531. <https://doi.org/10.1016/j.bmc.2019.07.005>.
- (84) Johansson, J. R.; Beke-Somfai, T.; Said Stålsmeden, A.; Kann, N. Ruthenium-catalyzed azide alkyne cycloaddition reaction: scope, mechanism, and applications. *Chem. Rev.* **2016**, *116*, 14726–14768. <https://doi.org/10.1021/acs.chemrev.6b00466>.
- (85) Devadoss, A.; Chidsey, C. E. D. Azide-modified graphitic surfaces for covalent attachment of alkyne-terminated molecules by “click” chemistry. *J. Am. Chem. Soc.* **2007**, *129*, 5370–5371. <https://doi.org/10.1021/ja071291f>.
- (86) Pinson, J.; Podvorica, F. Attachment of organic layers to conductive or semiconductive surfaces by reduction of diazonium salts. *Chem. Soc. Rev.* **2005**, *34*, 429–439. <https://doi.org/10.1039/b406228k>.
- (87) Ssenyange, S.; Anariba, F.; Bocian, D. F.; McCreery, R. L. Covalent bonding of alkene and alkyne reagents to graphitic carbon surfaces. *Langmuir.* **2005**, *21*, 11105–11112. <https://doi.org/10.1021/la0516173>.

- (88) Sun, B.; Colavita, P. E.; Kim, H.; Lockett, M.; Marcus, M. S.; Smith, L. M.; Hamers, R. J. Covalent photochemical functionalization of amorphous carbon thin films for integrated real-time biosensing. *Langmuir*. **2006**, *22*, 9598-9605. <https://doi.org/10.1021/la061749b>.
- (89) Meldal, M.; Tomøe, C. W. Cu-catalyzed azide - alkyne cycloaddition. *Chem. Rev.* **2008**, *108*, 2952–3015. <https://doi.org/10.1021/cr0783479>.
- (90) Collman, J. P.; Devaraj, N. K.; Eberspacher, T. P. A.; Chidsey, C. E. D. Mixed azide-terminated monolayers: a platform for modifying electrode surfaces. *Langmuir*. **2006**, *22*, 2457–2464. <https://doi.org/10.1021/la052947q>.
- (91) Collman, J. P.; Devaraj, N. K.; Chidsey, C. E. D. “Clicking” functionality onto electrode surfaces. *Langmuir* **2004**, *20*, 1051–1053. <https://doi.org/10.1021/la0362977>.
- (92) Li, H.; Cheng, F.; Duft, A. M.; Adronov, A. Functionalization of single-walled carbon nanotubes with well-defined polystyrene by “click” coupling. *J. Am. Chem. Soc.* **2005**, *127*, 14518–14524. <https://doi.org/10.1021/ja054958b>.
- (93) Sun, X. L.; Stabler, C. L.; Cazalis, C. S.; Chaikof, E. L. Carbohydrate and protein immobilization onto solid surfaces by sequential diels-alder and azide-alkyne cycloadditions. *Bioconjug. Chem.* **2006**, *17*, 52–57. <https://doi.org/10.1021/bc0502311>.
- (94) Bard, A. J.; Faulkner, L. R. *Electrochemical methods: fundamentals and applications*, 2nd ed.; John Wiley & Son Inc.: Hoboken, U.S.A., 2001.
- (95) Elgrishi, N. N.; Rountree, K. J.; Mccarthy, B. D.; Rountree, E. S.; Eisenhart, T. T.; Dempsey, J. L. A practical beginner’s guide to cyclic voltammetry. *J. Chem. Educ.* **2018**, *95*, 197-206. <https://doi.org/10.1021/acs.jchemed.7b00361>.
- (96) Kaifer, A. E.; Gómez-Kaifer, M. *Supramolecular electrochemistry*; Wiley-VCH Weinheim. **1999**.
- (97) Savéant, J.-M.; Costentin, C. *Elements of molecular and biomolecular electrochemistry: an electrochemical approach to electron transfer chemistry*; John Wiley & Son Inc.: Hoboken, U.S.A., 2019.
- (98) Kissinger, P. T.; Heineman, W. R. Cyclic Voltammetry. *J. Chem. Educ.* **1983**, *60*, 702–706. <https://doi.org/10.1021/ed060p702>.
- (99) González-Meza, O. A.; Larios-Durán, E. R.; Gutiérrez-Becerra, A.; Casillas, N.; Escalante, J. I.; Bárcena-Soto, M. Development of a Randles-Ševčík-like equation to predict the peak current of cyclic voltammetry for solid metal hexacyanoferrates. *J. Solid. State. Electrochem.* **2019**, *23*, 3123-3133. <https://doi.org/10.1007/s10008-019-04410-6>.

- (100) Sandford, C.; Edwards, M. A.; Klunder, K. J.; Hickey, D. P.; Li, M.; Barman, K.; Sigman, M. S.; White, H. S.; Minter, S. D. A synthetic chemist's guide to electroanalytical tools for studying reaction mechanisms. *Chem. Sci.* **2019**, *10*, 6404–6422. <https://doi.org/10.1039/c9sc01545k>.
- (101) Qi, L.; Tian, H.; Yu, H.-Z. Binary thiolate DNA/ferrocenyl self-assembled monolayers on gold: a versatile platform for probing biosensing interfaces. *Anal. Chem.* **2018**, *90*, 9174–9181. <https://doi.org/10.1021/acs.analchem.8b01655>.
- (102) Yaakob, B. C. M.; Syahariza, Z. A.; Abdul, R. Fourier transform infrared (FTIR) spectroscopy: development, techniques, and application in the analyses of fats and oils. In *Fourier Transform infrared spectroscopy: development, techniques, and applications*; Rees, J. O., Ed; Nova Science Publishers, Inc.: New York, 2010; 1-26.
- (103) Alvarez-Ordóñez, A.; Prieto, M. Technical and Methodological Aspects of Fourier Transform Infrared Spectroscopy in Food Microbiology Research. In *Fourier Transform Infrared Spectroscopy in Food Microbiology*. Springer US: Boston, MA, 2012; 1-18.
- (104) Skoog, D. A.; Holler, F. J.; Crouch, S. R. Chapter twenty-one: surface characterization by spectroscopy and microscopy. In *Principle of Instrumental Analysis*, 7th ed.; Cengage Learning: Boston, MA, 2018; 537-545.
- (105) Brisdon, A. K. Vibrational spectroscopy. In *Inorganic Spectroscopic Methods*; Oxford University Press: New York, 2010; 10-29.
- (106) Sun, D.-W. Spectroscopic technique: mid infrared (MIR) and fourier transform mid infrared (FT-MIR) spectroscopies. In *Modern techniques for food authentication*, 1st ed.; Sun, D.-W, Ed.; Academic Press: Amsterdam, 2008; 27-57.
- (107) Handke, M.; Milosevic, M.; Harrick, N. J. External reflection Fourier transform infrared spectroscopy: theory and experimental problems. *Vib. Spectrosc.* **1991**, *1*, 251-262. <https://doi.org/10.1016/0924-2031%2891%2985002-5>
- (108) Fringeli, U. P. ATR and reflectance IR spectroscopy, applications. In *Encyclopedia of Spectroscopy and Spectrometry*; Lindon, J. C., Ed.; Academic Press: Amsterdam, 2000; 58–75.
- (109) Khoshhesab, Z. M. Reflectance IR spectroscopy. In *Infrared spectroscopy – materials science, engineering and technology*; Theophanides T., Ed.; InTech: Rijeka, 2012; 233-244.
- (110) Ras, R. H. A.; Schoonheydt, R. A.; Johnston, C. T. Relation between S-Polarized and p-Polarized Internal Reflection Spectra: Application for the Spectral Resolution of Perpendicular Vibrational Modes. **2007**. <https://doi.org/10.1021/jp073108a>.

- (111) Gan, N.; Liu, K.; Qi, L.; Zhang, G.; Guo, Y.; Sen, D.; Yu, H. Z. DNAzyme-catalyzed click chemistry for facilitated immobilization of redox functionalities on self-assembled monolayers. *J. Phys. Chem. C*. **2020**, *124*, 19083–19090. <https://doi.org/10.1021/acs.jpcc.0c05150>.
- (112) Good, R. J. Contact angle, wetting, and adhesion: a critical review. *J. Adhes. Sci. Technol.* **1992**, *6*, 1269–1302. <https://doi.org/10.1163/156856192X00629>.
- (113) Parvate, S.; Dixit, P.; Chattopadhyay, S. Superhydrophobic surfaces: insights from theory and experiment. *J. Phys. Chem. B*. **2020**, *124*, 1323–1360. <https://doi.org/10.1021/acs.jpcc.9b08567>.
- (114) Gupta, P.; Ulman, A.; Fanfan, S.; Korniaikov, A.; Loos, K. Mixed self-assembled monolayers of alkanethiolates on ultrasmooth gold do not exhibit contact-angle hysteresis. *J. Am. Chem. Soc.* **2005**, *127*, 4–5. <https://doi.org/10.1021/ja044623e>.
- (115) Heide, P. V. D. Preface. In *X-ray photoelectron spectroscopy – an introduction to principles and practices*; John Wiley & Sons Inc: Hoboken, 2012; xiii-xiv.
- (116) Hofmann, S. Instrumentation. In *Auger- and X-ray photoelectron spectroscopy in material science: a user-oriented guide*; Ertl, G., Lüth, H., Mills, D. L., Eds.; Springer-Verlag Berlin Heidelberg, 2013; 11-41.
- (117) Yu, H. Z.; Soolaman, D. M.; Rowe, A. W.; Banks, J. T. Evaporation of water microdroplets on self-assembled monolayers: from pinning to shrinking. *ChemPhysChem*. **2004**, *5*, 1035–1038. <https://doi.org/10.1002/cphc.200301042>.
- (118) Chen, K. S.; Qi, L.; Chen, J.; Wang, R.; Yu, H.-Z. “Click” cucurbit[7]uril hosts on self-assembled monolayers: quantitative supramolecular complexation with ferrocene guests. *J. Phys. Chem. C*. **2022**, *126*, 1661-1671. <https://doi.org/10.1021/acs.jpcc.1c09781>.
- (119) Chen, J.; Li, S.; Wang, Z.; Pan, Y.; Wei, J.; Lu, S.; Zhang, Q.-W.; Wang, L.-H.; Wang, R. Synthesis of an AIEgen functionalized cucurbit[7]uril for subcellular bioimaging and synergistic photodynamic therapy and supramolecular chemotherapy. *Chem. Sci.* **2021**, *12*, 7727-7734. <https://doi.org/10.1039/d1sc01139a>.
- (120) Kim, S.; Kim, D.; Hwang, G.; Jeon, J. A bromide-ligand ferrocene derivative redox species with high reversibility and electrochemical stability for aqueous redox flow batteries. *J. Electroanal. Chem.* **2020**, *869*, 114131-114137. <https://doi.org/10.1016/j.jelechem.2020.114131>.
- (121) Wei, X.; Cosimbescu, L.; Xu, W.; Hu, J. Z.; Vijayakumar, M.; Feng, J.; Hu, M. Y.; Deng, X.; Xiao, J.; Liu, J.; Sprenkle, V.; Wang, W. Towards high-performance nonaqueous redox flow electrolyte via ionic modification of active species. *Adv. Energy Mater.* **2015**, *5*, 1–7. <https://doi.org/10.1002/aenm.201400678>.

- (122) Chidsey, C. E. D.; Bertozzi, C. R.; Putvinski, T. M.; Mujisce, A. M. Coadsorption of ferrocene-terminated and unsubstituted alkanethiols on gold: electroactive self-assembled monolayers. *J. Am. Chem. Soc.* **1990**, *112*, 4301–4306. <https://doi.org/10.1021/ja00167a028>.
- (123) Joshi, D. R.; Adhikari, N. An overview on common organic solvents and their toxicity. *J. Pharm. Res. Int.* **2019**, *28*, 1–18. <https://doi.org/10.9734/jpri/2019/v28i330203>.
- (124) Osella, D.; Carretta, A.; Nervi, C.; Ravera, M.; Gobetto, R. Inclusion complexes of ferrocenes and-cyclodextrins. critical appraisal of the electrochemical evaluation of formation constants. *Organometallics*. **2000**. *19*, 2791-2797. <https://doi.org/10.1021/om0001366>.
- (125) Tang, H.; Fuentealba, D.; Ko, Y. H.; Selvapalam, N.; Kim, K.; Bohne, C. Guest binding dynamics with cucurbit[7]uril in the presence of cations. *J. Am. Chem. Soc.* **2011**, *133*, 20623-20633. <https://doi.org/10.1021/ja209266x>.
- (126) Ong, W.; Kaifer, A. E. Salt Effects on the Apparent Stability of the Cucurbit[7]Urill-Methyl Viologen Inclusion Complex. *J. Org. Chem.* **2004**, *69*, 1383-1385. <https://doi.org/10.1021/jo035030>.
- (127) Věžník, J.; Konhefr, M.; Trnková, L.; Skládal, P.; Lacina, K. Elusive PKa' of aminoferrocene determined with voltammetric methods in buffered and unbuffered systems and practical aspects of such experiments. *Electrochim. Acta.* **2019**, *318*, 534–541. <https://doi.org/10.1016/j.electacta.2019.05.113>.
- (128) Skeika, T.; Zuconelli, C. R.; Fujiwara, S. T.; Pessoa, C. A. Preparation and electrochemical characterization of a carbon ceramic electrode modified with ferrocenecarboxylic acid. *Sensors*. **2011**, *11*, 1361–1374. <https://doi.org/10.3390/s110201361>.
- (129) Liu, Q.; Yue, X.; Li, Y.; Wu, F.; Meng, M.; Yin, Y.; Xi, R. A novel electrochemical aptasensor for exosomes determination and release based on specific host-guest interactions between cucurbit [7]uril and ferrocene. *Talanta*. **2021**, *232*, 122451. <https://doi.org/10.1016/j.talanta.2021.122451>.
- (130) Kaifer, A. E.; Li, W.; Silvi, S.; Sindelar, V. Pronounced PH effects on the kinetics of cucurbit[7]uril-based pseudorotaxane formation and dissociation. *Chem. Commun.* **2012**, *48*, 6693–6695. <https://doi.org/10.1039/c2cc32871b>.

Appendix A.

Additional Supplementary Data

A1.

Determination of the effective surface area (A) of the gold working electrode.

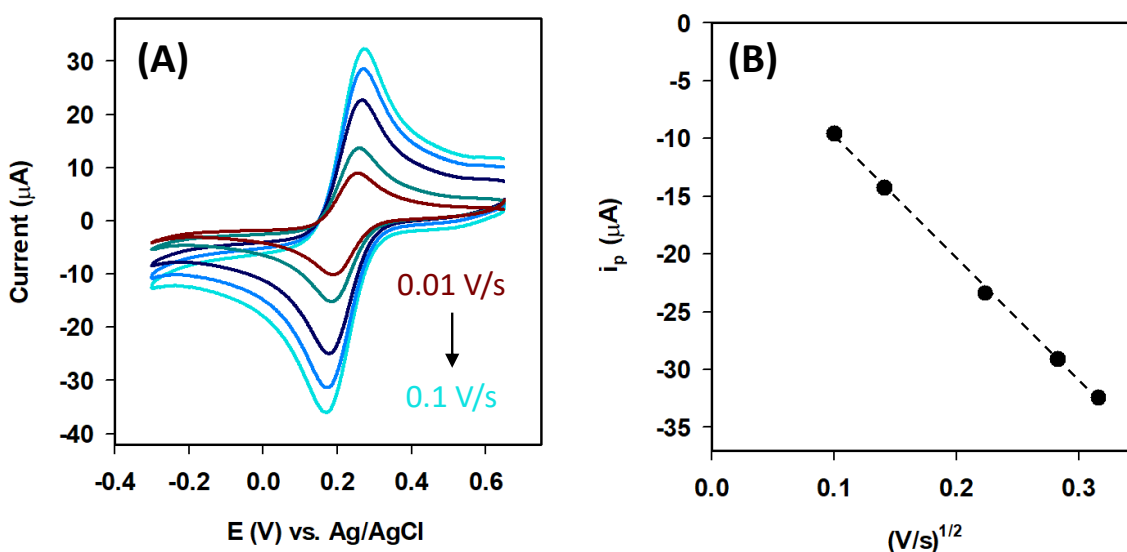


Figure A1-1. (A) Shows the cyclic voltammograms obtained at different scan rates (ν) in 1.0 mM $K_3Fe(CN)_6$ prepared in 0.1 M KCl. (B) A plot for the corresponding reduction peak current (I_p) as a function of square root of ν . The dashed line is the best fit linear line to the experimental data.

The good linear relationship with $R^2 > 0.99$ confirms the diffusion-controlled redox behavior of $K_3Fe(CN)_6$ on Piranha-cleaned bare gold surface. The effective surface area of the gold working electrode was determined to be $0.15 \pm 0.01 \text{ cm}^2$ based on Eq. (2.2) described in Section 2.1.

A2.

Preparation and Characterization of HO-CB[7] and \equiv -O-CB[7].

The alkyne-functionalized CB[7] (\equiv -O-CB[7]) used for this study was acquired from the same batch as that prepared by Chen et al.¹¹⁹ The synthesis was started with the preparation of a monohydroxy-CB[7] (HO-CB[7]) by utilizing the photochemical method reported by Ouari et al.^{44,45} with slight modifications (Figure A2-1). In brief, 232 mg of CB[7] (0.2 mmol, 1 eq.) was dissolved in 50 ml of 5 M HCl in a quartz test tube followed by sonication to ensure complete dissolution, and then degassed by bubbling N₂ for 10 min. Then, 10 μ l H₂O₂ (10 \times 10⁻¹⁴ mol) was added to the mixture and irradiated with 254 nm UV light with vigorously stirring. After 24 h of reaction, the solvent was removed using a vacuum rotary evaporator. By separating the residues using a silica column with acetic acid/H₂O/formic acid at a ratio of 10:10:1 as the solvent, a white color solid (HO-CB[7]) was obtained with a yield of 15%.

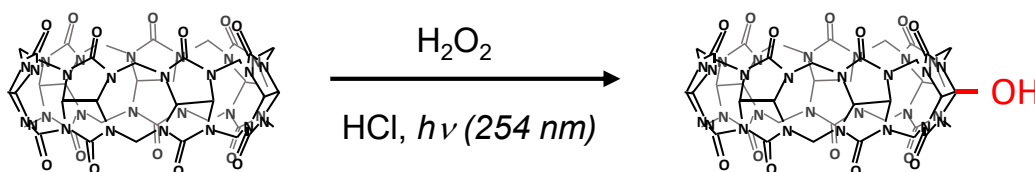


Figure A2-1. Synthesis of HO-CB[7] from CB[7].

The subsequent synthesis of \equiv -O-CB[7] from HO-CB[7] was performed by reacting with propargyl bromide (Figure A2-2).¹¹⁹ Specifically, 300 mg of HO-CB[7] was dissolved in 25 ml anhydrous DMSO with the help of sonication. Once the NaH (100 mg, 2.5 mmol, 10 eq. 60% in mineral oil) was added to the reaction mixture under an inert atmosphere at 0 °C, the mixture was continued to be stirred at room temperature for 2 h. Subsequently, 121 mg of propargyl bromide (1.0 mmol, 4 eq.) was added with a syringe at 0 °C followed by stirring at room temperature for another 12 h. To precipitate the generated \equiv -O-CB[7], the reaction mixture was poured into methanol then washed with another four portions of

methanol to remove any impurities. A fluffy light brownish solid with a yield of 82% was obtained after drying.

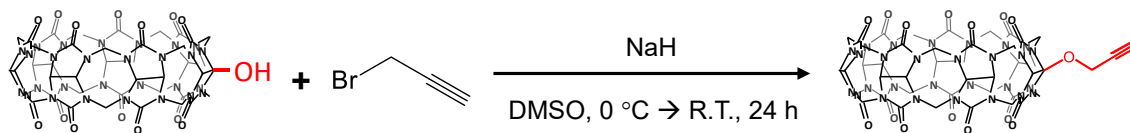


Figure A2-2. Synthesis of $\equiv\text{-O-CB[7]}$ from HO-CB[7] .

The characterization data for both the intermediate (HO-CB[7]) and the final product ($\equiv\text{-O-CB[7]}$) have been reported in the earlier publication.¹¹⁹ In particular, HO-CB[7] was confirmed with $^1\text{H-NMR}$ (600 MHz; D_2O): 4.29-4.26 (m, 12H), 4.53-4.50 (d, 2H), 5.26 (s, 1H), 5.57-5.47 (m, 14H), 5.76-5.62 (m, 12H). For $\equiv\text{-O-CB[7]}$, we have performed the following measurements: (1) ESI-MS (high resolution): 667.2523 m/z was for $[\text{HO-CB[7]} + \text{diaminohexane}]^{2+}$ (cal. for $\text{C}_{51}\text{H}_{62}\text{N}_{30}\text{O}_{15} = 667.2505$ m/z). (2) FTIR (KBr) 1736 cm^{-1} (C=O), 2118 cm^{-1} (-C \equiv C-), 3280 cm^{-1} (C \equiv CH), 3437 cm^{-1} (CO-N). (3) $^1\text{H-NMR}$ (600 MHz; $\text{D}_2\text{O} + \text{NaCl}$ puris): δ_{H} 2.65 ppm (m, 1H), 4.35-4.25 ppm (m, 13H), 4.52-4.64 ppm (m, 2H), 5.65-5.57 ppm (m, 14H), 5.75-5.71 ppm (m, 12H), and 5.82-5.80 ppm (d, 2H). (4) $^{13}\text{C-NMR}$ (150 MHz; D_2O): δ_{C} 47.51, 49.34, 52.61, 71.52, 77.57, 97.41, 155.46, 156.88.

The low yield for the synthesis of HO-CB[7] was a challenge,^{44,45} yet, the much better yield (82%) of the subsequent conversion of HO-CB[7] to $\equiv\text{-O-CB[7]}$ made the preparation of adequate amount of final product feasible for the surface modification described in this thesis.

A3.

Preparation and Characterization of FcN⁺Br⁻.

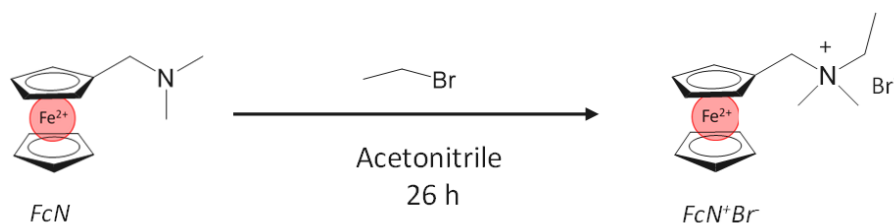


Figure A3-1. Synthesis of FcN⁺Br⁻ from (dimethylaminomethyl)ferrocene (FcN).

Note: Reprinted with permission from Ref 118. Copyright (2022), American Chemical Society.

As depicted in Figure A3-1, the synthesis of FcN⁺Br⁻ follows the method reported in the literature.^{120,121} First, 300 μ l of (dimethylaminomethyl)ferrocene (FcN \geq 95%) was dissolved in 20.0 ml of acetonitrile. Then 150 μ l of bromoethane (EtBr, 98%) was slowly dropped into the FcN solution. The reaction mixture was stirred at room temperature for one day. Once the reaction was done, the reaction mixture was placed under a vacuum rotary evaporator to remove acetonitrile and precipitate the product. The product was collected via filtration and washed subsequently with diethyl ether. The obtained precipitates were then dried at 40 °C in an oven overnight to get a final orangish-brown compound. The yield was 72% and the ¹H-NMR confirmation is shown in Figure A3-2.

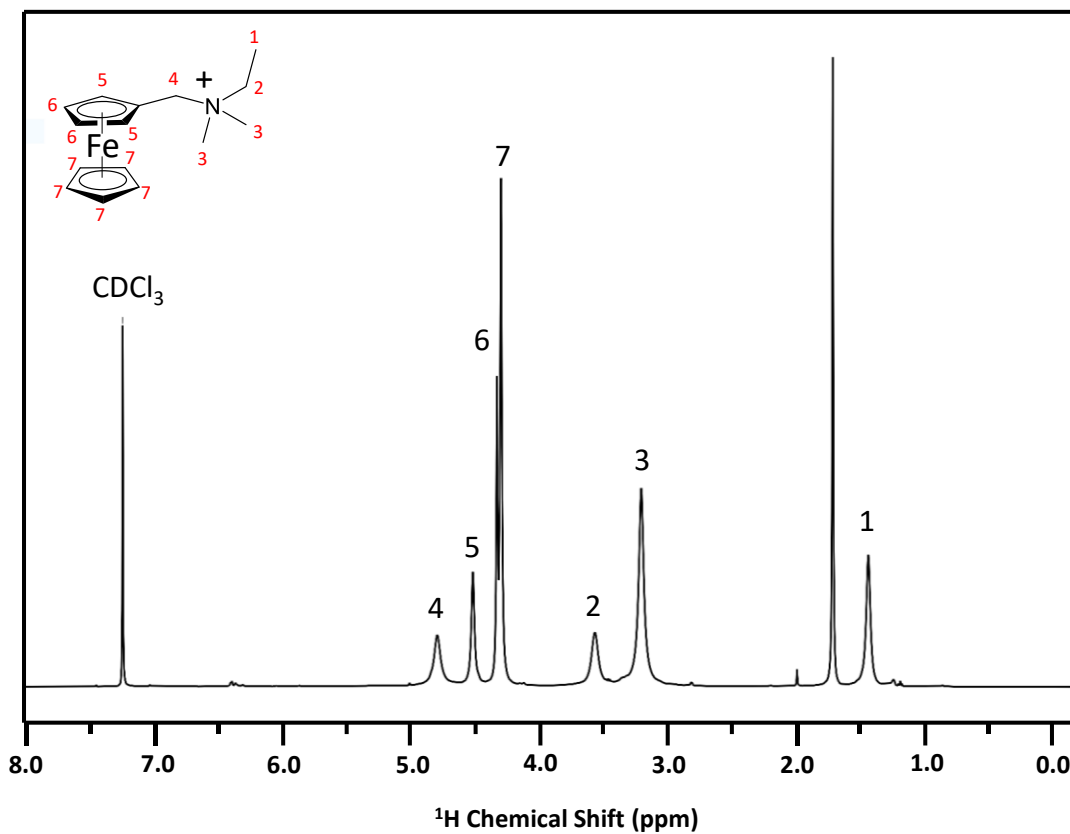


Figure A3-2. 400 MHz ¹H NMR spectrum of the synthesized FcN⁺Br⁻ in chloroform-D (CDCl₃).

Note: Reprinted with permission from Ref 118. Copyright (2022), American Chemical Society.

Appendix B

Additional Publication List

- 1) Jiang, F.; Qi, L.; Schultz, C. W.; **Chen, K. S.**; Song, G.; Yu, H.-Z. Flexible graphene substrates for electrochemical analysis and construction of functional nanostructures. *Electrochim. Acta.* **2021**, *329*, 139008-139015. <https://doi.org/10.1016/j.electacta.2021.139008>.

My contribution: assisted in additional experiments suggested by the reviewers.

- 2) Liu, K.; **Chen, K. S.**; Sen, D.; Yu, H.-Z. Ultrasensitive detection of total copper with an electrochemical biosensor built on the in cis coupling of hexynyl CLICK-17 DNAzyme with azido self-assembled monolayers. *Electrochim. Acta.* **2021**, *379*, 138125-138132. <https://doi.org/10.1016/j.electacta.2021.138125>.

My contribution: assisted in electrochemical experiment design, revising the paper, and doing additional experiments suggested by the reviewers.

- 3) Zhang, L.; Zhou, A. G.; Sun, B. R.; **Chen, K. S.**; H.-Z. Yu. Functionalized and versatile superhydrophobic coating via stoichiometric silanization. *Nat. Commun.* **2021**, *12*. <https://doi.org/10.1038/s41467-021-21219-y>.

My contribution: assisted in doing experiments.

- 4) Zhang, L.; **Chen, K. S.**; H.-Z. Yu. Superhydrophobic glass microfiber filter as background-free substrate for quantitative fluorometric assays. *ACS Appl. Mater. Interfaces.* **2020**, *12*, 7665-7675. <https://doi.org/10.1021/acsami.9b17432>.

My contribution: assisted in doing experiment and revising the paper.